Structural and Functional Effects of the Ageing Lens Environment on Connexin-46/50 Gap Junctions

By

Jonathan Alexander Flores

A DISSERTATION

Presented to the Department of Chemical Physiology & Biochemistry at the

Oregon Health & Science University

School of Medicine

in partial fulfillment of

the requirements for the degree of

Doctor of Philosophy

April 2022

Table of Contents

Table of Figures

Chapter 1

Chapter 2

Chapter 3

Chapter 4

Abstract

Transparency of the ocular lens is essential for vision. To maintain lifelong transparency, the avascular lens employs a complex system of ion pumps, transporters, and membrane channels that facilitate circulation of water, ions, and nutrients. Because there is no protein turnover in the lens, this microcirculatory system is subject to a lifetime of chemical modifications and oxidative stress that eventually leads to loss of homeostasis and cataract development. Age-related decline in lens circulation is correlated with changes to the cellular environment, including cytoplasmic acidification, a rise in intracellular Ca^{2+} (Ca^{2+}_i), and dramatic enrichment of membrane cholesterol (CHL). The interplay between cataracts and these age-related changes to the lens environment have been actively studied since the 1970s. Despite a remarkable body of work from the past half-century, a molecular understanding for how environmental changes in the lens affect the proteins involved in microcirculation remains unclear.

A pair of proteins critical to lens circulation and transparency are connexin-46 and connexin-50 (Cx46/50), which form cell-to-cell communication channels known as gap junctions. This class of membrane channel forms a conduit between the cytoplasm of neighboring cells to facilitate rapid and direct communication of electrical and chemical signals. Gap junctions electrochemically couple cells throughout the body and this property is essential for normal physiology in a variety of tissues. In the lens, Cx46 and Cx50 facilitate outward flux of ions and metabolites as part of microcirculation and maintenance of transparency. Solute

permeation through Cx46/50 is regulated by various cellular signals (e.g., pH, Ca^{2+}_i, CHL); however, a mechanistic basis for how these signals modulate the structure and function of Cx46/50 (and other gap junctions) is not understood.

Gap junctions have been targeted by crystallographers for decades, but challenges with this technology have stymied progress. The recent arrival of a "resolution revolution" in single-particle cryoEM has put the target of high resolution structures of macromolecular complexes formerly stymied by crystallography (such as membrane proteins) now in reach. In pursuit of atomic-level insights into Cx46/50, the Reichow Lab determined the first high-resolution structure of Cx46/50 by cryoEM, demonstrating the feasibility of this technology in pursuit of high-resolution gap junction structures. To expand on this progress, my dissertation research has focused on understanding 1) how Cx46/50 interacts with the local lipid environment, 2) how age-related cholesterol enrichment in the lens affects Cx46/50 structure and function, and 3) the mechanistic basis for Ca^{2+}-induced channel gating in Cx46/50 intercellular channels.

Chapter 1: Structure & Function of the Lens Connexins

Authors: Jonathan A. Flores[1] and Steve L. Reichow[1,2]

Affiliations:

[1] Department of Chemical Physiology and Biochemistry, Oregon Health and Science University, Portland OR 97239, U.S.A.

[2] Department of Chemistry, Portland State University, Portland OR 97201, U.S.A.

Author Contributions

J.A.F and S.L.R. contributed to manuscript preparation.

S.L.R. provided overall guidance to the design and execution of manuscript preparation.

This is an unpublished manuscript in preparation

The life-long transparency of the eye lens

The complex eye is a hallmark adaptation of higher animals, and a central feature is the transparent lens. The lens focuses light from the environment onto the retina at the posterior. Image formation occurs as photons reach photoexcitable neurons in the retina. This process of phototransduction—whereby visible light is converted to a cellular signal—is in the biological sense, vision. This process is impossible without a transparent, properly functioning eye lens.

The mammalian lens is composed of two cell types. A single layer of epithelium forms the anterior, light-facing surface of the lens. These cells divide and terminally differentiate into elongated fiber cells that stretch from pole to pole and form the bulk of the lens[1] (Fig. 1A). The newest fiber cells layer atop older ones, such that older fiber cells reside at the core of the lens, and younger at the so-called cortex[2]. Fiber cells at the core terminally differentiate *in utero* and because there is no cellular turnover in the lens, mature fiber cells remain with the organism throughout life[3]. As fiber cells differentiate, all internal organelles are degraded in order to minimize light scatter[4,5]. Therefore, a defining feature of the mature lens is that there is no protein synthesis or turnover. From a biochemical perspective, mature fiber cells present an intriguing biological problem: the protein complement in each fiber cell must remain stable and functional throughout life[6].

The uniqueness of lens biology means that proteins expressed in the fiber cells are subject to a lifetime of chemical and UV damage. The accumulation of age-related posttranslational modifications (PTMs) can eventually lead to a loss of proteostasis, protein denaturation and ultimately precipitation of the cytosolic lens

crystallin proteins (which make up 90% of the cytosolic lens proteome)[7]. These precipitation events result in light-scattering opacities (a.k.a. cataract)[8,9,10]. Left untreated, age-related cataracts either severely or completely impair vision, leading to blindness. Despite effective surgical treatment, cataracts remain the leading cause of blindness worldwide[11].

The lens microcirculatory system

Because fiber cells lack organelles, the lens relies largely on glycolysis for ATP production[12] and since the lens is totally avascular, accumulation of metabolic byproducts can't be removed by chemical exchange with blood vessels. As an alternative, evolution arrived at a unique mechanism, involving the coordination of membrane channels, transporters, and pumps for circulation of water, ions, and metabolites that would otherwise accumulate to toxic levels. This complex microcirculatory system is solely responsible for shuttling metabolic waste products and delivery of nutrients required for the maintenance of lens health and transparency (Fig. 1B)[13,14].

Maintenance of ionic homeostasis

A key feature of this microcirculatory system is chemical coupling of lens cells through channels known as gap junctions (Fig. 1B). Gap junctions provide continuous intercellular pathways from deep-lying fiber cells at the core, to the outermost cells in the cortex and epithelium[15]. To direct the flow of circulation through gap junctions, a complex milieu of membrane channels, transporters, pumps, and exchangers act in concert to maintain ionic homeostasis.

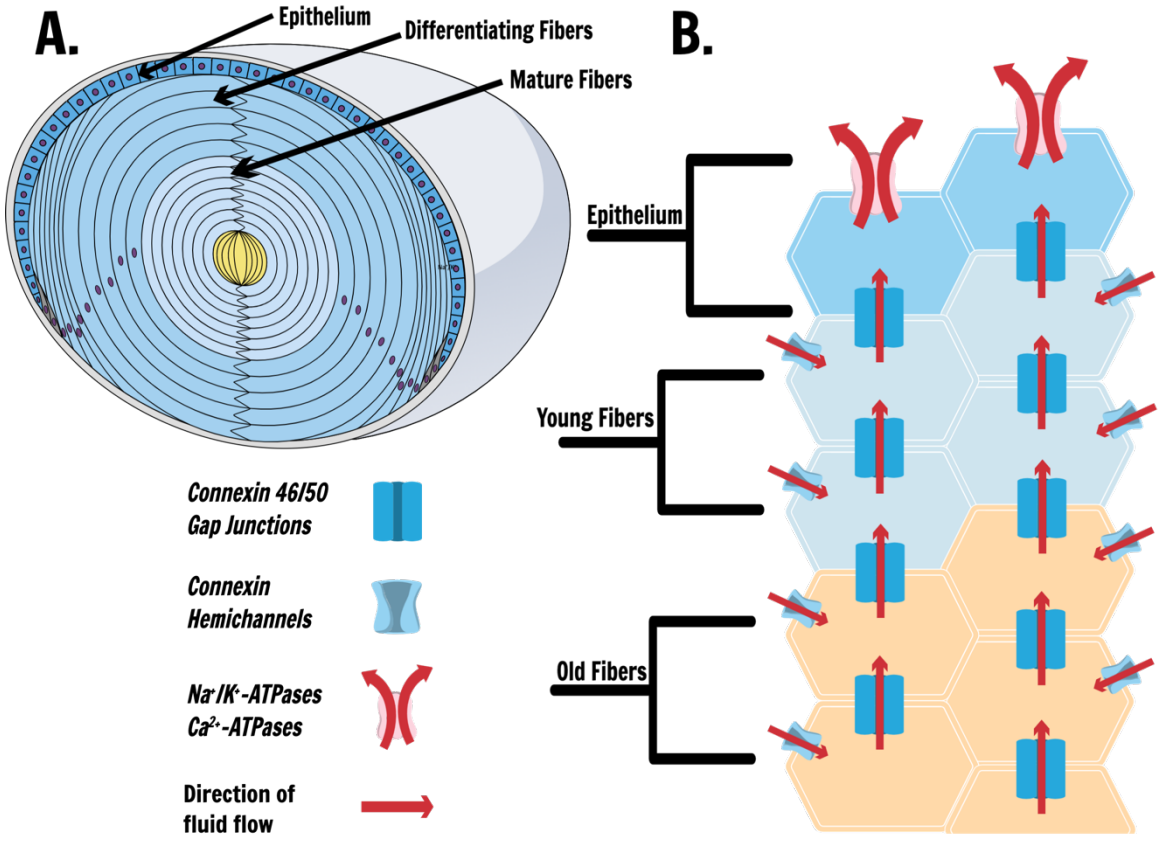

Figure 1 — Lens physiology and fluid circulation.

(A) A single layer of epithelial cells at the anterior lens divide and differentiate into the fiber cells throughout life. Newly differentiated fiber cells layer atop older ones, such that older cells are found in the lens core, while younger cells are nearer to the lens surface. ***(B)*** Ion, water, and nutrient circulation is facilitated by membrane channels known as gap junctions. Fiber cells cannot autonomously maintain ionic homeostasis. Instead, lens gap junctions permeate cytoplasmic solutes — such as Na^+ and Ca^{2+} — down their concentration gradient toward the epithelium, where Na^+/K^+- and Ca^{2+}-ATPases actively pump ions against their concentration gradient out of the cell, thereby maintaining ionic homeostasis for the bulk of the lens syncytium.

Fiber cells maintain typical intracellular concentrations of Na^+ (Na^+_i) and K^+ (K^+_i) despite having no Na^+/K^+-ATPase activity. This phenomenon is facilitated by equatorial epithelial cells, which are the only cells in the lens that express Na^+/K^+ pumps in abundance[16,17]. Therefore, the epithelium is the only lens tissue where ATP hydrolysis drives the flux of Na^+ and K^+ against their concentration gradients.

Electrochemical coupling through gap junctions allows the fiber cells to "piggyback" on Na^+/K^+-ATPase activity in the epithelium to maintain low Na^+_i and high K^+_i.

In the same way, intracellular Ca^{2+} (Ca^{2+}_i) is kept at levels typically found for cells at resting conditions (~100-300 nM)[18]. Virtually all tissues control Ca^{2+} flux through Ca^{2+}-ATPases and Na^+/Ca^{2+} exchangers in the plasma membrane and endoplasmic reticulum[19]. Since fiber cells lack these proteins and are incapable of autonomous Ca^{2+}_i regulation, the Ca^{2+}-ATPases and Na^+/Ca^{2+} exchangers in the epithelium are responsible for regulation of Ca^{2+}_i for the entirety of the lens[20,21].

Active transport of ions in the epithelium establishes the driving force of lens circulation. Gap junctions play a central role by forming insulated pathways that directly couple the cytosol of neighboring cells. These pathways are required for water, ions, antioxidants, nutrients, and metabolites to reach the lens core, and for waste products to be removed[12,14]. If gap junction coupling is compromised by either congenital mutation or age-related deterioration, fluid circulation is diminished and cataracts can form[22,23].

Structure and function of the lens gap junctions

Gap junctions are multisubunit complexes formed by members of the connexin protein family (21 isoforms in human)[24]. Connexins are integral membrane proteins that are differentially expressed throughout the body. Each subunit is composed of four transmembrane domain helices (TM1-4) connected by two short extracellular loops (EC1-2) that connect TM1-2 and TM3-4, respectively[25–27] (Fig. 2A). At the intracellular side of the channel is a single intracellular loop domain

(ICL; connecting TM2-3) and a c-terminal domain (CTD) following TM4 that diverge considerably in size and sequence from isoform to isoform. Connexins also contain a short (~20 residues) n-terminal helix (NTH) that forms the putative gating domain in connexin channels[28].

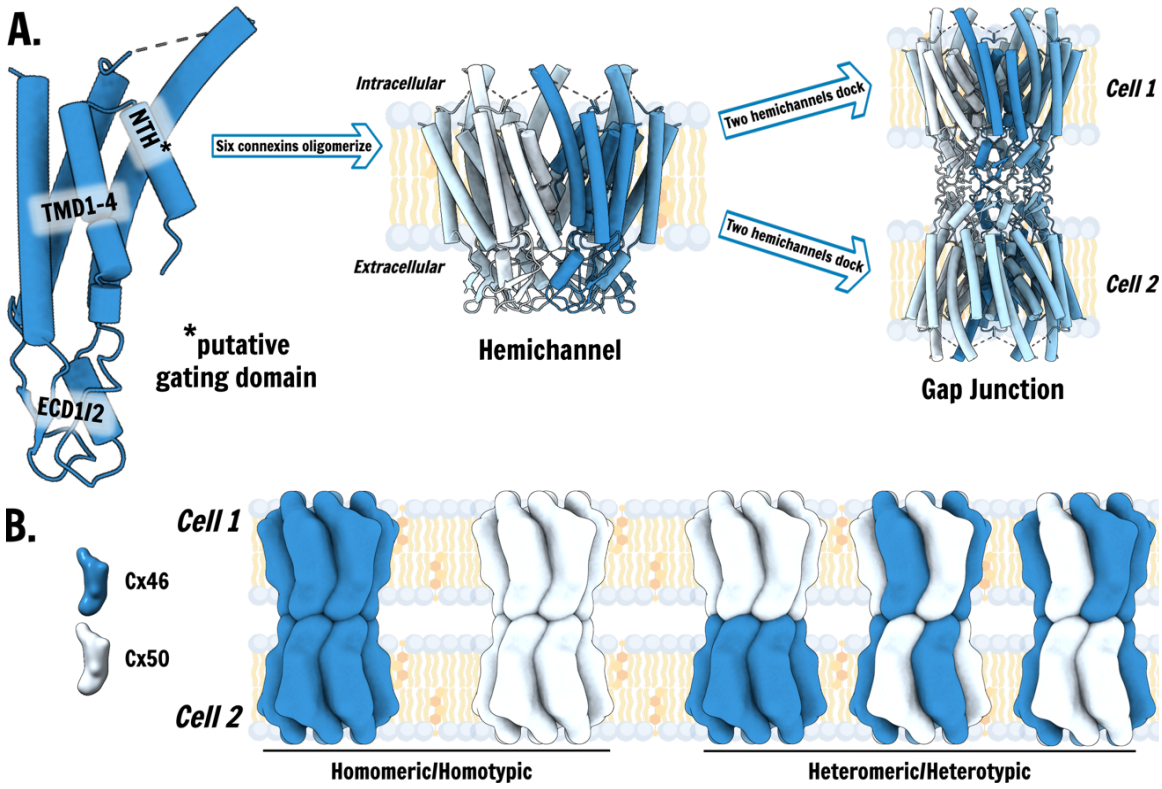

Figure 2 — Overview of lens gap junction structure and assembly.

(A, left) Monomeric atomic model for Cx46 (PDB: 7JKC). Connexins have four transmembrane domains (TMD1-4), two extracellular loops (EC1/2), and a pair of disordered cytoplasmic domains (not pictured). Connexins also have a short (~20 residues) n-terminal helix domain (NTH) that is putative gating domain for connexin channels. ***(A, middle)*** Connexin hemichannels are formed when six connexin subunits oligomerize in the cell membrane. ***(A, right)*** Hemichannels in neighboring cell membranes can dock through EC1/2 to form the dodecameric gap junction, which provides a pathway for direct electrochemical exchange between neighboring cells. ***(B)*** Gap junction channels are referred to as *homomeric* if they are composed of a single connexin isoform, and *heteromeric* if they are composed of more than one unique isoform. Gap junction channels are described as homotypic when both hemichannels are composed of identical isoforms, and *heterotypic* when the channel is composed of more than one unique isoform.

During biogenesis, six connexin subunits oligomerize to form a so-called hemichannel that traffics to the plasma membrane[29,30]. Connexin hemichannels can remain undocked and perform a variety of important non-gap junctional roles[31–33]. When a pair of compatible hemichannels from neighboring cells are opposed, they can dock through to form a conduit for intercellular communication, known as a gap junction intercellular channel[34]. Gap junctions assemble into higher-order assemblies known as plaques, in which 10s to 1000s of channels tightly cluster with one another in the cell membrane[35,36].

The lens microcirculatory system is facilitated by connexin channels in two major ways (Fig. 3). The most prominent and well-studied is in providing a network of pathways to various cytoplasmic solutes that must circulate throughout the lens[13]. Connexin hemichannels play a less well-understood role(s), but are thought to contribute to a Na^+ leak conductance in the fiber cells[33]. This establishes a standing gradient throughout the lens in which Na^+_i in the core is elevated relative to the cortex. The osmotic pressure from the Na^+ gradient directs water from the innermost fiber cells toward the epithelium. Various molecular species follow the flow of water and Na^+ to preserve lens homeostasis and transparency.

Most tissues express 2 or more unique connexin isoforms and with exception to certain compatibility restraints[34], different connexin isoforms can co-assemble in the same channel (Fig. 2B). Connexin channels are described as *heteromeric* when 2 or more connexin isoforms assemble into the same hemichannel, and *heterotypic* when different isoforms are distributed between the 2 docked hemichannels in a gap junction.

The ocular lens is a classic example of how connexin distribution is tightly regulated. In the epithelium, gap junctions are composed Connexin-43 (Cx43) and Connexin-50 (Cx50). During fiber cell differentiation, Cx43 is replaced by Connexin-46 (Cx46), with the downregulation of Cx43 expression and upregulation of Cx46 expression[37,38]. Thus, gap junctions in lens fiber cells are composed of Cx46 and Cx50. In the native lens, Cx46/50 form heteromeric/heterotypic assemblies[39]. It is thought that the precise nature of Cx46/50 co-assembly confers unique biophysical properties that may serve specialized physiological roles in the lens[33,40,41]. However, the precise pattern(s) of Cx46/50 co-assembly, spatial distribution of these assemblies, and their importance to lens circulation remain ongoing questions in the field.

Age-related changes to connexin-46/50 and the lens environment

Lens fiber cell gap junctions (connexin-46/50) must remain functional throughout the lifespan of the individual for lens circulation to remain uncompromised. However, the incidence of age-related cataract rises sharply with age[42,43], and a variety of age-related changes to lens proteins and the lens environment are associated with age. Therefore, to obtain a complete understanding of cataract progression, an intimate understanding of these age-related changes is required.

Age-related posttranslational modifications in connexin-46/50 — Perhaps the most well-studied age-related post-translational modification (PTM) of lens Cx46/50 is

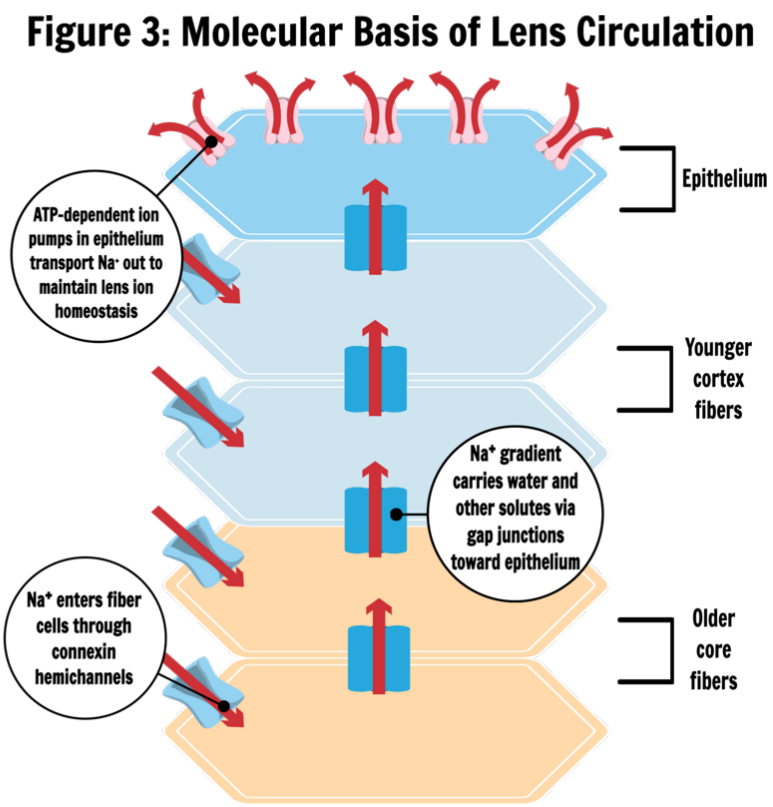

Figure 3 — Connexin channels are central regulators of lens circulation and ionic homeostasis.

Na^+ leak conductance via connexin hemichannels establishes a standing gradient in which older fibers in the core have elevated Na^+ relative to younger cortex fibers. Electrochemical coupling of the fibers through gap junctions permits Na^+, water, and other solutes to move down their concentration gradient toward the epithelium. Ion pumps, transporters, and exchangers actively transport various ionic species against their concentration gradient to maintain ionic homeostasis throughout the lens.

cleavage of the CTD. CTD cleavage of Cx46/50 is abundant in mature fiber cells, while Cx46/50 exists as a mixture of full-length and cleaved in differentiating fiber cells[37–47]. A less well-studied cleavage site in the ICL was recently identified in Cx46/50 isolated from human lenses, and distribution of this cleavage follows the same age-related trend as the CTD[48]. Cx46/50 channels with a truncated CTD form functional channels in cell culture, while ICL cleavage mutants fail to form functional channels when expressed in a heterologous system[48]. However, the studies on ICL cleavage do not replicate the native situation, as ICL cleavage would occur after channels were formed at the plasma membrane—a condition

that is not mimicked in these studies. Thus, it remains to be seen whether ICL cleavage is a physiologically important PTM, or if ICL cleavage is an age-related aberration that destroys connexin channel function.

The Cx46/50 NTH is also subject to a combination of PTMs. Met1 is co-translationally cleaved, leaving Gly2 at the connexin NH_2-terminus that is also acetylated[49]. Work from the Reichow Lab has shown that NTD acetylation alters the electrostatic profile of the pore, lowering the energy barrier for cation permeation and *vice versa* for anion permeation[27].

The CTD and ICL domains of Cx46/50 are heavily phosphorylated at several serine and threonine residues[50,51]. Phosphorylation is implicated in regulation of lens intercellular communication by modulating the expression, trafficking, stability, and intercellular coupling of connexin channels[52–56]. However, since the pattern of phosphorylation is highly heterogeneous in native tissues, the precise combination of phosphorylation sites that produce distinct functional outcomes are still not known.

Overall, the lens proteome is subject to a diverse array of PTMs, and age-related PTMs that have been identified are found in many proteins essential to lens transparency and homeostasis[7,57]. These PTMs include lipidation, racemization, deamidation, crosslinking, and even spontaneous (i.e., non-enzymatic) peptide cleavage[7,57]. While these PTMs have been extensively studied in the context of other proteins in the lens, such as the crystallins[7,57], it remains unclear whether Cx46/50 in the lens are subject to these PTMs in any age-related manner.

Age-related changes in lens ion concentrations

Due to the unique cellular organization and physiology of the lens, there are a series of chemical gradients that become established from the core through the cortex (Fig. 4). Perhaps the most well-studied example is the standing gradient of cytoplasmic pH[58,59], in which fibers at the core have relatively acidic pH (~6.8) relative to younger fibers in the cortex (~7.2), a result of anaerobic metabolism in the fiber cells[15,58]. Intracellular calcium (Ca^{2+}_i) follows a similar gradient, in which standing levels of Ca^{2+}_i vary from ~700 nM in the core to ~300 nM in the cortex[18], due to the lack of Ca^{2+} exchange in mature fiber cells.

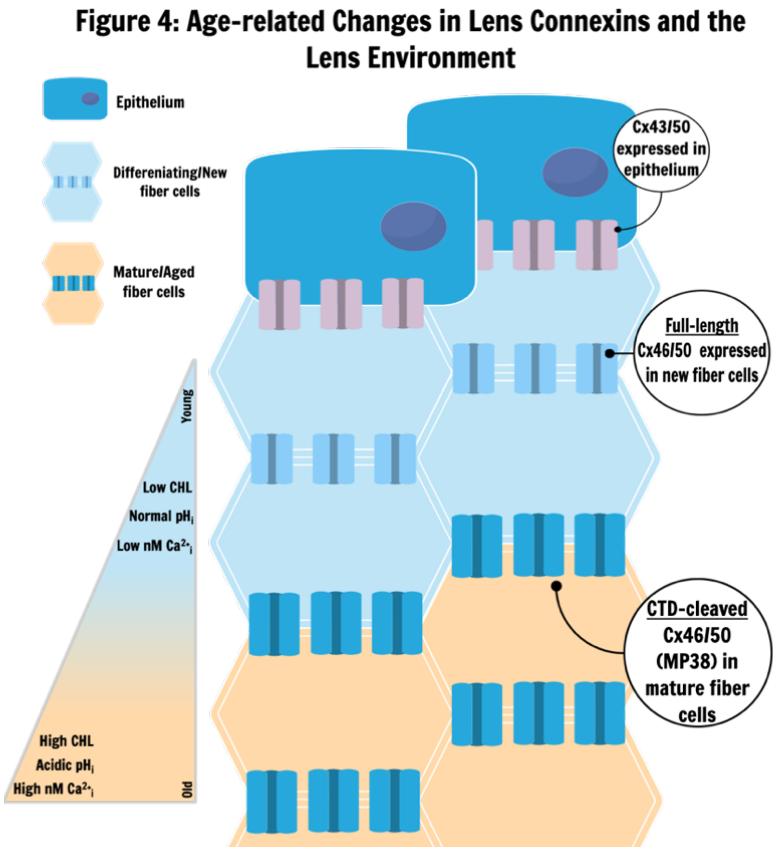

Figure 4 — The ageing process subject the lens connexins to a variety of biochemical and environmental changes. As the lens epithelium differentiates into the long-lived fiber cells, Cx43 is replaced by Cx46. Connexin channels in mature fiber cells are exclusively composed of Cx46 and Cx50 (full-length; a.k.a. MP70). Newly differentiated fiber cells also have typical membrane cholesterol (~25 mol%), pH_i (~7.2), and Ca^{2+}_i (~300 nM). As fiber cells age, the cytoplasmic c-terminal domain in Cx46/50 is proteolytically cleaved (CTD-cleaved; a.k.a. MP38), and the truncated form of Cx46/50 predominates in the lens core. Aged fiber cells also have elevated membrane cholesterol (up to ~80 mol%), Ca^{2+}_i (~700 nM), and acidic pH_i (~6.8).

Disruption of lens circulation by genetic knockout or mutation of Cx46/50 virtually eliminates fiber cell coupling[56–59]. Defining features of circulation-deficient lenses are abnormally high Ca^{2+}_i and dense central cataracts[18,64,65]. Based on these studies, a putative model for cataract progression begins with age-related deterioration of cell-to-cell coupling, which in turn deteriorates Ca^{2+} circulation. The rise in Ca^{2+}_i activates otherwise dormant calpain proteases that cleave the lens crystallins. Aberrant cleavage of crystallins leads to protein aggregates and lens opacitification[18,66,67]. Consistent with this model, it was shown that Ca^{2+}-rich precipitates are found in lens opacities[60,61,64,65]. The precise mechanism of how Ca^{2+} interacts with Cx46/50 to interfere with circulation remains a major roadblock to a critical evaluation of this model.

Age-related changes in lens lipids

Fiber cells also exhibit substantial age-related changes in plasma membrane composition. Despite the lack of lipid turnover in the mature lens[70], fiber cell membranes exhibit marked changes in various lipid abundances, acyl chain length, and saturation level[71,72]. The most dramatic age-related change in lens lipids was discovered by measuring cholesterol content among progressively deeper fiber cell layers from intact lenses[73–76]. Membrane cholesterol content in young fiber cells is typical for most cells in the body (20-25 mol%). Remarkably, older fiber cells at the core have cholesterol content up to 80 mol%, making core lens tissue the most cholesterol-rich in the human body.

The general effects of cholesterol on lipid membranes are well-documented: cholesterol increases bilayer order and strengthens the hydrophobic barrier to passive diffusion[77,78]. Pure cholesterol bilayer domains (CBDs) form when cholesterol reaches ~50 mol% and beyond ~70 mol%. At the highest concentrations found in lens membranes, cholesterol may even crystallize[79–81]. While the effect of cholesterol enrichment on lens membrane properties has been under active study for over 3 decades[82–84], very little is known about how this membrane environment affects the structure and function of lens membrane proteins.

Modulation of Cx46/50 activity by age-related changes in the lens

Coupling conductance of core fiber cells is reduced by 50%, as compared with cortex fiber cells[18]. A potential explanation for this is that age-related changes in the lens modulate fiber cell coupling through Cx46/50 to disrupt lens circulation. Age-related changes in PTMs, pH, Ca^{2+}_i, and lipids have all been implicated in regulation of connexin channel function[85–89]. The work completed as part of this thesis is focused specifically on the structural and functional effects of age-related changes in the lipid environment and Ca^{2+}_i on Cx46/50 gap junctions.

How do changes in membrane lipid composition affect connexin channel structure and function?

Because fiber cells shed internal organelles and halt new protein synthesis during differentiation, there is no lipid turnover in the mature lens[70]. Nonetheless, the composition and biophysical nature of lens membranes are shaped by

accumulation of age-related chemical changes[72,80,90]. While spatial and temporal changes to lens lipids have been extensively characterized[72,80], comparatively little is known about how membrane proteins respond to these changing conditions. Some insights have been gained from studies involving intercellular junctions in cell culture systems, as well as complementary *in vitro*/computational studies with non-lens connexins.

Junctional domains from liver and lens have markedly enriched cholesterol relative to total membrane cholesterol, varying from ~50-80 mol%[91]. In cultured hepatocytes, cholesterol supplementation increased gap junction formation and junctional communication[92]. The same effect has been seen in cultured smooth muscle cells, and supplementation with oxidized cholesterol derivatives reduced gap junctional communication by up to 40%, pointing to lipid oxidation as a potential precursor to connexin channel dysfunction in disease[93].

Changes to plasma membrane properties conferred by cholesterol enrichment may directly influence gap junctional communication. In cultured rat cardiac cells, heptanol treatment increased bulk membrane fluidity and decreased local membrane fluidity at intercellular junctions[94]. Localized decrease in membrane fluidity in intercellular junctions was correlated with an ~80% decrease in junctional conductance.

Maturation of gap junctions during fiber cell differentiation is also linked to cholesterol. In the chick lens, loosely-packed gap junctions form in cholesterol-rich membrane domains of newly formed fiber cells[95,96]. As fiber cells mature, gap junctions adopt more tightly-packed, quasi-crystalline arrays relatively devoid of

cholesterol[95,96]. Intriguingly, cholesterol abundance in fiber cells from clear lenses can reach ~80 mol%[97], implying that functional connexin channels in mature fiber cells persist in extremely cholesterol-rich cell membranes. In summary, gap junction formation and intercellular communication is sensitive to cholesterol. What remains unclear however, is whether direct cholesterol interactions influence connexin channel structure and function.

Studies that directly probe connexin channel permeability as a function of lipid composition have provided important insight. Permeability of Cx26 and Cx32 hemichannels reconstituted into liposomes are sensitive to lipid composition and cholesterol content[98]. Cx26 and Cx32 have maximal permeability at ~25 mol% cholesterol, but deviations from this value decrease permeability[98], implying that connexins may be regulated by direct interactions with cholesterol and/or biophysical properties of the membrane imparted by cholesterol. In support of the former, coarse-grained molecular dynamics simulations have identified putative cholesterol binding sites at the subunit interface of Cx26 hemichannels[99]. These experiments point strongly toward a direct dependence on cholesterol in connexin channel function, but the molecular details of these interactions are still not understood, and it remains unclear whether a cholesterol-saturated membrane environment modulates Cx46/50 channel activity.

How does dysregulation of intracellular Ca^{2+} affect cell-to-cell coupling via Cx46/50?

In virtually every cell type, Ca^{2+}_i is tightly regulated through a complex interplay of Ca^{2+}-ATPases and Na^{+}/Ca^{2+} exchangers in the plasma membrane and

endoplasmic reticulum. When cells are stressed or damaged, Ca^{2+} mishandling triggers apoptotic and/or necrotic cell death[100]. Connexin channels are highly sensitive to Ca^{2+}. Hemichannels are closed by extracellular Ca^{2+}, preventing leak of cytosolic content[86,101,102]. Meanwhile, in the context of gap junctions, direct Ca^{2+} binding and/or Ca^{2+}/Calmodulin can lead to cellular uncoupling[103,104]. Genetic perturbation of residues implicated in Ca^{2+} binding either reduce or abolish Ca^{2+} sensitivity[105,106], and Ca^{2+} mishandling is associated with human diseases in a variety of tissues[107–111]. Ca^{2+} sensitivity of connexin channels is thought play a protective role in injured tissues, whereby uncoupling of gap junctions can limit the spread cytotoxic signals to nearby cells[112–114]. Because fiber cells lack canonical mechanisms to maintain low Ca^{2+}_i, Ca^{2+} regulation in the lens is totally distinct from other tissues[115]. The lens gap junction network allows movement of Ca^{2+} down its concentration gradient from the lens core to the site of active Ca^{2+} export in the epithelium. When lens circulation is disrupted through mutation of Cx46/50, Ca^{2+} accumulates in fibers to cytotoxic levels[18,65]. Over 120 cataract-associated mutations in lens connexins have been identified in humans[116], many of which localize to pore-lining regions that result in aberrant channel activity[109,117]. Mounting evidence suggests that Ca^{2+} mishandling via disruption of gap junction coupling plays a role in cataractogenesis[64,65,68,69]. To shine a mechanistic light on the regulation of connexin channel activity by Ca^{2+}, the work completed as part of this thesis has focused on exploring the mechanism of Ca^{2+}-induced channel gating.

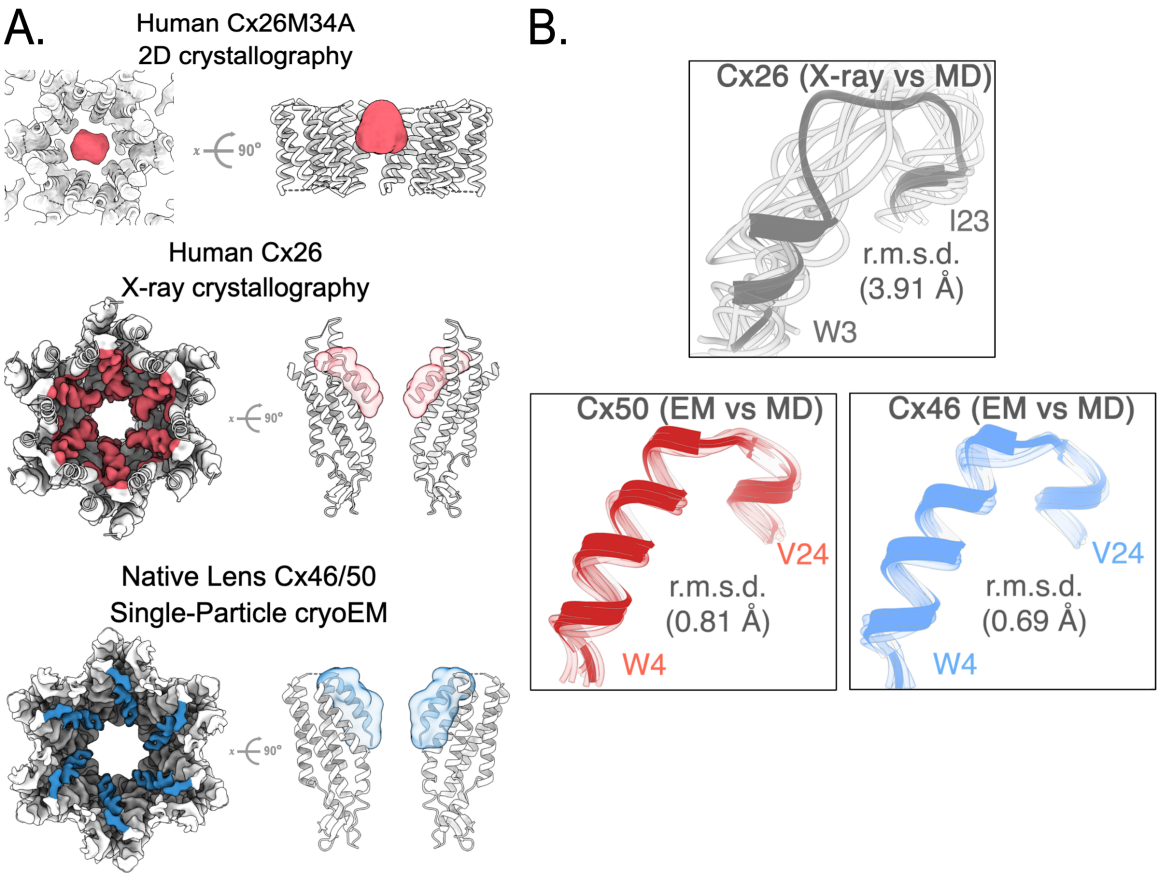

Figure 5 — Advances in connexin channel structural biology and models for the NTH gating domain conferred by the advent of single-particle cryoEM.

(A, top) 2D crystallography structure of Cx26M34A gap junction at ~10 Å resolution. This structure lent support to the putative 24-TMD architecture in each hemichannel (Cα trace; white). A "plug" density in the pore (coral) suggested that Cx26M34A was resolved in a closed conformation. ***(A, center)*** Human Cx26 was resolved to 3.5 Å by x-ray crystallography, providing sufficient detail for atomic modelling. The Cx26 NT domain is packed against the pore-lining TMs, which seemed to indicate the channel was resolved in an open-state conformation. ***(A, bottom)*** The single-particle cryoEM structure of native heteromeric Cx46/50 gap junctions at 3.4 Å resolution. Overall channel architecture resembles Cx26, with notable differences in the NT domain. ***(B)*** Myers, *et al* (Ref. 27) employed atomistic MD simulations to probe conformational stability in the NT between Cx26 and the cryoEM structures of Cx46/50. The Cx46/50 NT domains remain conformationally stable over ~500 ns of simulation time. Meanwhile, the Cx26 NT rapidly unfolded under identical simulation conditions. These observations ultimately point to ambiguity in the open/closed nature of the Cx26 crystal structure.

Early structural studies of the lens gap junctions

Junctional domains between lens fiber cells were first observed by electron microscopy studies of thin-sectioned tissues in the mid-70s[118,119]. A decade later, foundational biochemical characterization of lens fiber junctions uncovered a 70-kDa membrane protein (MP70) in lens fiber junctions (later termed connexin-50)[44,120]. The same group soon after showed that MP70 is absent from junctional domains of deeper-lying fiber cells in the lens core, where instead a 38-kDa membrane protein (MP38) is enriched[45,121–123]. Further characterization in sheep demonstrated that MP38 is a c-terminal cleavage product of MP70, and proteolytic conversion of MP70 to MP38 is dependent on Ca^{2+}-dependent protease activity from lens calpains[46].

The advent of modern molecular biology and recombinant DNA in the late-80s enabled cloning, recombinant expression, and biochemical isolation of connexin genes and their gene products. Cx43 and Cx50 were first identified as the protein components forming gap junctions in lens epithelium, while junctions in the differentiating and mature fibers were shown to be formed by Cx46 and Cx50[37,38,124]. Negative-stain electron microscopy (NSEM) of tissue slices and *in vitro* isolated MP70 and MP38 showed that gap junctions cluster into ordered hexagonal arrays[125–128]. These studies showed that gap junctional plaques feature a repeating unit with a stain-filled cavity, confirming the long-held speculation that fiber cell junctions feature a pore through which intercellular chemical exchange occurs.

The propensity for gap junctions to form ordered, quasi-crystalline arrays made connexins from a variety of tissues made these proteins very early targets for 2D electron crystallography (2DX) studies[129,130]. Some of the earliest 2DX structures came from natively isolated hepatocyte and cardiac gap junctions embedded in lipid bilayers[131–134]. This methodology provided the first 3-dimensional models for Cx43 gap junction channels[135–138], shedding light on the overall morphology of the junction-forming domains and the channel pore (Fig. 5). However, low-resolution diffraction consistently plagued these experiments and for this reason, 2DX structures of connexin channels fell far short of the atomic-level detail that this method was clearly capable of (*e.g.*, the lens water channel, AQP0, was resolved to 1.9 Å by 2DX methods)[139,140].

Gap junction structures by 2DX were limited to ~5-6 Å resolution[136,141,142], and while this was insufficient for atomic-level models, they nevertheless provided insight into gross details. For instance, functional studies demonstrating that connexin channels permeate a chemically diverse array of solutes up to ~ 1 kDa in size was largely confirmed by visualization of the ~1.5 nm diameter pore.[143,144]. Nevertheless, important ambiguities in connexin structure remained unresolved, such as the identity of pore-lining regions.[145].

One poignant example is the 2DX structure of the Cx26 M34A mutant (analogous to the deafness-associated M34T mutation)[141]. These crystals diffracted to ~10 Å and the density map was consistent with the proposed dodecameric subunit composition of gap junction channels. Intriguingly, the map revealed a prominent “plug” density in the pore, leading the authors to propose the

Cx26M34A mutant represents a closed or partially occluded state, consistent with electrophysiology experiments showing this mutation abolishes cell-to-cell currents (Fig. 5A, top). Deletion of the first 6 n-terminal residues (M34Adel2-7) diminished the plug density, suggesting involvement of the n-terminal helix in channel gating. Intriguingly, single channel permeabilities for wild-type and M34A Cx26 are comparable in reconstituted lipid bilayers[146], raising skepticism around the proposed closed state of Cx26M34A. With all these efforts in mind, high-resolution structural details for connexin channels remained highly sought after.

Atomic-level insight into the structure of the gap junctions

It wasn't until 2009 when a breakthrough from the groups of Tsukihara & Fujiyoshi yielded x-ray diffraction (XRD) data from crystals of recombinant human Cx26 at sufficient resolution to provide the first atomic model of a gap junction, resolved to 3.5 Å[25] (Fig. 5A, middle). The crystal structure of Cx26 confirmed that each connexin subunit contains 4 TMDs, and finally resolved the controversy that TM1/2 formed the pore-lining helices of these channels. The structure also provided key insight to understanding the electrostatic interactions between Cx26 ECDs that stabilize hemichannel docking to insulate the interior of the channel pore from the extracellular environment. Another major insight was the first visualization of the ~18 residue NTH domain, implicated in channel gating and substrate specificity. In the Cx26 crystal structure, the n-terminus is pointed downward and folded into the pore vestibule. Based on measurements of the major constriction sites throughout

the channel, the authors concluded that Cx26 was resolved in an open-state conformation.

The Cx26 crystal structure was a historical step toward understanding the structure and function of gap junctions. Nevertheless, many unanswered questions remained. For instance, how structurally conserved was Cx26 the other 20 human isoforms? Since lens gap junctions are heteromeric assemblies of Cx46/50, are there distinct isoform stoichiometries that affect channel structure? If so, how might structural variations inform functional properties observed by electrophysiology?

One curious aspect of the Cx26 crystal structure is in the NTH. The NTH itself has a somewhat amphipathic character, in which hydrophobic residues are positioned immediately adjacent polar and charged residues. Many hydrophobic side chains within the Cx26 NTH are oriented toward the solvent-exposed pore[25,27]. How can such an energetically unfavorable conformation be stabilized? One possibility posed was that crystal packing disrupted the native NTH open-state structure, trapping it in an alternative conformation with dubious physiological relevance[27]. Indeed, Cx26 channel permeability measurements paired with molecular dynamics simulations of Cx26 strongly suggest that the Cx26 crystal structure from Maeda, *et al* is not an open state[147–150].

Owing to the difficulty in growing high-quality crystals of membrane proteins, only a single x-ray crystallography study of a connexin channel has been published since Maeda, *et al* in 2009. To shed light on the mechanism of Ca^{2+} gating, Mark Yeager's laboratory succeeded in crystallizing Cx26 channels in the presence and absence of Ca^{2+} (20 mM)[105]. Unlike Maeda *et al*, the NTH was completely

unresolved, which precluded any insight into involvement of the n-terminus in gating. Difference map calculations identified a single Ca^{2+}-binding site in each Cx26 subunit (localized at Glu42 and Glu48) that introduces patches of positive charge along the permeation pathway of the dodecameric channel[105]. The authors proposed an electrostatic mechanism for Ca^{2+} gating in which a redistribution of positive charges in the pore under elevated cytoplasmic Ca^{2+} limits K^+ permeation and effectively uncouple cells. However, the electrostatic mechanism remains controversial, based on alternative models proposed by a combination of independent permeability studies and computational experiments[101,102,151,152].

The cryoEM resolution revolution opens new opportunities for gap junction structural biology

The explosive advance in single-particle cryoEM technology since the early 2010s has led to high-resolution structures of many macromolecular complexes that had been historically intractable to crystallography, in particular, membrane proteins were now in reach[153–158]. The Reichow laboratory determined the first single-particle cryoEM structure of a gap junction, native Cx46/50 channels isolated from mammalian lens (***Fig. 5A, bottom***), adding connexin assemblies to the nascent list of macromolecular complexes no longer hamstrung by the constraints of crystallography[27].

The most important revelation of the Cx46/50 cryoEM structure was a novel conformation for the NTH that differs markedly from Cx26 (***Fig. 5B***). Atomic models for Cx46 and Cx50, derived from the cryoEM density map, exhibit a much more

ordered NTH and conserved hydrophobic residues within the amphipathic helix are buried neatly in a hydrophobic cleft in the pore. This stands in stark contrast to the conformation modeled in Cx26, where these same residues were largely solvent-exposed[27]. The Cx46/50 NTH was remarkably stable over several 100ns of MD simulation, while under identical simulation conditions the Cx26 NTH rapidly unfolded[27] (***Fig. 5B***). This confirmed a long-held speculation that the Cx26 NTH conformation is energetically unfavorable and may not represent the open-state conformation that was the original interpretation by the authors.

Pushing the boundaries of cryoEM to uncover new insights into gap junction biology

Our research group has pioneered the application of single-particle cryoEM to gap junction structural biology and the structure of Cx46/50 was an important demonstration of the strengths of this methodology. Importantly, however, this is only the beginning: with the power of cryoEM at our disposal, there are countless questions to address about how Cx46/50 responds to the unique challenges of a surviving a life-long existence in the lens environment.

For the high-resolution structure from Myers *et al*, Cx46/50 channels required stabilization in the amphipol (amphipathic polymer) A8-35[27,159]. Amphipols substitute detergents at the aqueous-transmembrane interface of membrane proteins, providing an attractive alternative for stabilizing membrane channels in a detergent-free medium. While effective, amphipols cannot recapitulate the native lipid environment in which membrane proteins exist, and

therefore amphipol-stabilization inevitably lacks insight into how Cx46/50 interacts with the lipid environment of the lens.

Furthermore, while the 3.4 Å resolution depiction of Cx46/50 from Myers *et al* was sufficient for *de novo* atomic modeling, important details remain missing. Many side chain conformations in the cryoEM map remained somewhat ambiguous, including pore-lining residues that contribute to the permeation pathway. CryoEM maps that surpass ~3 Å resolution can reliably guide unambiguous rotamer assignment[160]. To disambiguate solvent/ion interactions, greater than ~2.5 Å is necessary[161]. Experimental structures with this degree of information content are invaluable for integral membrane proteins, since solvent and ion interactions are inextricably linked to regulatory mechanisms in these proteins. For instance, the identity of the Ca^{2+} gate in connexin channels remains a highly active area of study—not least of all because published connexin channel structures in the presence of Ca^{2+} have yet to unambiguously link *bona fide* Ca^{2+}-binding sites to a discrete gating mechanism.

For my thesis, I address these gaps in knowledge, by employing a combination of methods in membrane protein biochemistry and cryoEM single-particle analysis to determine structures of lens Cx46/50 in environments that recapitulate native lens conditions. In Chapters 2 & 3, I describe structures of Cx46/50 in a near-native lipid environment mimicking conditions of a healthy young lens, as well as high-resolution structures of Cx46/50 in conditions that recapitulate the cholesterol enrichment that occurs in aged lens core. In Chapter 4, I describe cryoEM structures of Cx46/50 that shed an unprecedented light on the molecular

basis for Ca^{2+}-induced cellular uncoupling. Finally, in Chapter 5, I provide a perspective on the future of connexin channel structural biology in the “resolution revolution” era of cryoEM, and how the niche cryoEM now occupies can further enhance our understanding of the structure and function of gap junctions moving forward.

Chapter 2: Connexin-46/50 in a dynamic lipid environment resolved by cryoEM at 1.9 Å

Authors: Jonathan A. Flores[1,†], Bassam G. Haddad[2,†], Kimberly A. Dolan[2,3,†], Janette B. Myers[2], Craig C. Yoshioka[4], Jeremy Copperman[4], Daniel M. Zuckerman[4] and Steve L. Reichow[1,2,*]

Affiliations:

[1] Department of Chemical Physiology and Biochemistry, Oregon Health and Science University, Portland OR 97239, U.S.A.

[2] Department of Chemistry, Portland State University, Portland OR 97201, U.S.A.

[3] Current Address: Biophysics Graduate Group, University of California, Berkeley, CA 94720, U.S.A.

[4] Department of Biomedical Engineering, Oregon Health and Science University, Portland OR 97239, U.S.A.

[†] Indicates equal contribution

* corresponding author (reichow@pdx.edu)

Respective Contributions

J.A.F, B.G.H and K.A.D. contributed equally. K.A.D. and J.A.F. conducted the protein purification and reconstitution of cryoEM specimens. J.A.F. collected the cryoEM datasets, performed image analysis and atomic modeling. K.A.D., J.B.M., C.C.Y. contributed to image analysis. B.G.H. conducted and analyzed the MD simulations. B.G.H., J.C. and D.M.Z. contributed to the experimental design and

analysis of MD simulations. All authors contributed to manuscript preparation. S.L.R. provided overall guidance to the design and execution of the work.

Publshed in: Flores JA, Haddad BG, Dolan KA, Myers JB, Yoshioka CC, Copperman J, Zuckerman DM & Reichow SL (2020). Connexin-46/50 in a dynamic lipid environment resolved by CryoEM at 1.9 A. Nat Commun 11, 4331.

Abstract

Gap junctions establish direct pathways for cells to transfer metabolic and electrical messages. The local lipid environment is known to affect the structure, stability, and intercellular channel activity of gap junctions; however, the molecular basis for these effects remains unknown. Here, we incorporated native connexin-46/50 (Cx46/50) intercellular channels into a dual lipid nanodisc system, mimicking a native cell-to-cell junction. Structural characterization by cryoEM revealed a lipid-induced stabilization to the channel, resulting in a 3D reconstruction at 1.9 Å resolution. Together with all-atom molecular dynamics simulations, it is shown that Cx46/50 in turn imparts long-range stabilization to the dynamic local lipid environment that is specific to the extracellular lipid leaflet. In addition, ~400 water molecules are resolved in the cryoEM map, localized throughout the intercellular permeation pathway, and contributing to the channel architecture. These results illustrate how the aqueous-lipid environment is integrated with the architectural stability, structure, and function of gap junction communication channels.

Introduction

The connexins are a family of transmembrane proteins (21 isoforms in human) that form intercellular channels for cell-to-cell communication[24,162]. These intercellular channels establish a ~1.4 nm pore that couples the cytoplasms of neighboring cells, and enable direct passage of electrical and small molecule signals (such as, ions, second messengers, hormones and metabolites)[163] and therapeutic agents[164]. 10's – 1000's of connexin channels may assemble to form large hexagonally packed arrays, *a.k.a*. plaques, known as gap junctions. In this way, gap junctions enable the near instantaneous response of electrical synapses in the brain and heart, and contribute to the long-range signaling and metabolic coupling of most tissues. Because of these fundamental roles, aberrant gap junctional coupling is associated with a variety of human diseases, including blindness, deafness, skin disorders, arrhythmia, stroke and cancers[107,110,117,165].

Gap junction intercellular communication is facilitated by a unique macromolecular architecture, where intercellular channels directly couple the cytoplasms of two neighboring cells. The lipid bilayers of opposing cells are separated by a characteristic gap of ~3.5 nm[131,132], a feature for which these structures were first recognized in electron micrographs of cell sections[35,166]. Furthermore, large-scale gap junctional plaque formation is dependent upon a dense mosaic of protein-lipid interactions. *In vitro* reconstitution studies have established that plaque assembly and intercellular channel function are dependent on the lipid environment[89,91,98,128,167,168]. However, the molecular basis for these

effects remains largely unknown, due to the lack of high-resolution structural information within a lipid bilayer.

Here, we present a cryoEM structure of native connexin-46/50 (Cx46/50) intercellular channels stabilized in a dual lipid nanodisc system at 1.9 Å resolution—providing an unprecedented level of detail for this class of membrane channel. These structural results are coupled with all-atom molecular dynamics (MD) simulation studies, which together reveal many architectural and proposed functional features of the connexin channels. Cx46/50 is shown to have a remarkable influence on the local lipid environment, effectively inducing a phase separation (to the gel state) that is specific to the extracellular lipid leaflet of the two opposed membranes. 3D heterogeneity analysis of the cryoEM data identified multiple lipid configurations that co-exist within the dynamic lattice of stabilized lipids, which is further detailed by MD. In addition, ~400 water molecules are resolved in the cryoEM map, localized at architectural and functionally important sites. Together this work uncovers previously unrecognized roles of the aqueous-lipid environment in stabilizing the structure and assembly of the gap junctions and suggests Cx46/50 plays an important role in shaping the properties of local membrane environment.

Results

Structural overview of connexin-46/50 in a lipid environment

Native (heteromeric/heterotypic) connexin-46/50 intercellular channels were purified from mammalian lens tissue (obtained from sheep)[27]. Freshly purified

channels were reconstituted into self-assembling lipid nanodiscs containing pure dimyristoyl phosphatidylcholine (DMPC) at room temperature (~25° C), supported by the membrane scaffold protein MSP1E1[169,170] (see Methods). Under optimized conditions, the reconstitution resulted in a monodispersed population of intercellular channels embedded into a pair of lipid-nanodiscs, as assessed by size-exclusion chromatography and negative stain EM (Supplementary Fig. 1).

Structure determination by high-resolution single particle cryoEM resulted in a high-quality 3D reconstruction, with an overall resolution of 1.90 Å (gold-standard FSC) (Fig. 1a,b, Supplementary Fig. 2,3 and Supplementary Movie 1). The quality of the cryoEM map allowed for detailed stereochemical structural refinement of both Cx46 and Cx50 (Fig. 1b, Supplementary Table 1 and Supplementary Fig. 3). The heteromeric pattern(s) of Cx46/50 co-assembly remain unresolved, following various attempts at computational image classification (see Methods). Nevertheless, atomic models of both Cx50 and Cx46 isoforms were equally well-fit into the D6-symmetrized cryoEM map, reflecting their close sequence and structural similarities, 89% sequence similarity over the structured regions and a resulting 0.17 Å backbone r.m.s.d. (see Methods and Supplementary Fig. 3 for details and limitations regarding the heterogeneity of the natively isolated specimen).

Cx46/50 is captured in the stabilized open-state, as previously described[25] (backbone Cα r.m.s.d. = 0.49–0.56 Å and Supplementary Fig. 5), and exposes many new features of the connexin channels that are detailed below. Intercellular

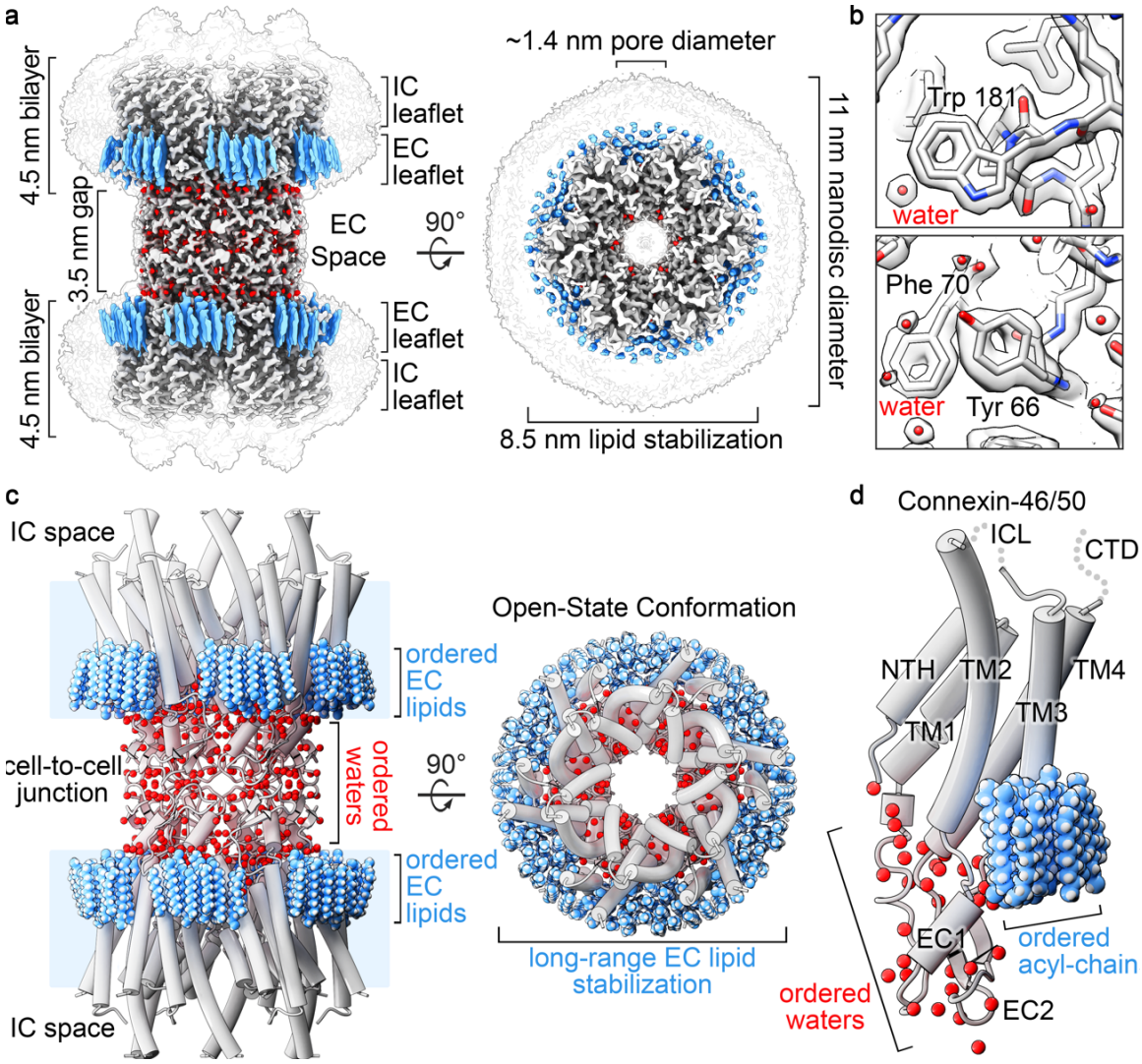

Figure 1. Structure of connexin-46/50 in lipid nanodiscs by cryoEM.

a) CryoEM 3D reconstruction of Cx46/50 (white) in an open state conformation, with resolved lipid acyl-chains (blue) and waters (red). Transparent silhouette displays the lipid nanodisc densities at low contour, with intracellular (IC) and extracellular (EC) lipid leaflets indicated. **b)** Zoom views of the cryoEM map with atomic models fit to illustrate high-resolution features observed in the 1.9 Å resolution consensus refinement. **c)** Model of Cx46/50 (tube representation) with EC lipids and ordered waters displayed (spheres). **d)** Cx46/50 monomer. 15 bound lipids and 33 waters are associated with each subunit. Domains labeled for transmembrane helices (TM1-4), EC loops (EC1-2) and n-terminal helix (NTH). The disordered intracellular loop (ICL) and c-terminal domain (CTD) are not resolved (dotted lines).

channels are constructed by a dodecameric (12-mer) assembly, with six subunits assembled into 'hemi-channels' that dock together through extracellular domains, resulting in a continuous ~1.4 nm pore for intercellular permeation (Fig. 1a,c and Supplementary Movie 2). The distance separating the two lipid nanodisc densities is ~3.5 nm (Fig. 1a,c), matching that observed by x-ray diffraction on native gap junctional plaques[131,132].

Each monomer consists of four transmembrane helices (TM1-4), two extracellular loops (EC1-2) that form the sites of docking interaction and an amphipathic n-terminal helix (NTH), implicated in channel selectivity/gating, is well resolved in the stabilized open-state, as previously described[27] (Fig. 1c,d and Supplementary Movie 3). However, the significant enhancement in resolution allowed for detailed refinement of sidechain conformations and notable improvement in precision at functional sites, including the NTH domain and the EC1/2 docking sites (Supplementary Fig. 3,5). Furthermore, the quality of the cryoEM map allowed for modeling previously un-resolved regions of TM2 and TM3, which effectively extend the cytoplasmic vestibule of the channel by ~20 Å, as compared to our previous model (Fig. 1c,d), significantly augmenting the electrostatic environment of the pore entrance (Supplementary Fig. 5). The intracellular loop (ICL) and c-terminal domain (CTD) remain unresolved, presumably due to intrinsic disorder of these regulatory domains[25,27,105].

Perhaps the most remarkable features of the cryoEM map, however, are the non-protein components of the cell-to-cell junction that are now resolved. A bouquet of 15 ordered lipid acyl-chains is held in place by each of the 12 connexin

subunits, which appear to buttress the channel assembly by filling a cavity formed at the lateral subunit interfaces (Fig. 1a,c,d; blue). Surprisingly, acyl-chain densities are observed well beyond the first layer of annular lipids that directly interact with the TM domains (primarily TM4 and TM3 of a neighboring subunit) (Fig. 1c,d and Supplementary Fig. 6), suggesting Cx46/50 has a long-range effect on the stability and biophysical properties of the membrane. Remarkably, all resolved lipid densities in the cryoEM map are specifically localized to the extracellular leaflet of the bilayer, indicating a selective interaction with the local lipid environment. In contrast, individual lipids are not resolved in the intracellular leaflet, even at lower contour levels (Fig. 1a and Supplementary Fig. 2) likely due to intrinsic disorder and/or lack of specific interaction with this region of the channel.

In addition to stabilized lipids, 396 ordered water molecules are resolved throughout the channel (33 waters per subunit) (Fig. 1,2; red and Supplementary Fig. 6). Waters are found at both solvent accessible and buried sites within the core of the channel, apparently contributing to the permeation pathway and structural integrity of the channel assembly (Fig. 1,2). The assignment of water densities was validated by assessment of hydrogen bonding patterns (< 4 Å donor-acceptor distances) and supported by comparison to all-atom equilibrium MD simulations conducted in the presence of explicit water and 150mM NaCl or KCl (see Methods and Supplementary Fig. 7,8). There was no clear evidence that the resolved solvent sites correlated with low-affinity ion binding sites observed by MD (not shown). In the following sections, we describe these resolved features in further detail and discuss their potential structural and functional roles.

Roles of stabilized waters in Cx46/50 intercellular channels

Gap junctions establish aqueous pathways that allow a variety of cytosolic substrates, less than ~1 kDa in size, to permeate from cell to cell[171]. The permeation pathway is established by the pore-lining NTH domain, TM1/2 and EC1 domains (Fig. 1c,d). Within the channel pore of Cx46/50, there are 108 waters bound at solvent-exposed sites (9 per subunit). Pore-bound waters localize to regions of the EC1 domain and TM1 parahelix, and mediate an extensive network of h-bonding interactions, involving, D42, F43 (bonding), E48, Q49, N63 and R76 in Cx50 (positions 42 and 43 are Glu in Cx46), and several protein backbone interactions (Fig. 2a,b and Supplementary Fig. 6).

EC1 and the TM1 parahelix contribute to the selectivity, conductance and slow (loop) voltage-gating mechanisms of Cx46/50[27,172–174] and other

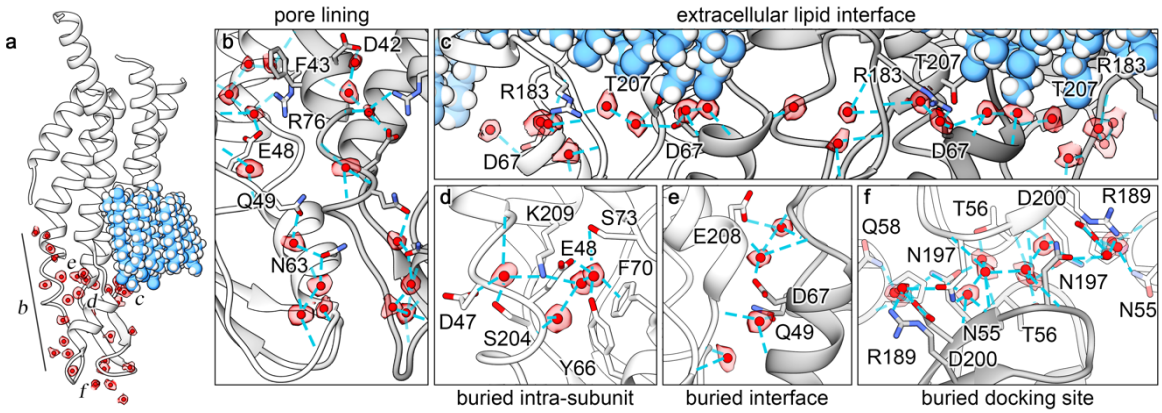

Figure 2. Ordered water molecules resolved in Cx46/50 by cryoEM.

a) Cx46/50 subunit with segmented CryoEM density of waters overlaid in transparency (colored as in Fig. 1). Labels in panel a indicate position of zoom views, presented in panels **b–f**, showing water molecules bound to **b)** pore-lining sites, **c)** extracellular lipid interface, **d)** buried intra-subunit sites, **e)** buried subunit interface sites, and **f)** buried cell-to-cell docking sites. In panels b-f, amino acids sidechains forming hydrogen bonds to water are displayed (blue dashed lines) and labeled using Cx50 numbering.

connexins[147,149,175–178], and are implicated in Ca^{2+}-regulation in Cx26 by X-ray crystallography[105], MD studies[101,149], and by functional mutation studies of Cx46[101]. As such, these pore-lining waters may functionally contribute to these mechanisms, for example, by orienting or extending the hydrogen-bonding potential of amino-acid sidechains involved in the coordination of substrates (or regulatory ions), buffering the electrostatic properties of the channel pore, or integrating the electrostatic network that is proposed to couple EC1/TM1 to the fast (NTH) voltage-gating domain[179,180].

On the extracellular surface of the channel, symmetry-related rings of tightly bound water molecules are organized at the extracellular aqueous-lipid boundary (Fig.1a,c and Fig. 2a,c). In the ensemble cryoEM map, the PC lipid head groups are not resolved (due to local disorder described in the following sections). Nevertheless, these stabilized rings of water are nominally positioned at the acyl-headgroup boundary of the extracellular lipid leaflet. These waters are stabilized by hydrogen bonds with EC1/2 residues (D67, R183/Q171 and T207/T195 in Cx50/Cx46, respectively) and expected to be further coordinated through non-specific interactions with the phospho-glycerol backbone of the extracellular PC lipids (Fig. 2c; and discussed below).

The EC1/2 domains appear to be the most well-ordered region of the channel, as reflected by local-resolution of the cryoEM density map (Supplementary Fig. 3) and root-mean-square-fluctuation (r.m.s.f.) analysis of MD-trajectories (Supplementary Fig. 7) This high-degree of stability reflects the important functional role of the EC1/2 domains in maintaining an electro-chemical

seal at the cell-to-cell junction. Several clusters of water molecules are found buried a sites located both within and between the EC1/2 domains of individual subunits (Fig. 2a, d-f). A cluster of four waters are buried within the EC1/2 domains is coordinated by residues D47, E48, Y66, F70 (bonding), S73, S204/S192 and K209/K197, in Cx50/46 respectively (Fig. 2d). Four additional waters are buried at the lateral EC domain interface formed by neighboring subunits, primarily coordinated by hydrogen bonding interactions with the peptide backbone and sidechains of Q49, D67 and E208/E196, in Cx50/Cx46 respectively (Fig. 2e). The degree of coordination of these buried waters suggest they contribute to the architectural integrity of EC1/2 docking domains and may in part explain why deleterious mutations at D47, E48 and D67 in Cx50 linked to cataract formation disrupt junctional coupling and/or biogenesis[181–183].

The EC1/EC2 domains also play important roles in establishing the specificity of hemi-channel docking interactions formed between different connexin isoforms, and the ability to establish so-called homotypic or heterotypic channels[184–186]. Elucidating the determinants of hemi-channel recognition is therefore critical to understanding the principles dictating cell-type specificity of gap junctional coupling[187]. It has been proposed that isoform-specific hydrogen bonding patterns that bridge the EC1/EC2 interface govern hemi-channel docking compatibility[186,188]. Contributing to this bridging site in Cx46/50 is a cluster of 12 water molecules (per subunit pair) that are deeply integrated within a dense network of hydrogen bonds between EC1/EC2 residues of opposed subunits (Fig. 2f). At the center of this network is the highly conserved K/R-N-D motif found in

EC2 of Group I compatible connexins (including Cx50, Cx46, Cx32 and Cx26). Genetic mutations of this motif in Cx46/50 are linked to congenital cataracts[27,189], as well as other genetic disorders (*e.g.,* Charcot-Marie-Tooth disease[190] and non-

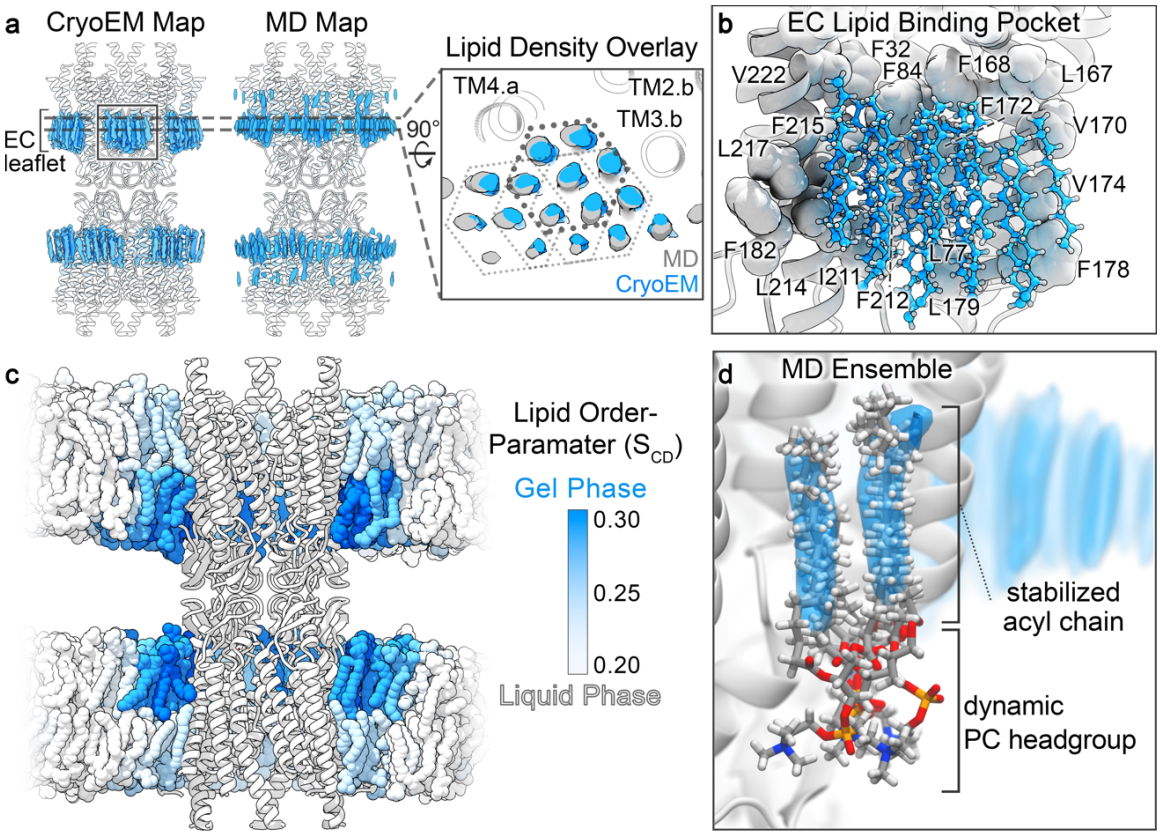

Figure 3. Cx46/50 induces a local phase-separation to the extracellular lipid leaflet.

a) Comparison of acyl-lipid density maps (blue) obtained by cryoEM and time-averaged all-atom MD-simulation, overlaid onto the Cx46/50 ribbon structure (white). *Inset,* shows a slice-view (rotated 90°) of overlaid acyl-lipid densities by cryoEM (blue) and MD-simulation (grey). The hexagonal packing pattern of acyl-chains is indicated (solid and dotted lines), and TM helices interacting with lipid are labeled. Different subunits are indicated by suffix (*a* or *b*). **b)** Zoom-view of the acyl-lipid binding pocket, with lipid-binding residues displayed (spheres) and labeled (Cx50 numbering). **c)** MD-snapshot of Cx50 in phosphatidylcholine (PC) lipid bilayers, with time-averaged lipid order parameter (S_{CD}) for each lipid indicated by shading (blue = 0.30 to white = 0.20). **d)** Zoom view, showing an ensemble super-positioning of symmetry-related lipids obtained by MD-simulation (displayed as all atom representation, C = grey, H = white, O = red, N = blue, P = orange) occupying the MD-based lipid acyl-chain density map (blue).

syndromic deafness[191]), when mutated in other Group I connexins. These observations suggest interfacial waters may play previously unappreciated and functionally important roles in establishing the structural integrity of the intercellular channel and contribute to the specificity of hemi-channel docking interactions involved in regulating the formation of intercellular communication pathways.

Long-range ordering of the extracellular lipid leaflet

The degree of long-range stabilization to the local lipid environment observed in the Cx46/50 nanodisc reconstruction is extraordinary, extending several solvent layers away from the protein. DMPC was selected as a model lipid because of the high PC content of mammalian (sheep) lens[192], and reconstitution studies show DMPC produces Cx46/50 assemblies that are indistinguishable from those formed with native lipids[125,128]. Due to its complete saturation DMPC has a relatively high phase-transition (i.e., melting) temperature (T_m) compared to other biological lipids (T_m ~24° C in pure lipid vesicles[193]). This value is close to the temperature at which reconstitution was performed (~25° C, room temperature). However, in nanodiscs the melting temperature of DMPC is reportedly higher (~28° C), due to compartmentalization effects by the MSP scaffold[194]. Nevertheless, the specific localization of stabilized lipids to the extracellular leaflets observed by cryoEM (and by MD; described below) suggested long-range lipid stabilization is induced through interactions with Cx46/50 (Fig 1, 3a).

To gain further insight into the lipid-stabilization observed by cryoEM, we analyzed time-averaged densities of DMPC acyl-chain positions obtained by

unbiased all-atom MD simulations for both Cx50 and Cx46, conducted at 37° C, where the starting positions of DMPC molecules had been randomly placed into a 15.4 x 15.4 nm lipid bilayer (see Methods and Supplementary Fig. 7a). Following equilibration, the resulting acyl-lipid density profiles displayed remarkable similarity to what was resolved by cryoEM (Fig. 3a). In both cases, lipids within the extracellular leaflets are specifically stabilized, as compared to the intracellular lipid leaflet (Fig. 3a). Furthermore, the resolved clusters of acyl-chain densities obtained by MD display the same hexagonal packing pattern that extends 3-4 orders beyond the annular shell, as observed by cryoEM (Fig. 3a, inset).

The corroborating results obtained by MD imply that the lipid stabilization observed by cryoEM is specifically induced by structural features of the Cx46/50 TM domains, and not an artifact of the nanodisc. Each cluster of lipids is bound by a shallow pocket of hydrophobic and aromatic residues, displayed by TM2/3 and TM4 of adjacent subunits (Fig. 3a,b). A cleft, rich in aromatic sidechains (formed by F32, F84, L167/L155 and F168/F156 in Cx50/C46, respectively) intercalates into the bilayer, appearing to bisect the extracellular leaflet from the more disordered intracellular leaflet (Fig. 3b). In this way, it appears that the acyl-lipid binding pocket selectively grasps a large bouquet of lipids from the extracellular leaflet, inducing long-range stabilization to the membrane through extensive Van der Waals interaction.

The extended acyl-lipid chain conformation and hexagonal packing adopted by the bouquet of bound lipids are indicative of a quasi phase-transition to the liquid-ordered (or gel-like) state. To obtain a more quantitative assessment of the

degree of lipid stabilization, we extracted SN1 and SN2 lipid order parameters (S_{CD}) from the MD-simulations, which have been parameterized to fit well to experimental NMR-based order parameters[195]. These results are consistent with

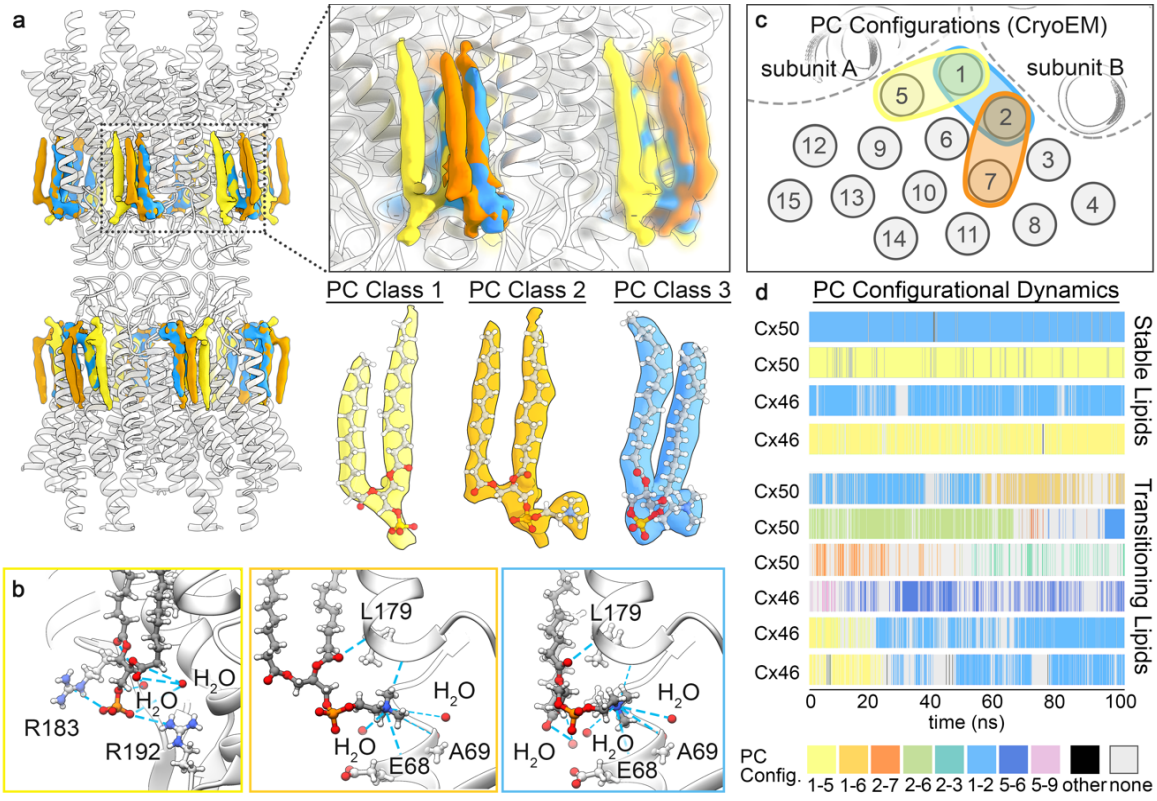

Figure 4. PC lipid configurational heterogeneity and dynamics resolved by cryoEM and MD. **a)** Segmented PC density maps obtained by cryoEM 3D heterogeneity analysis and classification (PC Class 1 – yellow, PC Class 2 – orange, PC Class 3 – blue). *Insets* show zoom views of overlapping features in resolved lipid configurations. Segmented densities with fitted atomic models are also shown. Density for non-unique acyl-lipid chains, with unresolved head groups, have been omitted for clarity. **b)** Zoom-view, showing Cx50 hydrogen bonds (blue dashed line) between the PC lipid headgroup and phosphoglycerol backbone. Side chain and stabilized solvent interactions are labeled. Yellow box – PC Class 1, orange box – PC Class 2, blue box – PC Class 3. **c)** Illustration of acyl-chain positions and overlapping configurations resolved by cryoEM (represented as grey circles and numbered 1 – 15). **d)** PC configurational classification and dwell times obtained by all-atom MD-simulation, showing representative populations of stable (non-transitioning) and dynamic (transitioning) lipids. PC configurations were classified by acyl-chain occupancy in densities numbered as in panel c, and colored uniquely (as indicated, bottom of panel d).

the notion that lipids in the intracellular leaflet are maintained in a fluid state, while Cx46/50 induces a phase transition from a fluid to a gel-like state that is specific to the extracellular lipid leaflet, as indicated by a shift in order parameters to above ~0.25[196] (acyl-chain carbons 4–11; Fig. 3c and Supplementary Fig. 9), which extend ~10–20 Å from the protein surface, as observed by cryoEM.

Although this degree of stabilization to the local lipid environment is likely to depend on lipid type, the general effects may be functionally important. For example, by contributing to the architectural integrity at the gap junctional interface, partitioning specific types of lipids, or even templating long-range hexagonal packing interactions found in plaque assemblies[125,131]. In this context, it is noteworthy that connexins localize to lipid raft domains[197,198], which are rich in high T_m lipids (e.g., sphingomyelin) and characterized as forming a liquid-ordered state.

Dynamic lipid configurations captured by cryoEM and MD

Another notable feature of the lipid densities observed in the cryoEM map is that PC head groups are not observed, despite sufficient resolution to expect such features (Fig. 1, 3a). Super-positioning of representative lipid conformations obtained by MD show that, although the annular lipid acyl-chains were relatively well ordered and superimpose, their corresponding head groups remain conformationally dynamic and/or heterogeneously positioned (Fig. 3d and Supplementary Movie 4). Such behavior would rationalize the lack of resolvability in the averaged cryoEM density map. In an attempt to resolve this heterogeneity, we conducted 3D-classification analysis on the ensemble cryoEM data (Methods

and Supplementary Fig. 4), which resulted in three distinct 3D reconstructions resolved at resolutions of ~2.5 Å (gold-standard FSC) (Fig. 4a-c and Supplementary Fig. 4).

In each of the 3D classes, PC head groups and/or phosphoglycerol backbone of individual annular lipids were uniquely resolved (PC Class 1–3, Fig. 4a). The conformational state of Cx46/50 is very similar in all three classes, and essentially indistinguishable from models derived from the ensemble density map (Cα r.m.s.d. = 0.24 – 0.34 Å). Notably, structural features of each fully-resolved lipid are shared amongst these classes. For example, the SN2 acyl-chain of PC Class 1 overlays with the SN1 chain of PC Class 3 (Fig. 4a,c; yellow and blue). Likewise, the SN1 chain of PC Class 2 also overlays with the SN1 chain of PC Class 3 (Fig. 4a,c; orange and blue). This suggested that multiple, overlapping, configurational states can support the same lattice of acyl-chain positions observed in the cryoEM reconstructions, consistent with non-specific and/or transient binding interactions.

The choline head group of PC Class 1 remained unresolved, however the negatively charged phospho-glycerol backbone is clearly visualized and appears to be stabilized by flanking positively charged arginine residues R183 and R192 in Cx50 (Q171 and R180 in Cx46) (Fig. 4b; left), and hydrogen bonding with two water molecules (part of the belt of extracellular waters described above, see Fig. 2c). PC Class 2 and 3 resolve distinct acyl-chain configurations, yet, both of these states share a similar placement of their positively charged choline head groups. Head group placement of these lipids is supported by non-specific hydrogen-bond

interactions with backbone carbonyls presented by EC1 and TM3 (involving residues E68, A69 and L179 in Cx50; position 68 is an Arg in Cx46) and a buried water molecule (Fig. 4b; center and right). The phospho-glycerol backbones of PC Class 2/3 lipids are coordinated by hydrogen-bonding to local waters and the backbone amide of L179 in Cx50 (L167 in Cx46). Remarkably, the SN2 acyl chain and glycerol backbone of the PC Class 2 lipid is completely resolved, despite lacking any direct contact with the Cx46/50 protein interface (Fig. 4a,c).

Collectively, these observations support the notion that while the Cx46/50 acyl-chain interactions appear to be high-affinity, the lipid head group interactions are nonspecific and adopt a variety of configurational/conformational states. This is reinforced by our MD-simulation studies for both Cx50 and Cx46, where mapping of PC arrangements at resolved acyl-chain densities show a variety of configurational states that co-exist within the dodecameric assembly. Furthermore, during the timescale of the simulations (100 ns), time-resolved PC configurations could be classified as being either stable or dynamically transitioning between multiple configurational states (Fig. 4d and Supplementary Movie 5,6). Notably, the most stable (yet overlapping) configurations (*e.g.,* 1-2 and 1-5 configurations) are the same as those resolved by cryoEM 3D classification (Fig. 4a,c,d; blue and yellow respectively). Yet, other lipid trajectories were observed interconverting between these same configurations over this relatively short time-scale (Fig. 4d). The degree of configurational preference diminishes beyond the first two solvent shells, presumably due to the loss of energetic influence induced by protein interactions (Fig. 4d), and reflect the randomized head group arrangements

expected of a bulk lipid population. Taken together, these data show Cx46/50 stabilizes the dynamic local lipid environment through non-specific interactions with the extracellular leaflet, with multiple configurational PC lipid states existing at the annular interface and effectively captured by cryoEM.

Discussion

The structure and function of membrane proteins are deeply integrated with their lipid environment. Our mechanistic understanding of protein-lipid interactions have been largely shaped by high-resolution structures of membrane proteins where specifically bound lipids have been captured at well-defined binding sites[199]. Yet, most interactions made between membrane proteins and their local membrane environment are relatively non-specific and highly dynamic. The mechanistic principles and biophysical consequences underlying such interactions remains poorly understood, as these interactions are typically lost during protein purification, or remain too dynamic to resolve by traditional structural methods. By exploiting the potential of lipid nanodisc technologies coupled with single-particle cryoEM and MD simulation, we show that Cx46/50 intercellular communication channels form dynamic interactions with annular lipids. These non-specific interactions have long-range stabilizing effects capable of inducing a phase separation to high T_m lipids, which may extend ~20 Å from the protein surface. These interactions appear selective toward the extracellular leaflet of pure PC membranes, which may have significant consequences on the biomechanical properties and lipid composition of gap junctional domains. In fact, the lack of resolved lipids in the intracellular leaflet

may reflect the selectivity at this leaflet toward non-PC lipid types, as suggested for Cx26/32[98]. The methods developed here provide a valuable high-resolution platform for developing our deeper understanding of the specificity and physiological role lipids play in gap junction biology, and how aberrant lipid environments may contribute to connexin-related pathologies. Indeed, the capability of resolving connexin channels beyond the critical threshold of ~2.0–2.5 Å resolution, the precision desired for structure-based drug design – *e.g.,* providing detailed stereochemical models and placement of architectural water molecules – now opens the door to rational development of selective high-affinity pharmacological tools that are desperately needed in this field to better understand and potentially treat a wide range of connexin-opathies[200].

Methods

MSP expression and purification

A plasmid containing the coding sequence for membrane scaffold protein 1E1 (MSP1E1) was obtained from Addgene[169] and the protein was expressed and purified as described[170], with minor modification. Freshly transformed *E. coli* cells (BL21Gold-DE3) were grown in LB medium containing 50 μg mL^{-1} kanamycin at 37° C with shaking (250 rpm). Induction with 0.5 mM Isopropyl β-d-1-thiogalactopyranoside (IPTG) was performed when OD_{600} reached 0.5–0.6, and allowed to express for 3–5 hours post-induction at 37° C. Cells were harvested by centrifugation at 4,000 x *g* for 20 minutes at 4° C, and cell pellets were resuspended in MSP Lysis Buffer (40 mM Tris [pH 7.4], 1% Triton X-100, 1 mM PMSF) at a density of ~20 mL of Lysis Buffer per Liter of culture. Cell suspensions were flash frozen in liquid nitrogen and stored at –86° C for up to several months.

Frozen cell suspensions were thawed from –86° C storage, supplemented with 1 mM phenylmethylsulfonyl fluoride (PMSF) and lysed by sonication on ice. Crude lysate was cleared by ultra-centrifugation at 146,550 x *g* for 30 minutes at 4° C. The supernatant was filtered (Millipore; 0.22 μm) and applied to a gravity column with 5 mL of HisPur Ni-NTA resin (Thermo Fisher Scientific) prepared in equilibration buffer (40mM Tris [pH 7.4]). MSP-bound resin was washed with 5 column volumes (CV) of equilibration buffer, followed by 5 CVs of each of the following: Triton buffer (40 mM Tris [pH 8.0], 300 mM NaCl, 1% TX-100), Cholate buffer (40 mM Tris [pH 8.0], 300 mM NaCl, 50mM cholate), Imidazole Wash Buffer (40 mM Tris [pH 8.0], 300 mM NaCl, 50 mM imidazole). MSP1E1 was eluted with

3 CVs of Elution Buffer (40 mM Tris [pH 8.0], 300 mM NaCl and 750 mM imidazole). The eluate was filtered (Millipore; 0.22 μm) and applied to a size exclusion chromatography (SEC) column (ENC70; BioRad) equilibrated in 20 mM HEPES (pH 7.4), 150 mM NaCl and 1 mM EDTA using an FPLC (NGC system; BioRad). Peak fractions were monitored by UV_{280}, pooled and concentrated to 400-600 μM using a centrifugal device. Final protein concentration was determined by UV absorbance at 280 nm. Samples were aliquoted, flash frozen in liquid nitrogen and stored at –86° C for up to several months.

Cx46/50 purification and nanodisc reconstitution

Native Cx46/50 intercellular channels were isolated from native lens fiber cells from sheep[27]. Briefly, lamb eyes were obtained from the Wolverine Packers slaughterhouse (Detroit, MI), and the lenses were removed using a surgical blade and stored at –86° C. Gap junction intercellular channels were isolated from the core lens fiber tissue, containing c-terminal truncation variants of Cx46 and Cx50 (a.k.a. MP38)[37,45,122]. Details of the purification procedure are provided below.

Lenses were thawed from –86° C, core lens fiber cell tissue was dissected from the outer cortical tissue using a surgical blade and stripped core membranes were prepared as described[201–203]. Total protein concentration was determined by BCA (Pierce) and membranes were stored at –86° C, in storage buffer (10 mM Tris [pH 8.0], 2 mM EDTA, 2 mM EGTA) at a total protein concentration of ~2 mg mL^{-1}. Stripped membranes were thawed from –86° C and solubilized with 10 mM Tris (pH 8.0), 2 mM EDTA, 2 mM EGTA, 1% (wt vol^{-1}) n-decyl-β-D-maltoside (DM)

for 30 minutes at 37° C. Insoluble material was cleared by ultra-centrifugation at 146,550 x *g* for 30 minutes at 4° C. The supernatant was filtered (Millipore; 0.22 μm) and separated by anion-exchange chromatography (UnoQ, BioRad) with buffer A (10 mM Tris [pH 8.0], 2 mM EDTA, 2 mM EGTA, 0.3% DM [wt vol^{-1}]). Protein was eluted with a 20 CV gradient of buffer B that additionally contained 500 mM NaCl. Elution peaks containing Cx46/50, as determined by SDS-PAGE, were pooled and applied to a size exclusion chromatography (SEC) column (Superose 6 Increase 10/300 GL; GE Healthcare) equilibrated with SEC buffer (20 mM HEPES [pH 7.4], 150 mM NaCl, 2 mM EDTA, 2 mM EGTA and 0.3% DM [wt vol^{-1}]). Peak fractions containing purified Cx46/50 were pooled and concentrated to 5–6 mg mL^{-1} with a centrifugal device (Vivaspin 6; 50-kDa cut-off filter; Sartorius). Protein concentration was determined by UV absorbance at 280 nm. All chromatography steps were performed by FPLC at 4° C.

Freshly purified Cx46/50 was reconstituted into MSP1E1 nanodiscs using dimyristoyl phosphatidylcholine (DMPC) lipids, following established procedures[170,204]. Chloroform-solubilized DMPC (Avanti) was dried under nitrogen gas and left under vacuum overnight to remove residual solvent. The resulting thin film was resuspended in 5% DM (wt vol^{-1}) to a final DMPC concentration of 30 mM, and solubilized in a sonicator bath at 37° C. DM-solubilized Cx46/50 (5–6 mg mL^{-1}) was combined with DMPC at a molar ratio of 0.6:90 (Cx46/50:DMPC) and incubated at 25° C with gentle agitation for 60 minutes. Purified MSP1E1 was then added at a final molar ratio 0.6:1:90 (Cx46/50:MSP1E1:DMPC) and allowed to incubate at 25° C for an additional 20 minutes. Detergent was removed with SM-2

Bio-Beads (BioRad) at a ratio of 30:1 beads:detergent (wt wt^{-1}) by overnight incubation at 25° C with gentle agitation. Bio-Beads were removed by filtration and the sample was ultra-centrifuged at 146,550 x *g* for 15 minutes at 4° C to remove insoluble material. The supernatant was filtered (Millipore; 0.22 μm) and applied to an SEC column (Superose 6 Increase 10/300 GL; GE Healthcare) equilibrated in 20 mM HEPES (pH 7.4) and 150mM NaCl, to separate empty nanodiscs from Cx46/50-embedded nanodiscs. Peak fractions containing both Cx46/50 and MSP1E1, as determined by SDS-PAGE, were collected and concentrated using a centrifugal device (Vivaspin 6; 50-kDa cut-off filter; Sartorius) to a final concentration ~2.5 mg mL^{-1}, as determined by UV absorbance at 280nm (Supplementary Fig. 1a). All chromatography steps were performed by FPLC at 4° C. The presence of both Cx46 and Cx50 in the final sample was confirmed by western blot analysis using polyclonal antibodies directed against the N-terminal domain of Cx46 (AP11570PU-N, Acris) and the N-terminal domain of Cx50 (LS-C116220, LSBio) (Supplementary Fig. 1b).

Negative-stain electron microscopy

Cx46/50-lipid nanodisc complexes were prepared for negative stain EM as described[27]. Briefly, a 3 μl drop of sample (~0.02 mg mL^{-1}) was applied to a glow-discharged continuous carbon coated EM specimen grid (Ted Pella), blotted with filter paper and washed two times with detergent-free SEC buffer. The specimen was then stained with freshly prepared 0.75% (wt vol^{-1}) uranyl formate (SPI-Chem).

Negatively stained specimens were visualized on a 120kV TEM (iCorr, Thermo Fisher Scientific) at 49,000x magnification at the specimen level (Supplementary Fig. 1c). A total of 76 digital micrographs were collected on a 2k x 2k CCD camera (Eagle 2K TEM CCD, Thermo Fisher Scientific) with a calibrated pixel size of 4.37 Å and with nominal defocus values ranging from 1.5–3.0 μm. All negative-stain image processing was performed in EMAN2.2[205,206]. After contrast transfer function (CTF) parameters were determined, micrographs with significant astigmatism or drift were excluded based on visual inspection of Thon rings in the power spectrum. 7,598 hand-picked particles were extracted with 84 x 84 pixel box size and subjected to multiple rounds of reference-free 2D classification, resulting in a final dataset of 3,826 "good" particles. Representative class averages are shown in (Supplementary Fig. 1c), which revealed dimensions consistent with the expectation that Cx46/50 intercellular channels had been reconstituted into a pair of lipid-nanodiscs.

CryoEM specimen preparation and data collection

Samples were prepared for cryoEM by applying 5 μl freshly purified Cx46/50-lipid nanodisc complex (~2.5 mg mL^{-1}) to a glow-discharged holey carbon grid (Quantifoil R 1.2/1.3, 400 mesh) for 10 seconds. The grid was blotted for 4.0 seconds and plunge frozen in liquid ethane using a Vitrobot Mark IV (Thermo Fisher Scientific) at 100% humidity and stored under liquid nitrogen.

CryoEM specimen grids were imaged on a Titan Krios (Thermo Fisher Scientific) operated at 300 kV. Dose-fractionated image stacks were recorded on

a Falcon 3EC Direct Electron Detector (Thermo Fisher Scientific) at 120,000x nominal magnification in counting mode, with a calibrated pixel size of 0.649 Å pixel^{-1} (Supplementary Fig. 2a). The dose rate was 1.14 e^{-} pixel^{-1} sec^{-1}, with 5 frames sec^{-1} collected for a total exposure of 30 seconds, resulting in a total dose for each exposure of ~52.5 e^{-} Å^{-2}. A dataset of 2,087 movies was obtained with nominal defocus values ranging from 1.0–2.2 μm, and data collection parameters were controlled in an automated manner using EPU (Thermo Fisher Scientific).

CryoEM image processing for high-resolution workflow

The full dataset of 2,087 movies were corrected for beam-induced motion in RELION-3.0[207] and contrast transfer function (CTF) estimation was performed with Gctf[208] on the non-dose-weighted, aligned micrographs. Laplacian-of-Gaussian autopicking in RELION-3.0 yielded an initial set of 756,374 picks, which after multiple rounds of 2D classification left 183,784 bona fide particles (binned to a 64-pixel box, 3.894 Å pixel^{-1}). These particles were used to generate a de novo initial model in RELION, and subsequent 3D refinement of these particles yielded a map at 8.0 Å resolution (64 pixel box, 3.894 Å pixel^{-1}). This map was low-pass filtered to 20 Å and projected in 14 unique orientations to perform 3D template-based autopicking in RELION-3.0 to yield 1,210,797 particle picks. Following multiple rounds of 2D classification, this dataset yielded 379,423 “good” particles (200-pixel box, 1.947 Å pixel^{-1}) (Supplementary Fig. 2b). Particles that had been translated within 20 Å of their nearest neighbor were removed to prevent invalidation of gold-

standard Fourier-shell correlation by duplicate particles. Removal of 120,228 duplicates yielded a 259,195 refined particle set.

This particle set was then re-extracted (1.62 Å pix^{-1}, 280-pixel box) and subjected to 3D refinement (D6 symmetry), yielding a map at 3.3 Å resolution. A subsequent round of de-duplication (20 Å cut-off) yielded 227,618 particles that were again re-extracted (0.974 Å pix^{-1}, 512-pixel box) and subjected to 3D-refinement (D6 symmetry), which improved the resolution to 3.2 Å. Two rounds of Bayesian polishing and CTF refinement (per-particle defocus, per-micrograph astigmatism) with subsequent 3D refinement (D6 symmetry) yielded a map at 2.7 Å resolution. Particles were then completely unbinned (400-pixel box, 0.649 Å pix^{-1}) and subjected to another round of 3D refinement (D6 symmetry), yielding a map that reached the same resolution prior to unbinning (2.7 Å). Bayesian polishing and subsequent 3D refinement of these particles showed no significant improvement. The maps generated up to this stage were obtained without applied masks and there was no evidence of resolved lipids within the intracellular leaflet (see Supplementary Fig. 2, Step 2).

At this stage, the newly-developed tools in RELION-3.1-beta[209] were implemented to estimate the degree of beam tilt and high-order aberrations (3-fold and 4-fold astigmatism) present in the particle images. Subsequent 3D refinement (D6 symmetry) improved the resolution to 2.2 Å. Particles that had been translated to within 35 Å of their nearest neighbor (6,224 particles) were again removed to prevent invalidation of the gold-standard Fourier-shell correlation from duplicate particles. The remaining 221,394 particles were subjected to 3D classification into

2 classes with D6 symmetry and a tight solvent mask. Approximately ~89% of the particles (196,320) fell into one class that was subsequently refined to 2.2 Å resolution (D6 symmetry and solvent mask applied). The remaining 11% of particles (26,005) yielded a 2.0 Å resolution map after 3D refinement (D6 symmetry and solvent mask applied). There was no clear difference in protein conformation between these two classes, however, the high-resolution class was characterized by a particle set with comparatively lower defocus values (mean defocus = 1.20 ± 0.29 μm (s.d.)) as compared to the lower resolution class (mean defocus = 1.86 ± 0.52 μm (s.d.)) (https://github.com/huwjenkins). All subsequent processing steps were performed on this high-resolution particle set.

Particles were re-extracted with an expanded box size (initially to 448-pixels) to mitigate delocalized CTF signal from particle images with relatively high defocus. New polishing parameters were obtained by running the Bayesian polishing job type in RELION-3.1-beta in "Training mode" on a random 5,000 particle subset of these refined particles. Bayesian polishing was performed with these new parameters and the subsequent 3D refinement (D6 symmetry and solvent mask applied) improved the resolution slightly to 1.97 Å. This process was iterated multiple times with successive increase in box size and incrementally tighter solvent mask applied during Bayesian polishing until no further improvements were observed, resulting in a final box size of 768 pixels. The final map refined to a global 1.90 Å resolution with D6-symmetry and 2.3 Å resolution without symmetry (Gold-Standard, 0.143 cut-off)[210] (Supplementary Fig. 2c, 3a). The asymmetric reconstruction showed no discernable difference in protein conformation as

compared to the D6-symmeterized map. Local resolution of the final map was estimated in RELION-3.1-beta[68], and local resolution-filtered maps were generated for model building (Supplementary Fig. 2d, 3b). A schematic illustrating this high-resolution cryoEM workflow is presented in (Supplementary Fig. 2c).

CryoEM image processing workflow for lipid classification

For classification and analysis of lipid configurational/conformational heterogeneity, a modified workflow starting from the totally unbinned 227,618 particle set (0.649 Å pix^{-1}, 400-pixel box) which yielded the 2.7 Å resolution map was applied, as described here (and illustrated in Supplementary Fig. 4a). The particle set was subjected to 3D classification (eight classes), with D6 symmetry and a generous solvent mask applied. Two of the eight classes yielded maps in which the lipid configuration was unambiguously resolved: assigned as PC Class 1, containing 9,190 particles (~4% of the data) and PC Class 3, containing 6,944 particles (~3% of the data). Overlapping configurations were resolved in two of the other 3D classes, and so particles from these classes were combined and subjected to a second round of 3D classification with only 2 classes and a tight solvent mask applied. This yielded one class with unresolved lipid configurations, and a second class in which the lipid configuration was unambiguously resolved: assigned PC Class 2, containing 6,075 particles (~3% of the data). Particles assigned to PC Class 1, 2, and 3 were separately subjected to a final round of 3D refinement with a solvent mask and D6 symmetry applied (Supplementary Fig. 4a). The final reconstructions from particles in each of these classes all reached ~2.5 Å

resolution (Gold-Standard, 0.143 cut-off) (Supplementary Fig. 4b). Local resolution was estimated in RELION-3.1-beta, and local resolution-filtered maps were generated for model building (Supplementary Fig. 4c).

We note that alternative approaches to heterogeneity analysis were also pursued. For example, using the signal-subtraction and symmetry expansion methods in attempt to characterize the specimen heterogeneity at the single subunit level[211]. However, these approaches did not resolve any additional PC lipid conformations/configurations than those captured by the approach described above. It also did not help to resolve the Cx46 and Cx50 isoform heterogeneity.

Atomic modelling, refinement, and validation

For all atomic models of Cx46 and Cx50, initial models were derived from previously reported cryoEM structure of amphipol-stabilized Cx46 and Cx50 (PDB 6MHQ and 6MHY[27], respectively). Initial models were fit as rigid bodies into the D6-symmetrized cryoEM maps with applied local resolution-filtering using UCSF Chimera[212]. All atom models for Cx46 and Cx50 were further built into the cryoEM density maps with COOT[213], and subjected to real-space refinement in PHENIX[214] with secondary structure and non-crystallographic symmetry (D6) restraints applied. Several iterations of manual adjustment of the protein model in COOT followed by real-space refinement in PHENIX, were performed while monitoring model quality with MolProbity[215] and quality of side chain fit with EMRinger[216]. Coordinate and restraint files for the dimyristoyl phosphatidylcholine (DMPC) ligands were generated with PHENIX eLBOW[217]. DMPC molecules were manually

fit into the cryoEM density with COOT. Since density for the phosphatidylcholine (PC) head groups was not resolved in the high-resolution ensemble cryoEM map (1.9 Å map), head group and acyl chain atoms that could not be accommodated by the density were deleted. For the PC Lipid Classes 1–3, the postprocessed maps from RELION were low pass-filtered to 3.5 Å resolution to facilitate modeling of the fully-resolved PC lipids. COOT was further used to manually place water molecules into solvent densities of the cryoEM maps. Appropriate placement of waters was determined by the following three criteria: 1) confirmation of at least two hydrogen bond donor/acceptor interactions with the FindHBond tool in UCSF Chimera (< 4 Å donor-acceptor distance) and by visual inspection, 2) confirmation of solvent densities consistently observed in both gold-standard separated half-maps (contoured $\geq 2.5\ \sigma$), and 3) as an additional measure we looked for density overlap between the local resolution-filtered cryoEM map (contoured $\geq\ 5.3\ \sigma$) and the time-averaged water density map generated by equilibrium molecular dynamics simulation (contoured $\geq\ 5.0\ \sigma$) to help assign weak experimental water densities (Supplementary Fig. 8, see calculation of water density maps from MD described in Methods below). However, not all the assigned cryoEM water densities were observed by MD (76% of waters were observed at equivalent positions by cryoEM and MD). Several iterations of real-space refinement on the entire model were completed until refinement statistics converged.

Disclosure of unresolved heteromeric assemblies of Cx46/50

All models of Cx46 and Cx50 were built using D6 (12-fold) symmetrized cryoEM maps. Because native Cx46/50 intercellular channels may form homomeric and/or various patterns of heteromeric/heterotypic configurations[27,39,218], this map most likely represent a heterogeneous mixture of these two isoforms[27]. This approach was chosen because all attempts to separate the heteromeric/heterotypic assembly of these two isoforms using image classification procedures were unsuccessful (presumably due to the close sequence and structural similarity of these two isoforms) (see also[27]). Indeed, Cx46 and Cx50 are 80% identical and 89% similar in sequence over the resolved structural domains, while sites of difference are typically at solvent exposed regions (Supplementary Fig. 6a). Despite this limitation, all atomic-models generated by this approach showed good stereochemical refinement statistics (see Supplementary Table 1), and significant improvements to the previously described amphipol-stabilized models that were refined to 3.4 Å resolution (Supplementary Fig. 5a-e). It is important to note that sites in the density maps where the sequence of Cx46 and Cx50 are identical or similar, both models fit well into the D6 symmetrized map, and these regions tend to display well-resolved sidechain density (Supplementary Fig. 3c,d). Over regions where the sequence of Cx46 and Cx50 differ, sidechain density is sometimes weaker and/or displays appearance of density consistent with a mixture of both isoforms (Supplementary Fig. 3c,d). These observations are possibly due to the imposed D6 symmetry averaging of density belonging to two different sidechains in these areas, or relative flexibility at these sites as many of these residues are

also solvent-exposed. In these areas of difference, where EM density is observed, both Cx46 and Cx50 can be fit into the density equally well (Supplementary Fig. 3c,d). Nevertheless, caution should be used with interpretation of the conformational details at these sites of isoform difference.

Molecular dynamics simulations

Visual Molecular Dynamics (VMD) v1.9.3[219] was used to build systems for sheep Cx46 and Cx50 in a dual lipid-bilayer with varying salt conditions, designed to mimic either the cellular environment (cytoplasmic KCl, extracellular NaCl) or experimental cryoEM conditions (uniform NaCl). To produce unbiased analysis of water and lipid interactions, all water and lipid molecules derived by cryoEM analysis were removed from the Cx46 and Cx50 models prior to the MD setup. Each system comprised the full dodecameric gap junction intercellular channel, prepared in explicit water (model TIP3P) and embedded in two lipid bilayers composed of dimyristoyl phosphatidylcholine (DMPC), mimicking the cell-to-cell junction. For all models, sidechains were protonated according to neutral conditions and the HSD model was used for all histidine residues. Disulfide bonds identified in the experimental structures were enforced. Amino acids corresponding to the intracellular loop (ICL; residues 110–136 in sheep Cx46 and residues 110–148 in sheep Cx50) and c-terminal domain (CTD; residues 225–413 in sheep Cx46 and residues 237–440 in sheep Cx50) were not included for the MD simulations, as experimental data describing the structure of these large flexible domains (~30 residue ICL and ~200 residue CTD in Cx46 and Cx50) are missing.

The introduced n- and c-terminal residues resulting from the missing ICL segment (sheep Cx46 R109 and K137; sheep Cx50 R109 and R149) were neutralized. All of the systems were modified with an n-terminal acetylation (at the starting residue Gly 2) in VMD through an all-atom acetylation patch in the automated PSF-Builder, in accordance with previously described proteomics analysis on native Cx46/50[27,49,50], and expectation that this species would predominate in cells[220]. A complete list of modeled residues for each system is provided in Supplementary Fig. 7a.

The prepared protein structures were submerged in a hydration shell using Solvate 1.0.1[221]. Water was removed from sections of the channel corresponding to transmembrane domains, based on hydrophobic character and localization of lipid-nanodisc observed in the experimental cryoEM data (+/- 20–50 Å from the center of the channel). The CHARMM-GUI membrane-builder[222] was used to build the DMPC bilayers (pre-melted), with dimensions of 154 x 154 Å for Cx46 and Cx50, and lipids overlapping with protein were removed. The entire system was then placed in a water box with dimensions 147 x 147 x 174 Å for both Cx46 and Cx50, using VMD's Solvate plugin. The system was neutralized using the Autoionize plugin, then 150 mM KCl and 150 mM NaCl was added to the solvent areas corresponding to intracellular and extracellular regions of the simulation box for the "KCl" systems, while the "NaCl" systems contained 150 mM NaCl for the entire box. A summary of atoms counts for each system is provided in Supplementary Fig. 7a.

CUDA-accelerated nanoscale molecular dynamics (NAMD) 2.13[223] was used for all classical MD simulations, using the CHARMM36 force-field[224] for all atoms and TIP3P explicit model for water. Each system was prepared following the same minimization and equilibration protocol, as follows. An initial minimization step, where the lipids, solvent and ions were allowed to minimize around the protein was performed, with the protein harmonically constrained for 1 ns, with 1 fs timestep and constant pressure (NPT ensemble). A second minimization step was applied, where the system was free to minimize with a harmonic constraint on the protein backbone to ensure stable quaternary structure for 1 ns – lipids relax and compress during minimization steps with minimized dimensions equal to the water box (14.7 x 14.7). The entire system was then released from restraints and subjected to all-atom equilibration runs employing Langevin thermostat, with a constant temperature of 310 K and constant pressure of 1 atm (NPT ensemble), with 2 fs time-steps and allowed to proceed for 30 ns. Periodic boundary conditions were used to allow for the smoothed particle mesh Ewald (PME) calculation of electrostatics. Finally, two independent 100 ns production runs were seeded with randomly initialized velocities from the initial equilibration simulation – providing 200ns of production for each system. Root mean squared deviations (r.m.s.d.) and root mean squared fluctuations (r.m.s.f.) were calculated using VMD, and r.m.s.f. values were displayed to the protein structure using UCSF Chimera (Supplementary Fig. 7b-d). All systems approached a steady r.m.s.d. within 30 ns of the equilibration phase (Supplementary Fig. 7b), and r.m.s.f. values appeared well-behaved over the production periods, including regions corresponding to the

NTH domain[27] (Supplementary Fig. 7c,d). The only significant fluctuations (i.e., > 2.5 Å) occurred at the TM2, TM3 and TM4 cytoplasmic termini, which is expected as these regions form the boundary to the intrinsically disordered ICL and CTD regions of the protein (not modeled). All systems maintained an electro-chemical seal to extracellular sodium ions (Na^+) around the ECD docking domains during MD simulation.

Calculation of MD-based density maps

The Volmap plugin in VMD was used for the calculation of volumetric density maps, by replacing each atom with a normalized gaussian distribution, whose standard deviation is equal to the radius of the atom. The gaussians are summed and distributed on a grid for each frame of the simulation. The grids were re-sampled to a final voxel resolution of 0.649 Å to match the pixel size used in the cryoEM reconstruction. Water, ion, and lipid maps were calculated from each of two 100 ns production runs, and subsequently averaged and symmetrized (D6-symmetry) with the relion_image_handler tool in RELION-3.0[207]. Lipid and water density maps produced from Cx46 and Cx50 MD simulations contained significant overlap to each other and to the cryoEM maps, however, the maps produced from Cx50 MD simulations were of higher quality and were selected for detailed comparative analysis to the cryoEM density maps (Fig. 3 and Supplementary Fig. 8). Ion density maps showed only a few features and did not correspond to densities observed by cryoEM and were therefore excluded from further analysis.

Area per lipid and lipid order parameter calculations

Area per lipid (APL) for each membrane, separated by intracellular and extracellular leaflet, were calculated using the program FATSLiM[225], and used as an indicator of equilibration of the lipid systems (Supplementary Fig. 9a).

Eq.1 $$S_{CD} \equiv -\langle \frac{3\cos^2(\theta_{CD})-1}{2} \rangle$$

The S_{CD} lipid order parameter, as defined by Eq. 1, measures the orientation of the SN1 and SN2 acyl-chains by monitoring the angle that each acyl C-H vector makes with the bilayer normal θ_{CD}. The calculations of S_{CD} were done using the VMD script *calc_op.tcl*[226]. To analyze the distance dependence of S_{CD} in the respective membrane leaflets, the averaged S_{CD} values were calculated in 5 Å concentric shells around the protein (SN1 and SN2 calculated separately). S_{CD} of lipids from both membranes are averaged together, while the intra- and extracellular leaflets were averaged separately (Supplementary Fig. 9b-e). To visualize the order parameter mapped to the structure, the time-averaged S_{CD} values were calculated for each lipid (SN1 and SN2 combined values for acyl carbons 4–11), and colored according to this value using UCSF Chimera (Fig. 3c).

MD lipid configuration analysis

Analysis of PC lipid configuration (*i.e.,* acyl-chain positioning) was performed using in-house scripts to assess how phospholipids are organized within the extracellular leaflet of the Cx46 and Cx50 intercellular channels during MD simulation, as

compared to the PC configurations classified by cryoEM. This was done by counting the instances of a single DMPC molecule occupying the region bounded by the MD-based lipid-density, contoured at $\sigma_{\min} = 8$ (Fig. 3a). The lipid acyl-chain density maps calculated from the Cx50 MD simulations reveal more than 19 resolved rods (i) of density per connexin subunit (12 subunits), and each rod was arbitrarily numbered 1 through 19 (total of 228 acyl-chain positions). A lipid was classified in a state when both acyl-chains occupied a density, $\text{state} \equiv \text{"i} - \text{j"}\ (\text{where i} \neq \text{j})$. A rod density is considered occupied if at least 5 carbons of a lipid's acyl-chain are within the density, such that $\sigma_{\text{carbon}} \geq \sigma_{\min}$. This classification scheme was applied to every lipid within 15 Å of the protein, over each frame (0.1 ns per frame). To analyze the dynamics of lipids surrounding the protein, the state of each lipid (e.g., "1–2", "1–5", "none", etc.) was monitored and recorded at every frame providing a time series of lipid configurational dynamics in state-space (Fig. 4d).

Statistical analysis

95% confidence intervals for Cα r.m.s.f. values are reported (n = 24) using a two-tailed student t-test. Fourier-Shell Correlation (FSC) was performed using Gold-Standard methods with a 0.143 cut-off criteria[210]. No statistical methods were used to predetermine sample size for the cryoEM dataset. The experiments were not randomized, and investigators were not blinded to allocation during experiments and outcome assessment.

Figures and movie preparation

Figure panels and movies were created using Chimera[227], ChimeraX[212], VMD[219], and Blender[228]. Figures were composited in Adobe Photoshop. Movies were composited in Blender.

Data Availability

CryoEM maps, including half-maps, pre- and post-processed maps and masks, have been deposited to the Electron Microscopy Data Bank (EMD-22358, EMD-22382, EMD-22390, EMD-22391). Coordinates for Cx50 and Cx46 atomic models have been deposited to the Protein Data Bank (PDB ID: 7JJP and 7JKC correspond to the high-resolution models, 7JLW and 7JMD correspond to the models from PC Class 1; 7JM9 and 7JN0 correspond to PC Class 2; and 7JMC and 7JN1 correspond to PC Class 3). The original multi-frame micrographs have been deposited to EMPIAR (EMPIAR-10480). MD trajectory files and MD-based density maps have been deposited to Zenodo (doi: 10.5281/zenodo.3951861).

Code Availability

In-house code developed for the analysis of MD trajectories to assess lipid configurational state dynamics have been deposited on the Reichow Lab GitHub repository (https://github.com/reichow-lab/Flores-Haddad-Dolan_et-al.NatCommun2020) and Zenodo (doi: 10.5281/zenodo.3955131).

Acknowledgements

We thank Dror Chorev and Carol V. Robinson for help analyzing specimens prepared for cryoEM. We are grateful to the staff at the OHSU Multiscale Microscopy Core and Advanced Computing center, and to the Pacific Northwest Center for CryoEM (supported by NIH Grant **U24GM129547**) **and accessed through EMSL (grid.436923.9). J.A.F. and B.G.H. are supported by the National Institutes of Health NRSA fellowships (F31-EY030409) and (F31-EY031580), respectively. K.A.D. is supported by National Institutes of Health BUILD EXITO Program (TL4-GM118965) and Berkeley Molecular Biophysics Training Grant (T32-GM008295).** C.C.Y. is supported by OHSU. **J.C. and** D.M.Z. are supported by the OHSU Center for Spatial Systems Biomedicine, by the National Science Foundation (MCB 1715823) and by the National Institutes of Health (R01-GM115805). S.L.R. is supported by the National Institutes of Health (R35-GM124779).

Appendix

Supplementary Table 1

	Cx46	Cx50	Cx46 *PC Class 1*	Cx50 *PC Class 1*	Cx46 *PC Class 2*	Cx50 *PC Class 2*	Cx46 *PC Class 3*
Data collection and processing							
Magnification	120,000	120,000	120,000	120,000	120,000	120,000	120,000
Voltage (kV)	300	300	300	300	300	300	300
Electron exposure (e–/Å^2)	52.5	52.5	52.5	52.5	52.5	52.5	52.5
Defocus range (μm)	-1.0 to -2.2	-1.0 to -2.2	-1.0 to -2.2	-1.0 to -2.2	-1.0 to -2.2	-1.0 to -2.2	-1.0 to -2.2
Pixel size (Å)	0.649	0.649	0.649	0.649	0.649	0.649	0.649
Symmetry imposed	D6	D6	D6	D6	D6	D6	D6
Initial particle images (no.)	1,210,797	1,210,797	1,210,797	1,210,797	1,210,797	1,210,797	1,210,797
Final particle images (no.)	26,005	26,005	6,073	6,073	9,188	9,188	6,942
Map resolution (Å)	1.90	1.90	2.52	2.52	2.47	2.47	2.45
FSC threshold	0.143	0.143	0.143	0.143	0.143	0.143	0.143
Map resolution range (Å)	1.90–3.30	1.90–3.30	2.42–4.56	2.42–4.56	2.33–4.14	2.33–4.14	2.47–4.33
Refinement							
Initial model used (PDB code)	6MHQ	6MHY	6MHQ	6MHY	6MHQ	6MHY	6MHQ
Model resolution (Å)	1.99	1.99	2.55	2.52	2.35	2.35	2.63
FSC threshold	0.5	0.5	0.5	0.5	0.5	0.5	0.5
Model resolution range (Å)	-	-	-	-	-	-	-
Map sharpening *B* factor (Å^2)	-25.00	-25.00	-40.49	-40.49	-45.42	-45.42	-43.73
Model composition							
Non-hydrogen atoms	21,876	21,804	22,308	22,176	21,624	21,552	21,312
Protein residues	2352	2352	2,328	2,328	2,316	2,316	2,304
Ligands	180	180	168	168	132	132	144
B factors (Å^2)							
Protein	40.46	37.12	51.09	50.04	41.92	47.13	59.04
Ligand	42.58	38.21	55.25	55.19	43.92	47.64	61.77
R.m.s. deviations							
Bond lengths (Å)	0.011	0.010	0.010	0.007	0.009	0.009	0.007
Bond angles (°)	0.824	0.835	0.825	0.821	0.934	1.073	0.816
Validation							
MolProbity score	0.80	1.03	1.03	1.03	1.13	1.22	0.98
Clashscore	0.91	2.49	2.45	2.46	2.90	3.93	2.07
Poor rotamers (%)	0.57	0.56	0.00	0.56	1.17	1.14	0.00
Ramachandran plot							
Favored (%)	97.92	98.44	98.11	98.95	98.41	98.94	98.40
Allowed (%)	2.08	1.56	1.89	1.05	1.59	1.06	1.60
Disallowed (%)	0.00	0.00	0.00	0.00	0.00	0.00	0.00

Supplementary Table 1. CryoEM Statistics.

Summary of cryoEM data collection, refinement, and model validation. The ensemble cryoEM dataset was used to obtain the 1.90 Å resolution reconstruction and atomic models for Cx46 and Cx50, including 396 water molecules and 150 lipid acyl-chains. 3D classification was used to obtain the three PC classes and associated atomic models for Cx46 and Cx50 (PC Class 1–3). Pre-processed and post-processed maps and associated masks from all datasets have been deposited to the EM databank (EMD-22358, EMD-22382, EMD-22390, EMD-22391). The original multi-frame micrographs have been deposited to EMPIAR (EMPIAR-10480). Coordinates for Cx50 and Cx46 atomic models have been deposited to the Protein Data Bank (7JJP and 7JKC correspond to the high-resolution models, 7JLW and 7JMD correspond to the ~2.5 Å models from PC Class 1; 7JM9 and 7JN0 correspond to PC Class 2; and 7JMC and 7JN1 correspond to PC Class 3).

Supplementary Figure 1

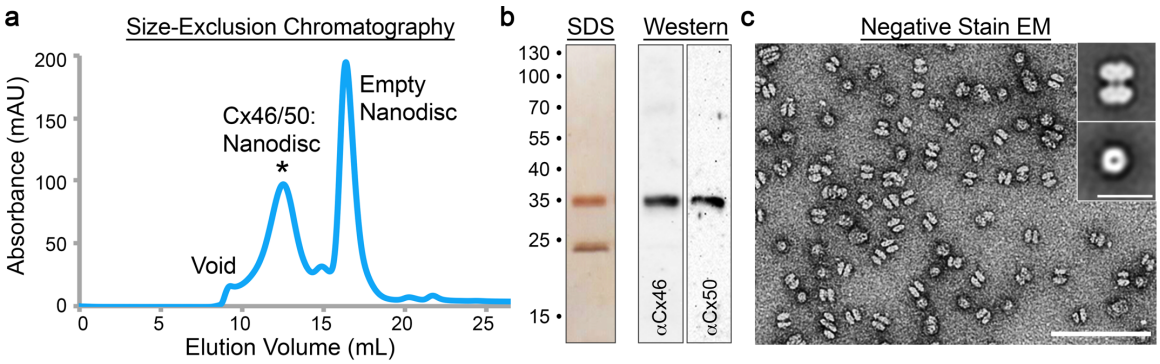

Supplementary Figure 1. Cx46/50 reconstitution into MSP1E1/DMPC lipid-nanodiscs and negative stain EM.

a) Size-exclusion chromatography (SEC) trace monitored by UV absorbance at 280 nm. Peaks corresponding to Cx46/50 reconstituted into MSP1E1/DMPC nanodiscs (asterisk), empty nanodisc and void are indicated. **b)** SDS-PAGE (left) and western blot (right) of peak SEC fraction (labeled asterisk), with molecular weight markers indicated. MSP1E1 migrates as a ~24 kDa band (predicted MW ~27.5 kDa). Cx46 and Cx50 migrate together at ~38 kDa band, as expected from c-terminal truncation from core lens fiber cells[27] and confirmed by western blot (right). **c)** Electron micrograph of negatively stained particles from SEC fraction (labeled asterisk), with scale bar = 100 nm. *Inset*, shows representative 2D class averages of sideview (top) and top view (bottom), with scale bar = 20 nm. Particles display dumbbell-like structures corresponding to Cx46/50 gap junctions intercellular channels[27,229], embedded into a pair of ~10-11 nm wide nanodiscs (MSP1E1 nanodiscs have a predicted diameter of ~10.5 nm[3]).

Supplementary Figure 2

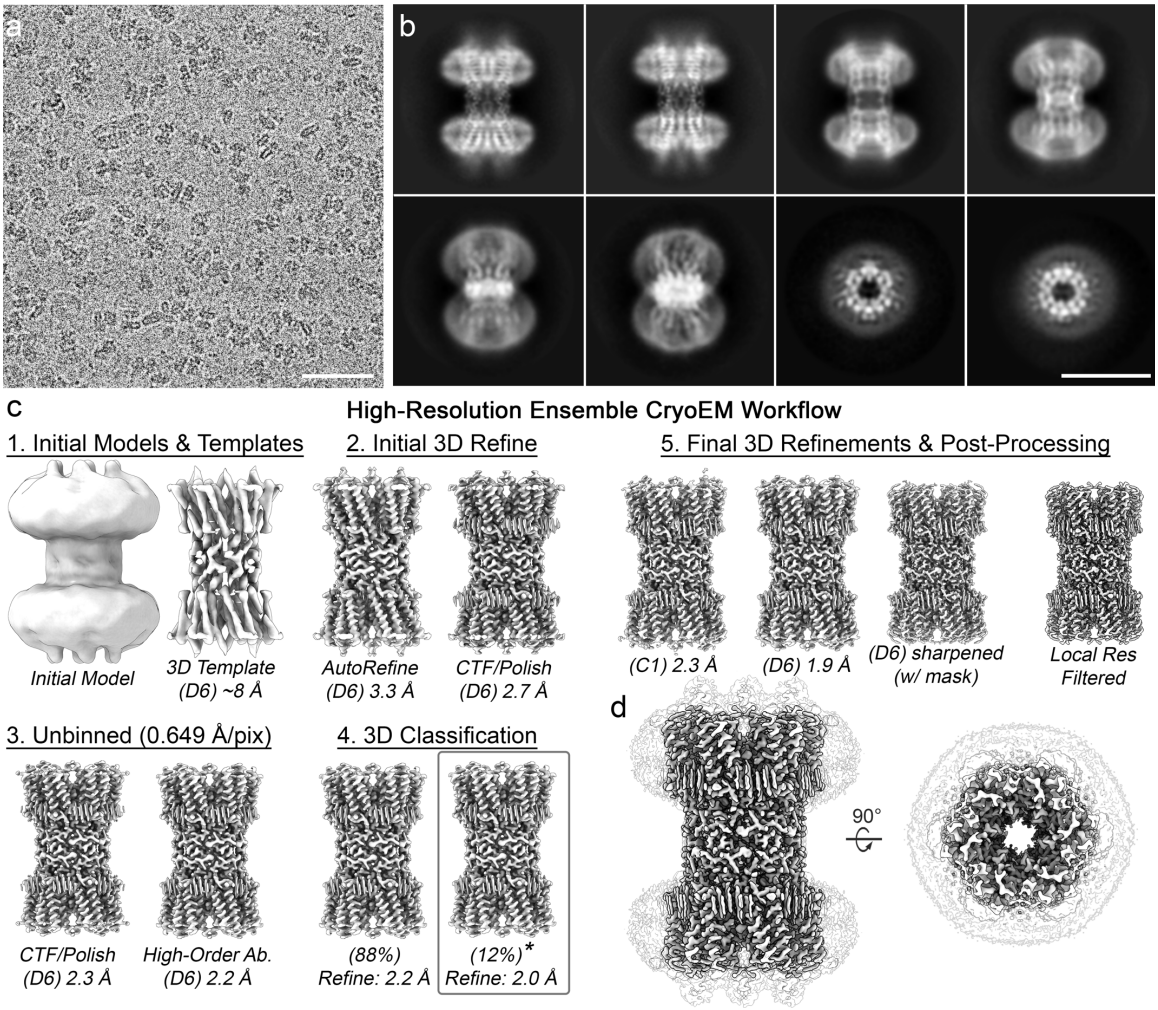

Supplementary Figure 2. CryoEM image processing workflow for 1.9 Å ensemble reconstruction of Cx46/50 in DMPC lipid nanodiscs.

a) Representative cryoEM micrograph (dataset of 2088 movies) recorded on a Falcon III detector, with physical pixel size = 0.649 Å^2 and total dose of ~60 e$^-$ per Å^2. Scale bar = 50 nm. **b)** Representative 2D class averages. Scale bar = 10 nm**. c)** Image processing and 3D reconstruction workflow carried out in RELION[207,209], with representative maps at different stages of the image processing pipeline. Step 1) De-novo model generated in Relion (left) and initial 3D AutoRefinement with D6-symmetry (~8 Å resolution, 3.9 Å pixel size) (right), which was then filtered to 20 Å and used for 3D template auto-picking in Relion (resulting in ~1.2M particle picks, which were culled to ~228k "good" particles following multiple rounds of 2D classification and de-duplication). Step 2) Resulting 3D AutoRefine with D6-symmetry without masking (3.2 Å resolution, 0.97 Å pixel size) (left), and resulting map following per particle CTF-refinement and polishing in Relion (2.7 Å) (right). Step 3) Particles were unbinned (pixel size 0.649 Å/pix, box size = 400 pix)

and refined with per-particle CTF-correction and polishing (2.3 Å) (left), and further refinement of high-order aberration parameters in Relion v3.1-beta[4] (2.2 Å) (right). Step 4) Particles were de-duplicated, resulting in a set of ~221k particles, and subjected to 3D classification (two classes). Class 1 contained 88% of the particles and was further refined to 2.2 Å resolution (left). Class 2 contained 12% of the particles and was further refined to 2.0 Å resolution (right, asterisk). It is noted that the major differences between these two classes appears to be the distribution of particle defocus values, were the higher resolution class contains particles with lower defocus range (mean defocus = 1.20 ± 0.29 μm (s.d.)). Step 5) Particles belonging to Class 2 (~26k particles), were then subjected to multiple rounds of 3D Auto-refinement followed by per-particle CTF, aberration-correction and polishing, using successively larger box-sizes until no further improvement, resulting in a final reconstruction at 2.3 Å resolution (C1 symmetry) (left) and 1.9 Å resolution (D6 symmetry) (center, left). There were no clear conformational differences between the C1 and D6-symmetrized reconstructions. The D6-symmeterized map was then subjected to post-processing (b-factor sharpening) (center, right) and local-resolution filtering in Relion (right) for downstream analysis. **d)** Final reconstruction of Cx46/50 following local resolution filtering, used for atomic-modeling. Transparent silhouette displays the unmasked map at low-contour to illustrate the dimensions of the lipid nanodisc densities.

Supplementary Figure 3

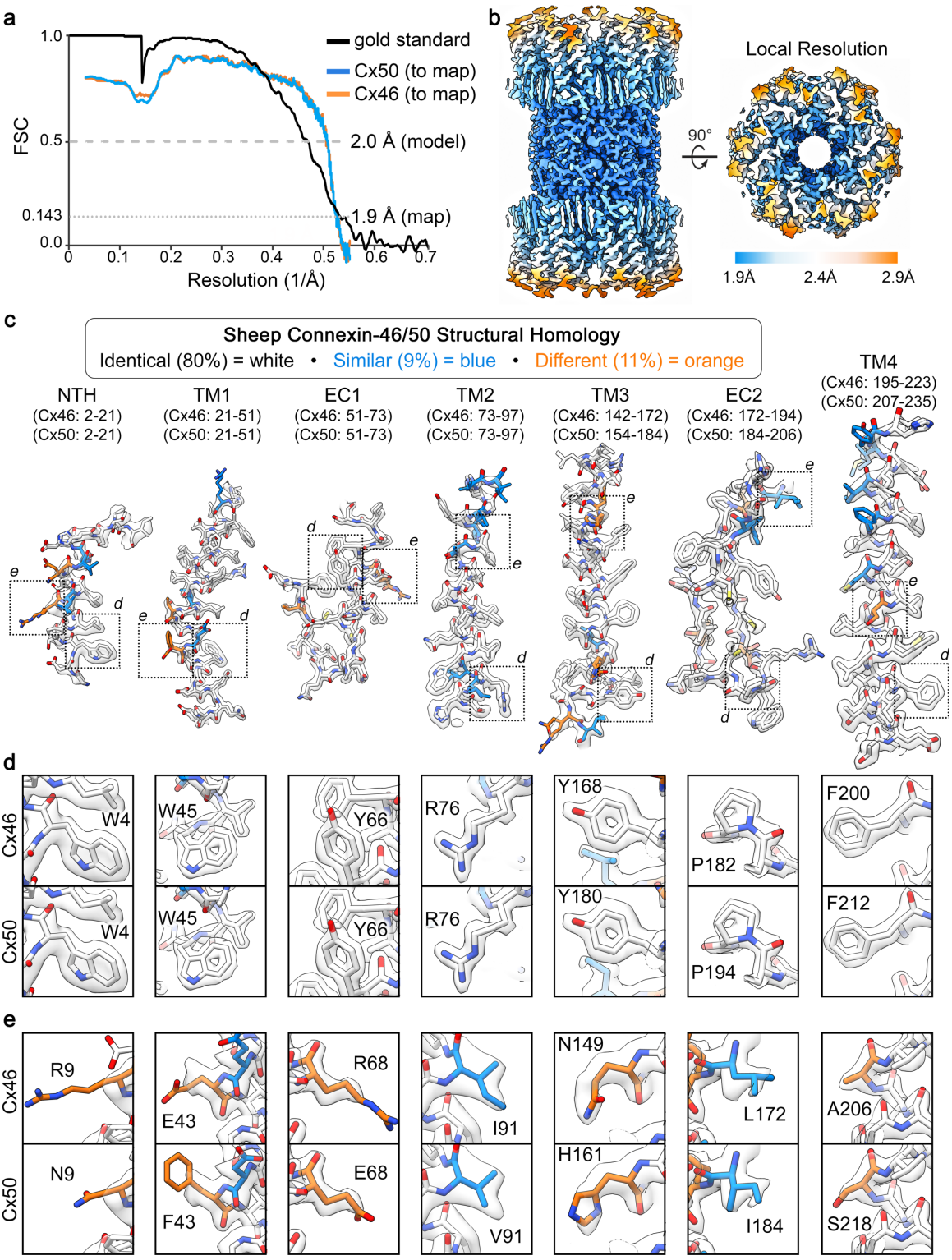

Supplementary Figure 3. Global and local resolution assessment of the 1.9 Å ensemble reconstruction of Cx46/50 in DMPC lipid nanodiscs.

a) Fourier Shell Correlation (FSC) analysis obtained from the ensemble cryoEM map of Cx46/50 in DMPC lipid nanodiscs. Gold-standard FSC (black) of the final refined cryoEM map indicates a global resolution of 1.9 Å (0.143 cut-off). FSC curves comparing atomic models for Cx50 (blue) and Cx46 (orange) fit to the final cryoEM map display overall correlation at 2.0 Å (0.5 cut-off). **b)** Local resolution analysis of the final cryoEM map using RELION[207], displayed by colored surface (1.9 – 2.4 Å = blue – white; 2.4 – 2.9 Å = white – orange). **c)** Segmented cryoEM map with regions of the atomic models for sheep Connexin-46 (Cx46) and Connexin-50 (Cx50) fit to the local-resolution filtered map. Residue numbering for Cx46 and Cx50 is displayed above the corresponding segments for the n-terminal helix domain (NTH) domain, the transmembrane domains 1-4 (TM1-4) and extracellular domains 1-2 (EC1-2), Residues are colored according to the pair-wise sequence homology between sheep Cx46 and Cx50, as being identical (white, 80%), similar (blue, 9%) and different (orange, 11%), with all heteroatoms colored by standard scheme (oxygen – red; nitrogen – blue, sulfur – yellow). **d, e)** Windows show zoom-views corresponding to boxed regions of the segmented maps. **d)** Displays fits over representative regions where both Cx46/50 contain identical amino acids, where the high-resolution features are well-resolved. **e)** Displays fits over representative regions where the sequence of Cx46 and Cx50 differ, and where sidechain density is weaker and/or consistent with heterogeneity. This is presumably due to the heteromeric/heterotypic mixture of these isoforms[27,39,218] and the imposed averaging of two different sidechains in these areas, and/or to relative flexibility at these sites, as many of these same residues correspond to solvent/lipid exposed sidechains (e.g., R9/N9; E43/F43, R68/E68, I91/V91 and A206/S218).

Supplementary Figure 4

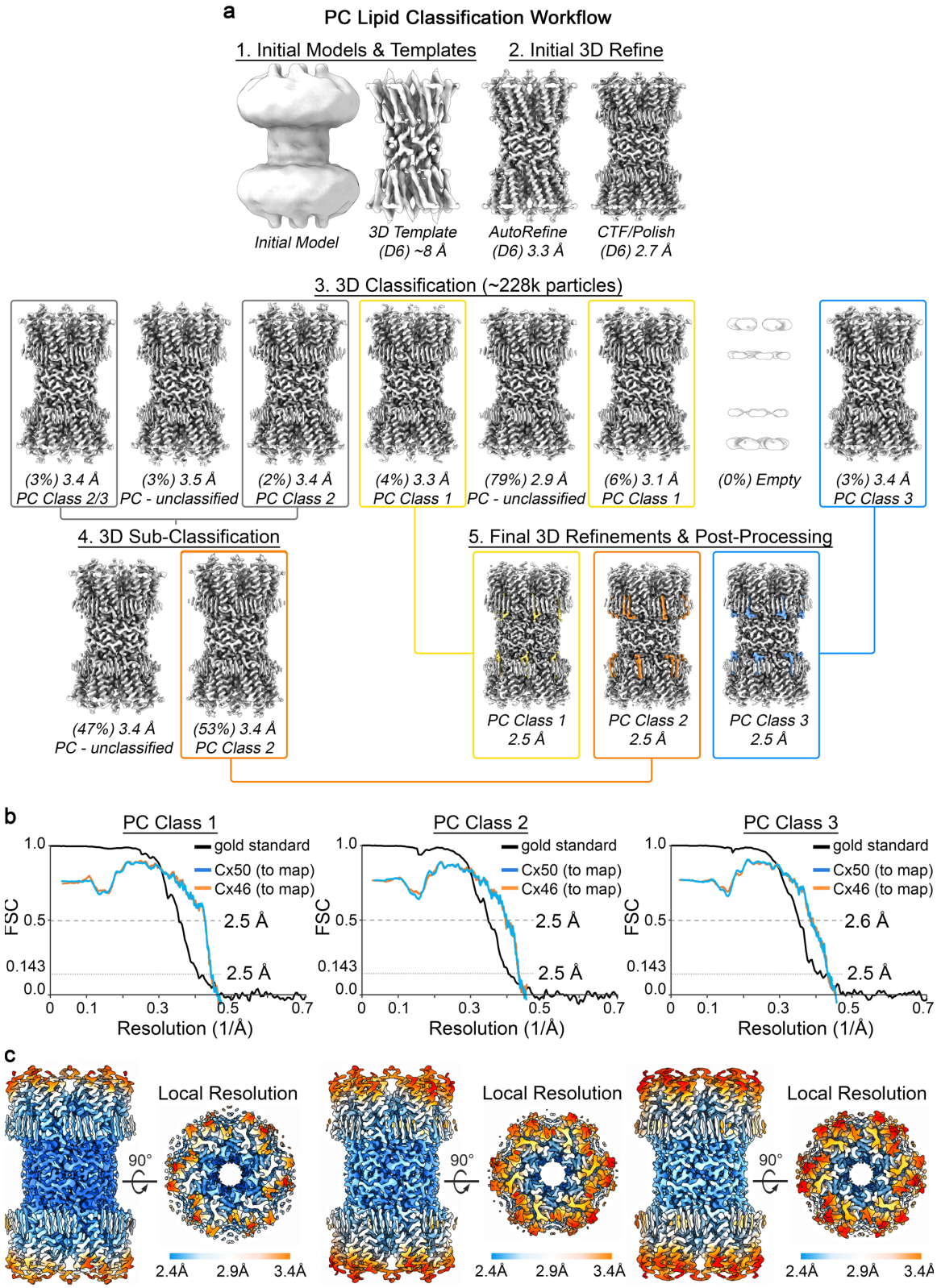

Supplementary Figure 4. Image processing and resolution assessment for 3D lipid-classification workflow.

a) Image process and 3D reconstruction workflow carried out in RELION for the analysis of PC lipid configuration/conformational heterogeneity, with representative maps at different stages of the image processing pipeline. Steps 1 and 2) are the same as described in Supplementary Fig. 2, which resulted in a 2.7 Å reconstruction from a dataset of ~228k "good" particles (right). Step 3) These particles were unbinned and re-extracted (0.649 Å/pix, 400 pixel box), and subjected to 3D classification (eight classes) without image alignment. Two of the eight classes yielded maps in which the lipid configuration was unambiguously resolved: assigned as PC Class 1 (yellow box), containing 9,190 particles (~4% of the data) and PC Class 3 (blue box), containing 6,944 particles (~3% of the data). Overlapping configurations were resolved in two of the other 3D classes (grey boxes). Step 4) The particles from these overlapping classes (grey boxes) were combined and subjected to a second round of 3D classification with two classes. This yielded one in which the lipid configuration was unambiguously resolved: assigned PC Class 2 (orange box), containing 6,075 particles (~3% of the data). Step 5) Particles assigned to PC Class 1 (left), PC Class 2 (center) and PC Class 3 (right) were separately subjected to a final round of 3D refinement and per-particle polishing, with D6 symmetry applied, resulting in final reconstructions ~2.5 Å resolution (Gold-Standard, 0.143 cut-off). **b)** Fourier Shell Correlation (FSC) analysis obtained for PC Class 1 (left), PC Class 2 (center) and PC Class 3 (right). Gold-standard FSC (black) of the final refined, masked and post-processed cryoEM map indicates a global resolution of 2.5 Å (0.143 cut-off). FSC curves comparing atomic models for Cx50 (blue) and Cx46 (orange) fit to the final cryoEM maps display overall correlation at 2.5–2.6 Å (0.5 cut-off). **c)** Local resolution analysis of the final cryoEM maps for PC Class 1 (left), PC Class 2 (center) and PC Class 3 (right) using Relion, displayed by colored surface (2.4 – 2.9 Å = blue – white; 2.9 – 3.4 Å = white – orange).

Supplementary Figure 5

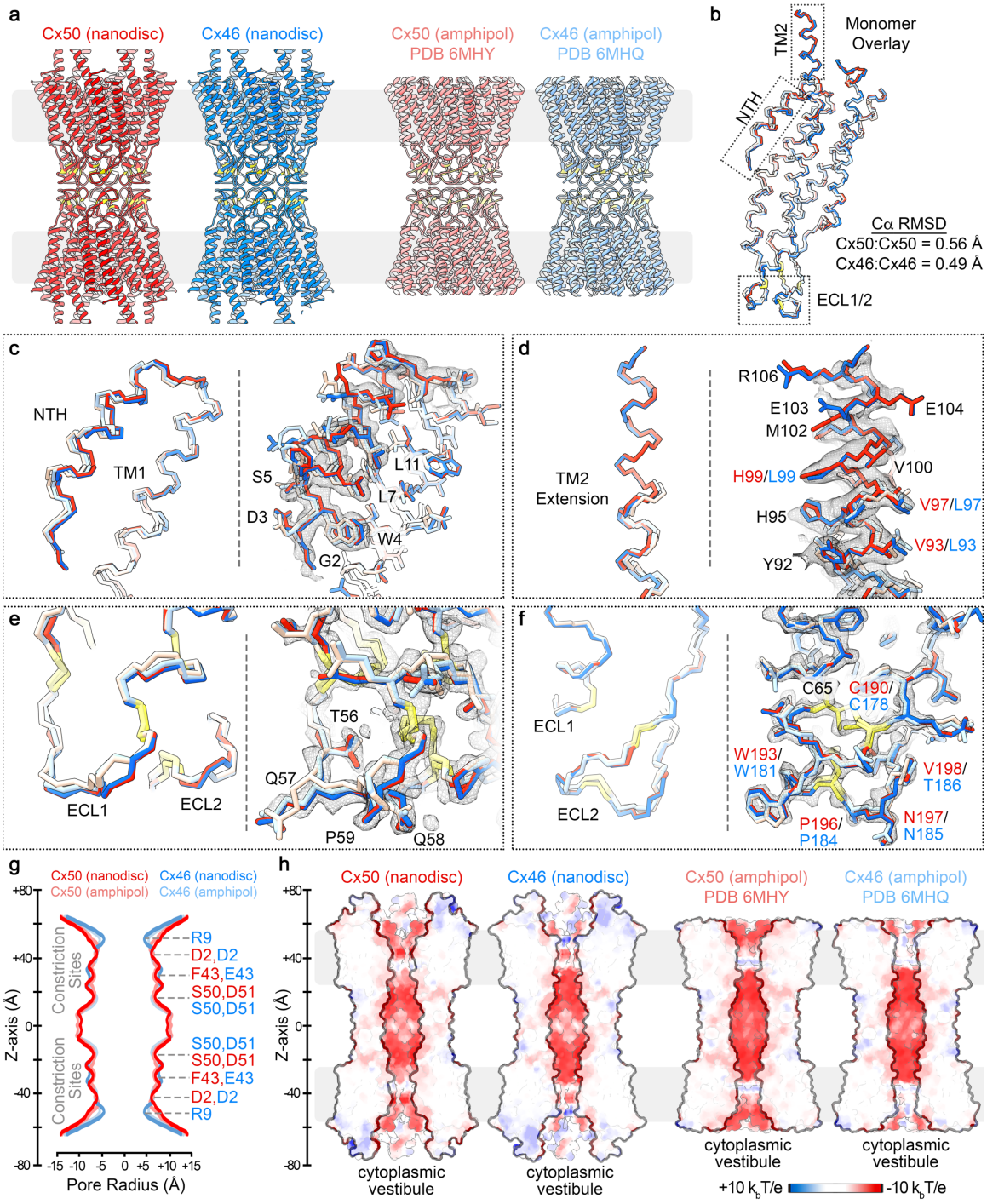

Supplementary Figure 5. Comparison of Cx46/50 structures determined in amphipol and lipid-nanodiscs.

a) Ribbon structures of Cx50 (red) and Cx46 (blue) determined by cryoEM in lipid-nanodisc (left) and as previously determined in amphipol (right) with Cx50 (light red, PDB 6MHY) and Cx46 (light

blue, PDB 6MHQ). Regions of lipid bilayer are indicated by light grey box. Conserved cysteine positions within the EC1/2 domains, involved in disulfide formation, are indicated in yellow. **b)** Cα traces over-laid for these four models, corresponding to a single subunit following super-positing (colored as in panel a). Cα r.m.s.d. following super-positioning is indicated for Cx50 (nanodisc) vs. Cx50 (amphipol) = 0.56 Å, and Cx46 (nanodisc) vs. Cx46 (amphipol) = 0.49 Å. **c–f)** Shows zoom views corresponding to the boxed regions in panel b. For each panel, (left) shows Cα trace and (right) shows all atom fit into the 1.9 Å cryoEM density map obtained from the nanodisc embedded structure, to show regions of improved fit to the experimental density map. Highlighted residues are indicated, and labels colored according to identity between the Cx50 and Cx46 isoforms (black – identical, red – Cx50 and blue – Cx46). **g)** Pore radius determined using HOLE[230], for experimental structures of Cx50-nanodisc (red), Cx46-nanodisc (blue), Cx50-amphipol (light red) and Cx46-amphipol (light blue). Locations corresponding to constriction sites are indicated, and residues contributing to these sites of constriction for both isoforms are labeled (Cx50 – red; Cx46 – blue). **h)** Cut-away surface representation of Cx50-nanodisc (left), Cx46-nanodisc (left center) and Cx50-amphipol (right center) and Cx46-amphipol (right), colored by coulombic potential (negative – red, neutral – white and positive – blue). This comparison illustrates the electrostatic environment of the permeation pathways and the extension of the intracellular vestibule that is resolved in the Cx46/50-nanodisc models, as compared to the previously described Cx46/50-amphipol models.

Supplementary Figure 6

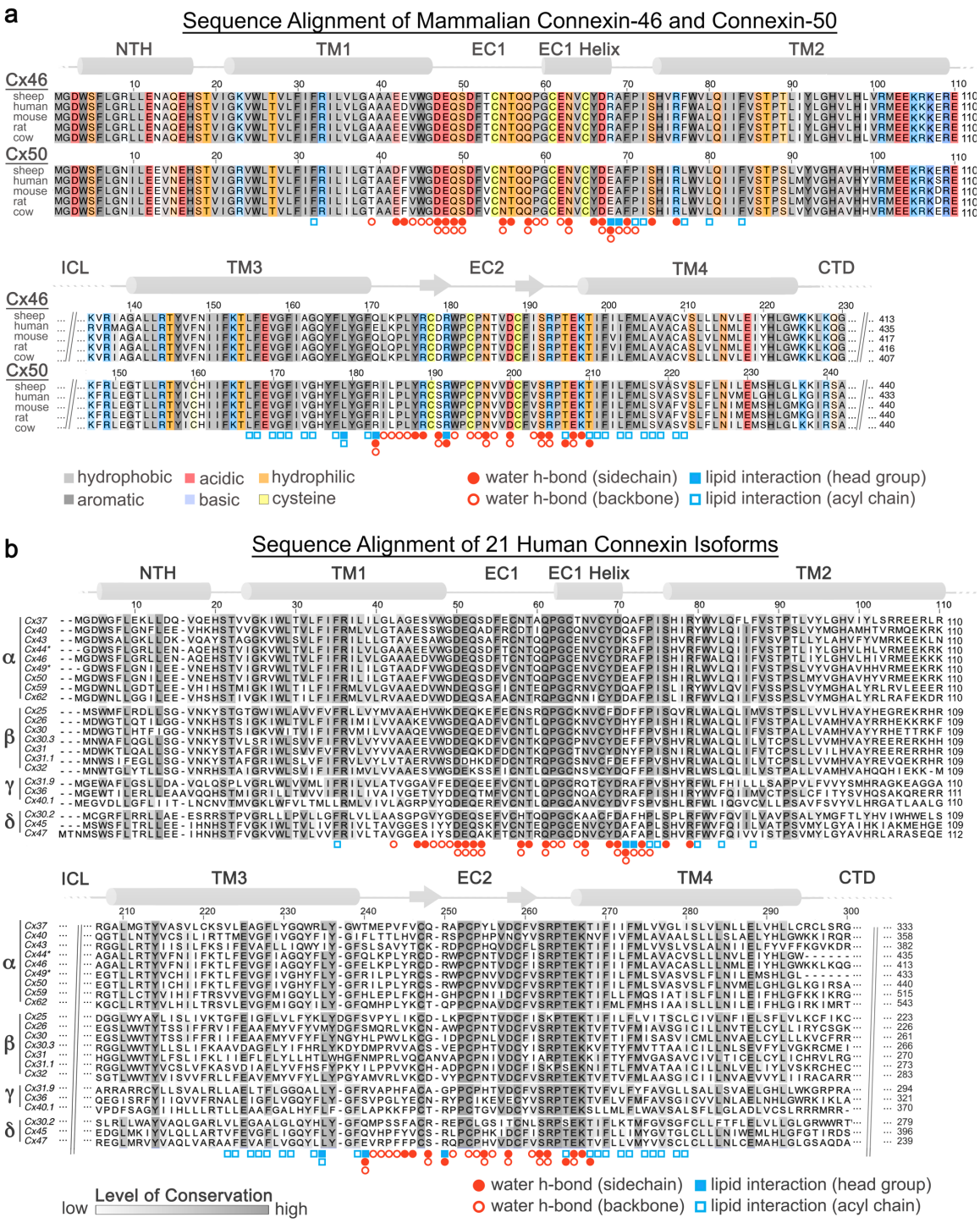

Supplementary Figure 6. Sequence alignment with annotated lipid and water binding sites.

a) Multiple sequence alignment of mammalian Cx46 and Cx50 isoforms with residues contributing to lipid and/or water binding sites annotated (filled circle – water h-bonding with amino acid

sidechain; open circle – water h-bonding with amino acid backbone) and (filled square – interaction involving lipid headgroup; open square – interaction involving lipid acyl chain). Primary sequence coloring corresponds to amino acid type (grey – hydrophobic; dark grey – aromatic; red – acidic; blue – basic; orange – hydrophilic; yellow – cysteine). Regions of sequence homology are indicated by the level of shading. Secondary structure and domain labels are indicated for the n-terminal helix (NTH), transmembrane helices (TM1-4) and extracellular domains (EC1-2). Regions lacking defined structure and of poor sequence homology within the intracellular loop (ICL) and c-terminal domain (CTD) have been omitted for clarity. Sheep and human Cx46 and Cx50 orthologs contain ~95% sequence identity (~98% similarity) over the structured regions of the protein. Numbering corresponds to the amino acid sequence of sheep Cx44 and Cx49 used in the main text. **b)** Multiple sequence alignment of 20 human connexin isoforms, with sheep Cx44 (Cx46 homolog) and Cx49 (Cx50 homolog) included for comparison. Isoforms are categorized by connexin family α, β, γ, and δ. The orphan Cx23 was excluded from analysis. Regions of sequence homology are indicated by the level grey of shading. Annotations for lipid and water binding sites and secondary structural elements/domains are indicated as in panel a.

Supplementary Figure 7

a

	Connexin-50 (KCl)	Connexin-50 (NaCl)	Connexin-46 (KCl)	Connexin-46 (NaCl)
Total Atoms	356,838	356,838	357,545	357,545
Solvent	186,150	186,150	186,663	186,663
Lipids	131,806	131,806	131,806	131,806
Protein	38,484	38,484	38,712	38,712
Ions	398	398	364	364
Modelled Residues	2-109 ; 149-236	2-109 ; 149-236	2-109 ; 137-224	2-109 ; 137-224
Modifications to model	n-term acetylation	n-term acetylation	n-term acetylation	n-term acetylation
Simulation Conditions				
Simulation Box (Å)	147 x 147 x 174	147 x 147 x 174	147 x 147 x 174	147 x 147 x 174
Pressure (atm)	1	1	1	1
Temperature (K)	310	310	310	310
Time Step (fs)	2	2	2	2
Equilibration Time (ns)	30	30	30	30
Production Time (ns)	100	100	100	100
Production Replicas	2	2	2	2
Total Production Time (ns)	200	200	200	200

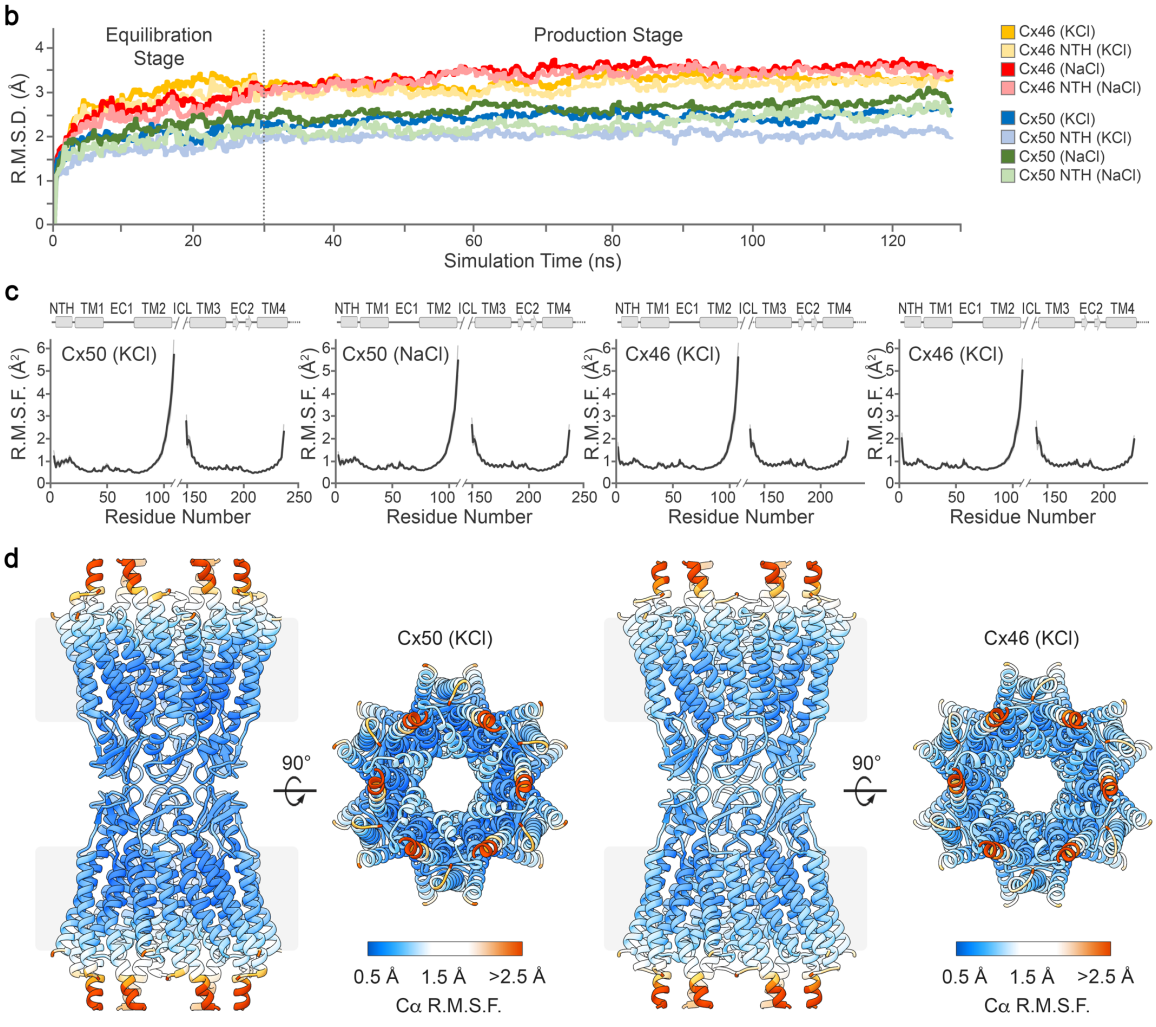

Supplementary Figure 7. Molecular dynamics setup and validation.

a) Summary of molecular dynamics (MD) simulation setup and conditions. Each simulation was setup similarly, using and explicit solvent model containing either KCl (Cx50KCl; Cx46 KCl) or NaCl

(Cx50 NaCl; Cx46 NaCl) in the cytoplasmic space, to match either cellular or in vitro conditions used for cryoEM studies, respectively. All simulations were conducted with NaCl in the extracellular space and using DMPC as the lipid system. Following minimization, all systems were equilibrated for 30 ns at 37° C, and multiple replicates (n = 2) of production (100 ns each) were acquired for analysis at 37° C. **b)** Cα root mean squared deviation (r.m.s.d.) analysis of equilibrium (0 – 30 ns) and production phases (30–130 ns) of the MD simulations, calculated with respect to the experimental starting structures, where Cx50 KCl (blue traces); Cx50 NaCl (green traces); Cx46 KCl (orange traces); Cx46 NaCl (red traces). Separate analysis for the n-terminal helix (NTH) domains are shown in lighter shades. **c)** Plot of average Cα root mean squared fluctuation (r.m.s.f.) during the production phase of the molecular dynamics (MD) simulations for Cx50 KCl (left), Cx50 NaCl (left center) Cx46 KCl (right center) and Cx46 NaCl (right). Averages are determined for the 12 subunits composing the intercellular channel, analyzed for both independent productions. Error bars (light grey shading) represent 95% confidence intervals (n = 24). Secondary structure and domain labels are indicated for the n-terminal helix (NTH), transmembrane helices (TM1-4), extracellular domains (EC1-2) and intracellular loop (ICL; not modeled). **d**) Representative r.m.s.f. values mapped to the experimental starting structures of Cx50 KCl (left) and Cx46 KCl (right). Colors correspond to r.m.s.f. amplitudes: < 0.5 Å (blue) – 1.5 Å (white) – 2.5 Å (red).

Supplementary Figure 8

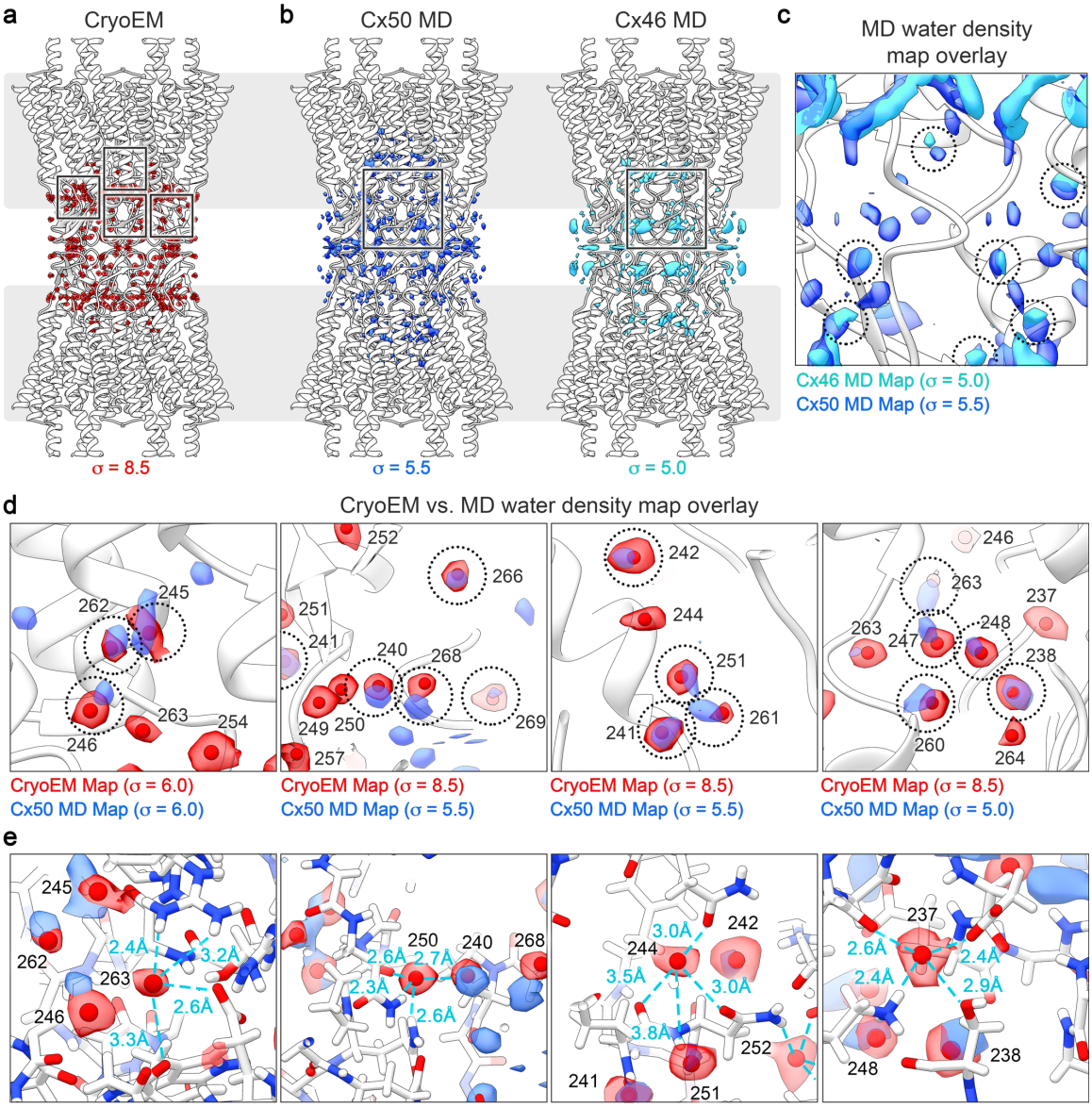

Supplementary Figure 8. Analysis of MD-based water density maps.

a) Ribbon structure of Cx46/50 with segmented water densities from the ensemble cryoEM map (red density, threshold = 8.5 σ). **b)** Ribbon structures of Cx50/46 with overlaid time-averaged and symmetrized water density maps calculated from MD-simulation for Cx50 (left; blue density, threshold = 5.5 σ) and Cx46 (right; cyan density, threshold = 5.0 σ). **c)** Zoom view, corresponding to boxed regions in panels b and c, showing overlaid MD-based water densities. Representative regions of overlapping density are circled. **d)** Zoom views of boxed regions in panel a, showing representative regions of cryoEM water densities (red) overlaid the Cx50 MD-based water density map (blue). Identities of modeled waters are indicated (using Cx50 numbering). Representative

regions of overlapping density are circled. 76% of waters modeled into the cryoEM map show corresponding density in the MD-based water maps. Density map threshold values (σ) used for visualization in each panel are indicated. **e**) Alternative views to those presented in panel d, depicting some of the water densities observed by cryoEM that were not also resolved in the MD-based density maps. To validate these sites, the local coordination to sidechain and/or backbone hydrogen bond partners were assessed (donor/acceptor distances < 4 Å, blue dashed lines).

Supplementary Figure 9

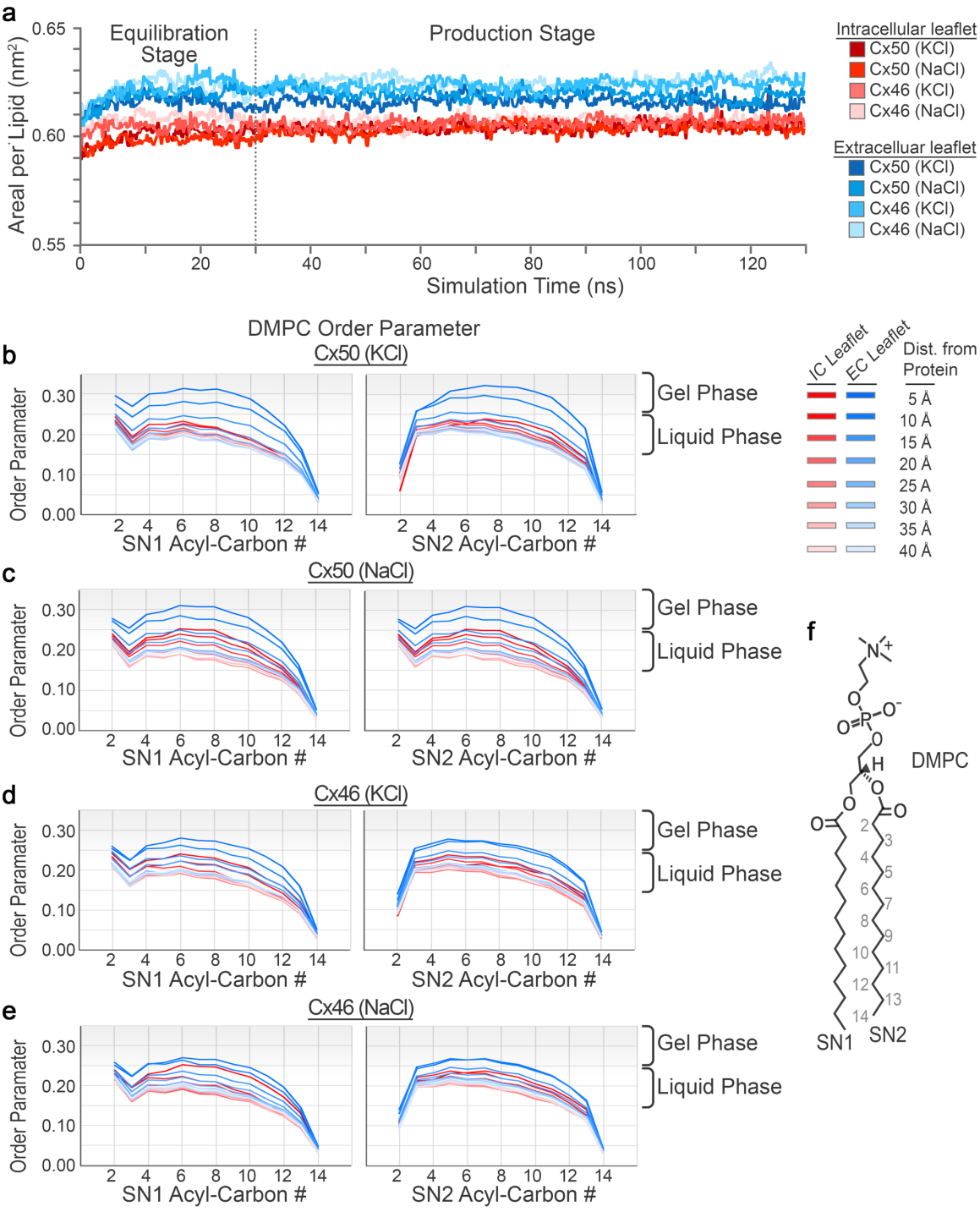

Supplementary Figure 9. Analysis of MD-based lipid dynamics.

a) Lipid equilibration was monitored by analyzing the averaged area per lipid (nm^2) over the duration of MD-simulation. Traces correspond to lipids from the extracellular leaflets (blue shades) and intracellular leaflets (red shades) for each system (Cx50 KCl, Cx50 NaCl, Cx46 KCl and Cx46 NaCl)

are displayed. **b-e)** Averaged lipid order parameters calculated for the SN1 (left) and SN2 (right) acyl-chain C-H bonds (S_{CD}) for each system (panel b, Cx50 KCl; panel c, Cx50 NaCl; panel d, Cx46 KCl; and panel e, Cx46 NaCl). Traces correspond to lipids from the intracellular leaflets (red, IC leaflet) and extracellular leaflets (blue, EC leaflet), with dark to light shading showing the radial distance dependence from the surface of the protein (5 Å shells). **f)** Structure of dimyristoyl phosphatidylcholine (DMPC) with SN1 and SN2 acyl-chains labeled.

Chapter 3: Binding and destabilization of the connexin-46/50 open-state by high-concentrations of cholesterol

Authors: Jonathan A. Flores[1] and Steve L. Reichow[1,2]

Affiliations:

[1] Department of Chemical Physiology and Biochemistry, Oregon Health and Science University, Portland OR 97239, U.S.A.

[2] Department of Chemistry, Portland State University, Portland OR 97201, U.S.A.

Respective Contributions

J.A.F. conducted the protein purification and reconstitution of cryoEM specimens. J.A.F. collected the cryoEM datasets, performed image analysis and atomic modeling. J.A.F. and S.L.R. contributed to the experimental design and structural interpretation. J.A.F. and S.L.R. contributed to manuscript preparation. S.L.R. provided overall guidance to the design and execution of the work.

This is an unpublished manuscript in preparation

Abstract

Gap junction channels are enriched in membrane domains that contain high concentrations of cholesterol. Cholesterol is a unique lipid component of biological membranes, both in its structure and biophysical properties. The potential functional consequence of this unique lipid on gap junctions is not well understood. The eye lens contains the highest concentrations of membrane cholesterol in the entire body, a result of age-related changes to the membrane environment of this unique organ. Here, we applied methods in single-particle cryoEM to elucidate the interaction(s) of cholesterol on native lens gap junctions (connexin-46/50). Our studies show that under typical membrane concentrations (25 mol%), cholesterol binds to specific annular sites located at both the inner- and outer-membrane leaflet of connexin-46/50. However, under very high concentrations (80 mol%) as found in the oldest regions of the lens, cholesterol binds at another site within the channel pore vestibule. This binding site appears to compete with the hydrophobic anchoring residues in the NTH-gating domain, and thereby dissociates and destabilizes the previously described open-state conformation of these channels. The resulting destabilized state of the NTH domain is suggested to induce altered channel properties. These findings provide novel insight into how age-related changes in the lens membrane environment may contribute to associated loss of connexin-46/50 channel activity and cataract formation, and potential clues for development of small-molecule drugs.

Introduction

The eye lens is the most cholesterol-rich tissue in the human body[71,90]. Remarkably, due to the unique cellular physiology required for transparency of this organ, lens fiber cells never turnover and the lipids (and proteins) that reside within the core of the lens are as old as the organism[7,70]. Despite the lack of lipid turnover, there is a dynamic age-related change in lens lipid composition as a result of selective degradation processes[75,231–233]. The mechanisms by which these changes occur and their potential effects on membrane proteins in the lens are nevertheless poorly understood. Enrichment in membrane cholesterol is perhaps the most well-characterized and dramatic of the many age-related changes in lens lipids[8–13]. While membrane cholesterol abundance is maintained at typical levels (~25 mol%) in the epithelium and young differentiating fiber cells, cholesterol levels within the oldest mature fiber cells in aged lenses can reach up to 80 mol%[90]. The physiological effect(s) of this highly enriched cholesterol environment are not known but may have significant consequences to the membrane proteins that play a critical role in maintenance of lens transparency and potentially contribute to age-related cataract formation.

In the avascular lens, gap junctions play a central role in forming a micro-circulatory system responsible for delivering ions and nutrients and removal of waste products[13,14]. The gap junctions form intercellular large-pore channels that directly couple the cytoplasmic environment of neighboring cells[22,235]. These channels typically aggregate together into large arrays, known as plaques, composed of 10’s to 1,000’s of intercellular channels. In this way, gap junctions

facilitate direct and rapid communication of electrical and chemical information throughout the body, with important roles in electrical coupling in the brain[236,237] and heart[238,239] and contribute to the long-range signaling and metabolic coupling of most tissues[235]. Gap junctional plaques are known to be enriched in cholesterol[96,167,240]; however, the structural and functional significance is unclear. Previous studies have shown that cholesterol can directly modulate the channel permeability of reconstituted Cx26 and Cx32 hemichannels[98]. Coarse-grained molecular dynamics simulations on Cx26 have also identified putative cholesterol binding sites at the cytoplasmic leaflet of these channels[99]. However, the mechanistic details of cholesterol binding and potential effects on channel function remain unclear.

Here, methods in single-particle cryoEM and lipid nanodisc technology were employed to elucidate the structures of native lens gap junctions (composed of connexin-46/50 intercellular channels), under varying cholesterol concentrations. We show that when reconstituted in typical cholesterol concentrations as found in the youngest regions of the lens (~25 mol%), Cx46/50 channels maintain the previously described ‘stabilized’ open-state conformation. Under these conditions, three specific cholesterol binding sites are resolved, localized at both the inner- and outer-leaflets of the membrane. Under cholesterol conditions that mimic the oldest regions of the eye lens (~80 mol% cholesterol), there are profound changes observed in the conformational state of the NTH-gating domain. These changes appear to be induced by a high-concentration cholesterol binding site located within the pore vestibule. Destabilization of the open-state is expected to induce

significant changes in channel properties that could be associated with the loss of cell-to-cell coupling in the mammalian lens associated with ageing[241,242]. These studies not only define novel structural and functional consequences of the cholesterol environment on connexin gap junctions, but also provide new insight into the potential pathophysiological consequences of the aged-lipid environment of the lens and cataract formation.

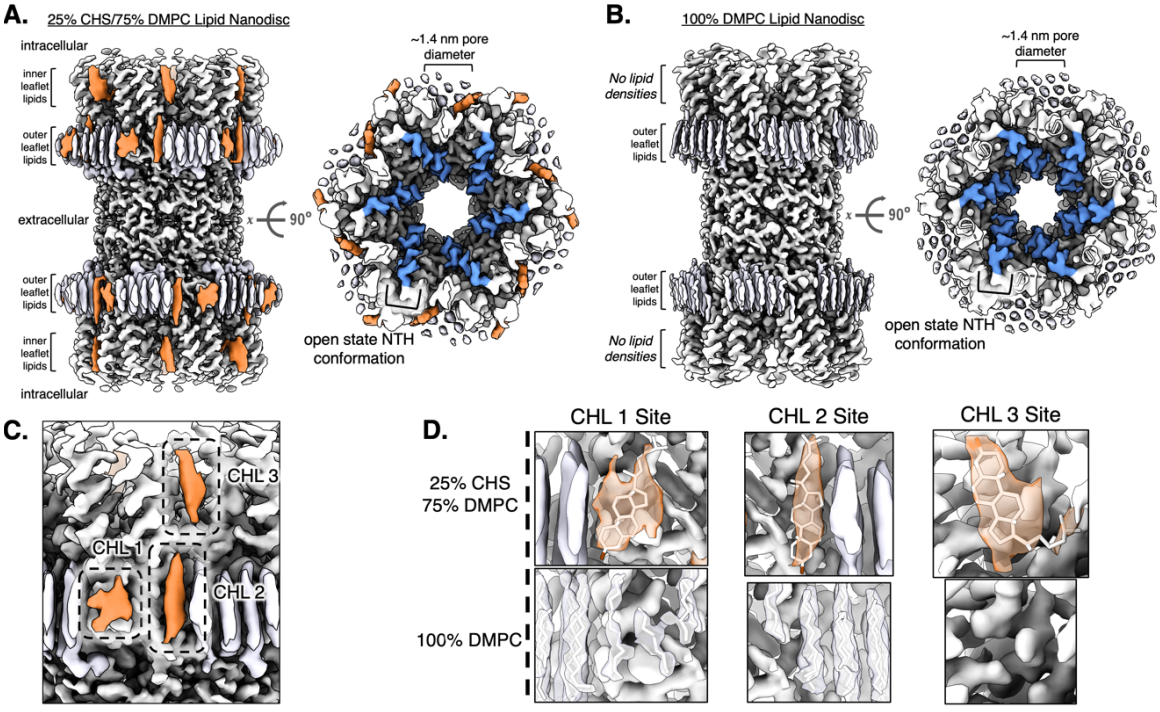

Figure 1 — Cx46/50 cryoEM structures reconstituted in lipid nanodiscs in the presence of 25 mol % cholesterol.

(A) CryoEM reconstruction of Cx46/50 gap junctions in lipid nanodiscs with 25 mol% cholesteryl hemisuccinate (CHS)/75 mol% dimyristoyl phosphatidylcholine (DMPC), and ***(B)*** the previously described cryoEM map obtained in 100% DMPC. Cx46/50 in 25% CHS retains the stabilized open-state NTH conformation observed in Cx46/50 in absence of CHS (compare blue densities). ***(C)*** Three new lipid densities were found in Cx46/50 reconstituted in 25% CHS lipid nanodiscs, assigned to CHL binding sites (CHL 1-3). Two outer leaflet cholesterol densities are bound to each connexin subunit in place of DMPC acyl chains (CHL 1 site, CHL 2 site). A third cholesterol density was found in the inner leaflet bound to each subunit (CHL 3 site). The equivalent site has no discernible lipid in absence of cholesterol.

Results

Structure of connexin-46/50 in 25% cholesterol lipid environment

Native (heteromeric/heterotypic) connexin-46/50 gap junctions were purified from sheep lens tissue[27]. Freshly purified channels were reconstituted into self-assembling lipid nanodiscs containing a mixture of pure dimyristoyl phosphatidylcholine (DMPC, 75 mol%) and cholesterol hemisuccinate (CHL, 25 mol%) at room temperature (~25° C), supported by the membrane scaffold protein MSP1E1[169,243] (see Methods). Under optimized conditions, the reconstitution resulted in a monodisperse population of intercellular channels embedded into a pair of lipid-nanodiscs, as assessed by size-exclusion chromatography and negative stain EM. The presence of both DMPC and CHL following reconstitution was confirmed by thin-layer chromatography (TLC) (*data not shown*).

Structure determination by high-resolution single particle cryoEM resulted in a high-quality 3D reconstruction (2.2 Å; gold-standard FSC) (Fig. 1A). The quality of the cryoEM map allowed for detailed stereochemical structural refinement of both Cx46 and Cx50. As described previously[27,243], the heteromeric pattern(s) of Cx46/50 co-assembly could not be unambiguously resolved, despite various attempts at computational image classification (see Methods). Nevertheless, atomic models of both Cx50 and Cx46 isoforms were equally well-fit into the D6-symmetrized cryoEM map, reflecting their close sequence and structural similarities (89% sequence similarity over the structured regions).

Gap junction intercellular channels are constructed by a dodecameric assembly, with six subunits assembled into ‘hemichannels’ that dock together

through extracellular domains, resulting in a continuous ~1.4 nm pore for intercellular permeation (Fig. 1A). The distance separating the two lipid nanodisc densities is ~3.5 nm (Fig. 1A), as previously described[131,132,243]. Each monomer consists of four transmembrane helices (TM1-4), two extracellular loops (EC1-2) that form the sites of docking interaction, and an amphipathic n-terminal helix

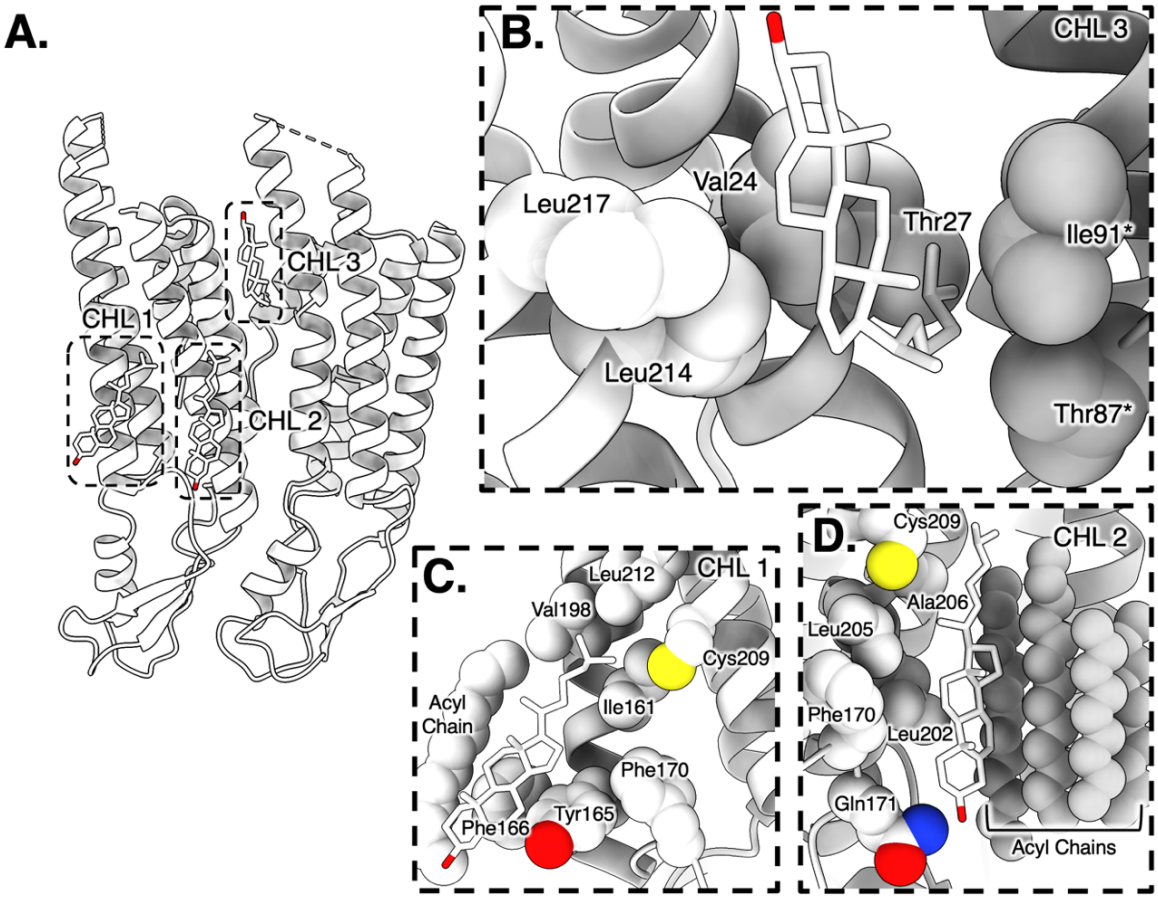

Figure 2 – Annular cholesterol binding sites in connexin-46/50.

(A) Overview of bound cholesterol molecules (stick representation) at annular sites of Cx46/50, indicated by dashed boxes. Only two protomers of Cx46 are displayed for simplicity. **(B)** CHL 3 is bound within the region of the inner lipid leaflet, at the subunit interface of neighboring connexin subunits. **(C and D)** A pair hydrophobic pockets in the region of the outer lipid leaflet is formed by aliphatic residues and DMPC acyl chains responsible for CHL binding (CHL 1 & CHL 2). The Oε of the hemisuccinate moieties in CHL 1 & 2 are stabilized by hydrogen bonding with Tyr165 and Gln 171, respectively.

(NTH), implicated in channel selectivity/gating, is well resolved in the previously described 'stabilized' open-state[27,243].

Overall, the density map obtained under 25 mol% CHL conditions appeared very similar to the map obtained in nanodiscs containing 100 mol% DMPC[243] (Fig. 1B). Under both conditions, the critical NTH-gating domain in Cx46/50 is captured in the same open-state conformation (Fig. 1A,B, blue densities). Indeed, model superpositions under these two conditions show they are nearly identical, and a similar set of stabilized water molecules are found at equivalent sites.

In contrast to similarities in the protein structure, there are marked changes to the features resolved within the lipid nanodiscs (Fig. 1A,B). Under 100 mol% DMPC, lipids are resolved only within the outer leaflet and appear as ordered clusters of rod-like densities at the connexin subunit interface (Fig. 1B). The rod-like densities extend several solvent layers beyond the annular protein-lipid interface. This remarkable feature has been attributed to DMPC acyl chains that have been highly stabilized through interactions with Cx46/50, resulting in a gel-like state that extends several solvent layers from the protein surface[243]. Under conditions of 25 mol% CHL, most of the same acyl chain densities are resolved at similar positions. However, disc-like densities are also observed occupying binding sites within the extracellular and intracellular leaflet of the bilayer (Fig. 1A, orange). These disc-like densities are attributed to resolved CHL molecules, bound at annular sites along the TM3/4 region of Cx46/50 channels (Fig. 1C). This assignment is based on the morphological differences of these lipid densities, as compared to the DMPC only map, and close fit of atomic models of CHL built into

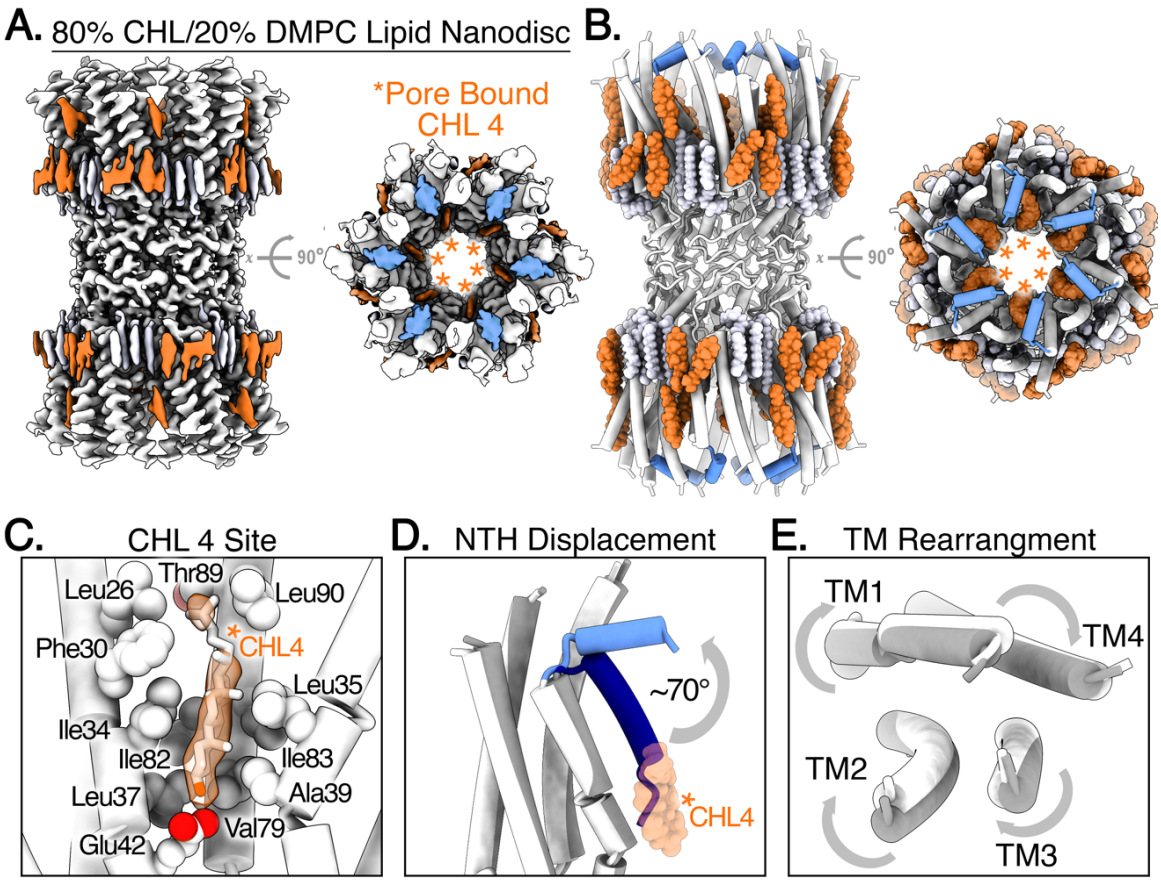

Figure 3 – The NTH-gating domain of Cx46/50 is displaced and destabilized in the presence of 80 mol % cholesterol.

(A) cryoEM reconstruction of Cx46/50 gap junctions in lipid nanodiscs with 80 mol% cholesteryl hemisuccinate (CHS)/20 mol % dimyristoyl phosphatidylcholine (DMPC), and ***(B)*** corresponding atomic model. Protein shown as tube-representation and lipids shown as space-filling models. Asterisks indicate locations of newly resolved CHL sites (CHL4), orange. The NTH domain is indicated in blue. ***(C)*** Molecular details of the pore-bound CHL4 site. CHL4 forms interactions with many of the same hydrophobic residues on TM1/2 that are involved in stabilizing the open-state of the NTH under 0 and 25 mol % cholesterol. ***(D)*** Superposition of Cx46/50 in the presence of 80 mol % CHL (white and light blue NTH) and 25 mol % CHL (grey and dark blue NTH). CHL4 displayed in transparency. ***(E)*** Illustration of conformational re-arrangements of the TM domains (TM1-4) that coincide with NTH domain movements shown in panel D, under high CHL conditions.

these sites (Fig. 1D). In total, three cholesterol molecules are resolved at each subunit (totaling 36 CHL molecules resolved in the dodecamer). Within the

extracellular leaflet, each subunit binds two CHL molecules (CHL1 & 2), and a third CHL molecule is clearly resolved within the region of the intracellular lipid leaflet (Fig. 1A,C,D). Remarkably, the identification of a lipid density in the intracellular lipid leaflet is unique when compared to the DMPC only map, and further supports the notion that Cx46/50 forms leaflet-specific interactions with the lipid environment (see Discussion).

Molecular details of annular cholesterol binding sites

The two CHL molecules localized within the extracellular leaflet appear to displace lipid acyl-chain densities observed in the DMPC-only structure[243]. CHL1 is bound within a pocket formed by hydrophobic sidechains from TM3, and additional hydrophobic interactions from a neighboring DMPC acyl-chain (Fig. 2A,C). In addition, Tyr165 forms a hydrogen bond involving its sidechain hydroxyl and the Oε of the hemisuccinate moiety (equivalent to hydroxyl O1 in cholesterol) (Fig. 2C). CHL2 is sandwiched between a set of hydrophobic residues displayed by TM4, and a cluster of DMPC acyl-chains (Fig. 2A,D). The Oε of the hemisuccinate moiety at this site appears to be bound through hydrogen bonding interactions with the sidechain of Gln171 (Arg183 in Cx50). For both CHL1 and CHL2, hydrogen bond interactions with the Oε oxygen orient the bound CHL, fixing the hydroxyl moiety toward the solvent interface of the outer leaflet.

The third CHL is bound at the inner leaflet of the membrane (Fig. 2A,B) and appears deeply intercalated at the lateral interface of neighboring connexin subunits. Intimate interactions between CHL3 and hydrophobic residues from

TM1/4 and TM2 form this intersubunit binding site. The residues involved in all CHL binding sites (CHL1-3) are well conserved between Cx46 and Cx50, and generally well conserved with other connexin isoforms. The degree of conservation might indicate similarly conserved CHL binding properties in other connexins.

The NT-gate of Cx46/50 is destabilized in 80% cholesterol lipid environment

To assess the effects cholesterol enrichment, as found in the oldest regions of the ocular lens, native Cx46/50 channels reconstituted into MSP1E1 nanodiscs in the presence of 80 mol% CHL and 20 mol% DMPC (following the same method used for Cx46/50 in 25 mol% CHL) and subjected to cryoEM single-particle analysis. This resulted in a 3D reconstruction and refined atomic model, resolved at a global resolution of 2.2 Å (gold-standard FSC) (Fig. 3A), comparable in quality to map obtained in 25 mol% CHL conditions.

In addition to the three annular CHL sites at the protein-lipid interface (CHL1-3) resolved in 25 mol% cholesterol, a fourth CHL site is clearly resolved within the channel vestibule (termed CHL4) (Fig. 3A,B, *asterisk*). The binding pocket for CHL4 is defined by hydrophobic residues displayed by pore lining TM1/2 (Fig. 3C). The Oε of the hemisuccinate moiety is oriented toward the middle of the channel (away from the pore opening) and positioned in proximity to Glu42.

In the stabilized open-state conformation observed under 0 and 25 mol% CHL, the NTH-gating domain (residues 2-20) forms a regular amphipathic helix in Cx46/50 that folds into the pore vestibule to form a constriction site[27,243]. In this conformation, the NTH is well positioned to function as a selectivity filter/gating

domain[27,244,245]. The hydrophobic face of the NTH is established by a set of aromatic and hydrophobic residues that are conserved across various connexin isoforms[27]. These anchoring sites pack against the pore lining helices (TM1/2) along the interface of neighboring subunits (Fig. 3D, *dark blue*). CHL4 binds at the same TM1/2 site that is used to stabilize the open-state of the NTH domain, and effectively displaces the NTH away from the pore vestibule. In this CHL-bound state, the NTH swings ~70° toward the opening of the channel (Fig. 3D, *light blue*). In this displaced state, only the distal residues 7-20 of the NTH domain are well-resolved. The proximal residues 2-6 are unresolved, likely due to the loss of stabilizing interactions within the pore. Although the proximal region of the NTH is unresolved, these disordered residues would be oriented toward the center of the pore, presumably occluding (or partially occluding) the permeation pathway.

Accompanying the displacement and destabilization of the NTH-gating domain are coordinated re-arrangements of the TM helices. TM1 (which is directly connected to the NTH) moves away from the center of the channel toward TM4 (Fig. 3E). This is further associated with a rather dramatic movement of TM2 toward the pore, with more modest rearrangements of TM3/4 to maintain TM packing interactions.

Overall, these concerted movements can be described as an overall rotation of TM helices in a clockwise direction, when looking down from the cytoplasmic view of the channel (Fig. 3E). This rearrangement draws the distal region of the NTH away from the center of the channel, while movement of TM2 toward the displaced NTH apparently stabilizes this newly-described lifted

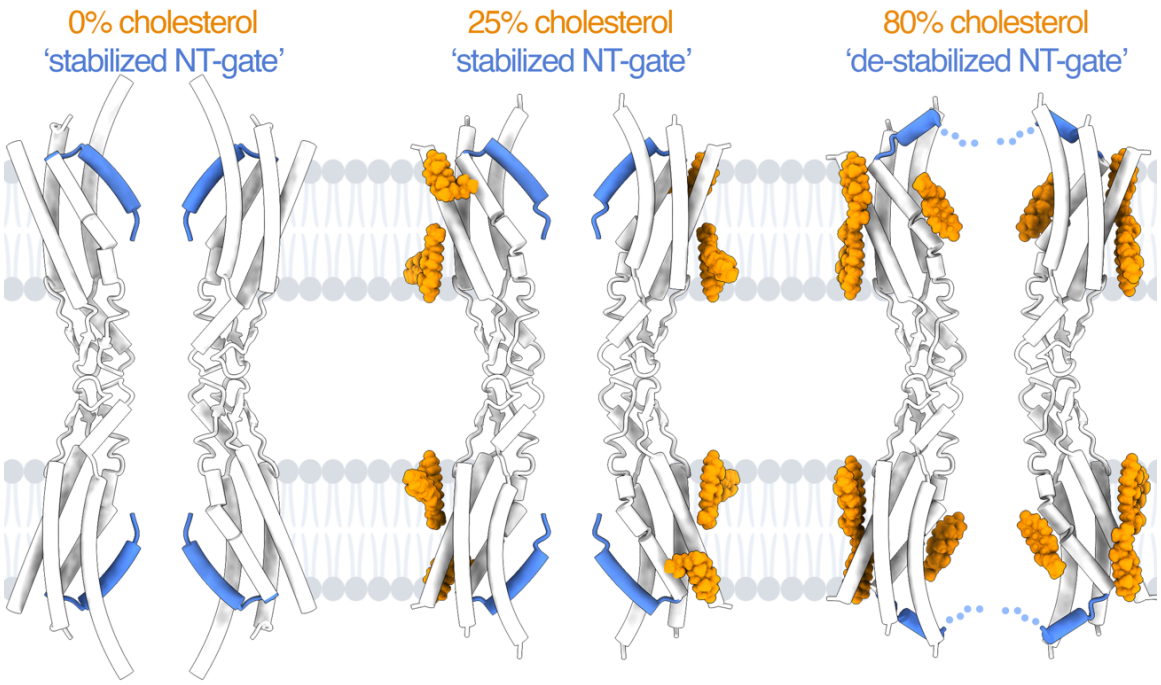

Figure 4 – Overview of CHL binding sites in Cx46/50 and conformational changes induced under high-cholesterol conditions.

Under conditions of 0 and 25 mol% cholesterol *(left and center, respectively)*, Cx46/50 intercellular channels adopt a stabilized open-state conformation, with the NT-gate (blue) folded into the pore lumen. Under normal cellular conditions (25 mol%), cholesterol occupies specific sites at the protein-lipid annular interface, localized at both the inner- and outer-lipid leaflets. Under hyper-enriched cholesterol conditions analogous to the membrane environment in the oldest lens regions, the NT-gate is displaced by cholesterol binding at a pore-lining TM1/2 site. In this displaced conformation, the NT-gate is relatively disordered and positioned toward the center of the pore, potentially occluding the permeation pathway.

conformation. Remarkably, displacement of the NTH domain and occupancy of CHL4 site dramatically alters the both the steric and electrostatic profile of the permeation pathway. The functional implications of these profound changes to the cell-to-cell communication pathway are discussed below.

Discussion

The gap junctions exist in regions of biological membranes that are enriched in cholesterol[91,93,94,167,246–248]. The work described here shows that cholesterol forms specific interactions with Cx46/50 intercellular channels, with relatively well-defined sites located at both the intracellular and extracellular lipid leaflets. The selectivity of Cx46/50 with PC lipids at the extracellular leaflet, coupled with the site-specific interactions with CHL resolved in this study, further highlight the degree to which these channels intimately associate with their lipid environment. Under normal cellular concentrations, CHL does not appear to significantly alter the functional state of Cx46/50, which is shown to retain the stabilized open-state that was resolved in PC-only membranes (see overview, Fig. 4). This is consistent with functional studies on Cx26 and C32 that show peak channel permeation under conditions of ~25 mol % CHL[98]. Remarkably, under very high concentrations (as found in the oldest regions of the eye lens), CHL may bind additional sites within the pore lumen of Cx46/50 and displace the NTH domain from its open-state. In this displaced conformation, the NTH points toward the center of the pore and becomes destabilized (Fig. 4, *dotted lines*). The functional consequences of this novel state are still unclear, but these conformational changes are expected to result in significant alteration to channel properties[244]. It is also unclear how cholesterol penetrates the pore lumen of the channel from the lipid bilayer. In the related Innexin channels, lipids have been proposed to migrate from the surrounding bilayer through fenestrations between adjacent subunits[249]. It is

possible that under high-concentrations, cholesterol may penetrate connexin channels in a similar way.

The NTH of Cx46/50 (and other connexins) is well-recognized as a key modulator of channel permeation[106,244,245,250–252], selectivity[175,253], and gating[177,254–257]. In the destabilized state (with CHL bound in the pore), substrate permeation would likely be at least partially occluded by the proximal regions of the NTH. Furthermore, the electrostatic environment that dictates permeation and selectivity would be significantly altered, as compared to the open-state. Indeed, the described destabilized state may resemble the gated (or closed) state of these channels induced by other physiological signals (such as pH[59,85] and voltage[152,258]). Interestingly, Cx46/50 coupling in the lens has been shown to diminish to ~30% activity within the oldest regions of the lens[241]. The mechanistic explanation for this age-related loss of channel function is still not understood but has been proposed to be associated with age-related changes in lens pH[15,58], Ca^{2+} levels[18,68] and accumulation of post-translational modifications[48,49]. Based on the results presented here, it is argued that age-related changes to the lipid environment may be—at least in part—responsible for the loss of Cx46/50 channel activity in aged lens fiber cells. If true, such a mechanism may contribute to a diminished nutrient circulation and waste removal, resulting in compromised lens transparency and eventual cataract formation. Further studies are needed to resolve the functional effects induced by such interactions with CHL in the lens, and how these interactions may contribute to disease phenotypes associated with cataract.

Lastly, it is noted that many gap junction inhibitors contain sterol-like chemical moieties[259]. The molecular details associated with CHL-induced destabilization of the NTH-gate (and potential closure of the channel), may thus provide key insights into the pharmacology of these and potentially other connexin inhibitors. Connexins are associated with wide-ranging disease states affecting various tissue types (including blindness, deafness, skin disorders, arrhythmia, stroke and cancer)[107,110,117,165]. As such, these channels have been proposed as viable therapeutic targets for many types of human disease[260,261]. The molecular insights illuminated here may provide key mechanistic details and molecular blueprints to enable structure-guided methods for the development of potent and selective connexin inhibitors (which are generally desperately in the field).

Methods

MSP expression and purification

A bacterial expression plasmid encoding MSP1E1 was obtained from Addgene[169]. MSP1E1 was expressed and purified as described[170,243]. Final protein concentration was determined by UV absorbance at 280 nm. Samples were aliquoted, flash frozen in liquid nitrogen and stored at –80°C for up to several months.

Cx46/50 purification and nanodisc reconstitution

Native Cx46/50 intercellular channels were isolated from ovine lens fiber cells[27,243]. Lamb eyes obtained from Wolverine Packers slaughterhouse (Detroit, MI) were dissected and fully intact lenses were stored at -80°C. Gap junctions were isolated from core lens tissue to obtain a homogeneous sample of the c-terminal truncated variant of Cx46/50 (a.k.a. MP38)[37,38,45,121]. Details of the purification procedure are provided below.

Lenses were thawed from -80°C and core lens was dissected from cortex with a surgical blade. Stripped fiber cell membranes were prepared as described[201–203]. Protein concentration was determined by BCA (Pierce) and membranes were stored at -80°C in Storage Buffer (10 mM Tris [pH 8.0], 2 mM EDTA, 2 mM EGTA) at ~2 mg mL^{-1} total protein. Stripped membranes were solubilized with Storage Buffer with 20 mg mL^{-1} n-decyl-β-D-maltoside (DM; Anatrace) for 30 minutes at 37°C with gentle agitation. Insoluble material was

cleared by ultracentrifugation at ~150,000 x *g* for 30 minutes at 4°C. Supernatant was filtered (Millipore; 0.22 μm) and separated by ion-exchange chromatography (UnoQ, BioRad) with Buffer A (Storage Buffer with 3 mg mL^{-1} DM). Protein was eluted with a 25 CV gradient of Buffer B (Buffer A with 500 mM NaCl). Elution peaks containing Cx46/50 (confirmed by SDS-PAGE) were pooled and separated by size exclusion chromatography (SEC; Superose 6 Increase 10/300 GL; GE Healthcare) with SEC buffer (20 mM HEPES [pH 7.4], 150 mM NaCl, 2 mM EDTA, 2 mM EGTA and 3 mg mL^{-1} DM). Peak Cx46/50 fractions were pooled and concentrated to ~5 mg mL^{-1} (Vivaspin 6; 50-kDa MWCO; Sartorius). Protein concentration was measured by UV_{280} absorbance. All chromatography steps were performed by FPLC at 4°C.

Freshly purified Cx46/50 was reconstituted into MSP1E1 nanodiscs using dimyristoyl phosphatidylcholine (DMPC; Avanti) and cholesteryl hemisuccinate (CHS; Avanti), following established procedures with slight modification[170,204,243]. Lipids in chloroform were dried under N_2 gas and left under vacuum overnight to remove residual chloroform. The resulting thin films were resuspended in 50 mg mL^{-1} DM and sonicated at 37°C for 2 hours. For 25% CHS nanodiscs, DMPC and CHS were combined at a 3:1 molar ratio (3.75 mM DMPC, 1.25 mM CHS). For 80% CHS nanodiscs, DMPC and CHS were combined at a 1:4 molar ratio (1 mM DMPC, 4 mM CHS). DMPC/CHS mixtures were gently vortexed at room temperature for 30 seconds. Cx46/50 (~5 mg mL^{-1}) in SEC Buffer was combined with DMPC/CHS at a final molar ratio of 0.6:75:25 (Cx46/50:DMPC:CHS) for 25% CHS nanodiscs, and 0.6:80:20 for 80% CHS nanodiscs. Cx46/50 with lipids was gently pipetted to

mix and incubated at 25°C with gentle agitation for 2 hours. Purified MSP1E1 was added for a final molar ratio of 0.6:1:100 (Cx46/50:MSP1E1:lipids) for both 25% and 80% CHS nanodisc reconstitutions. After addition of MSP1E1, reconstitution mixtures were incubated at 25°C for 30 minutes. DM was removed with Bio-Beads SM-2 resin (BioRad) at a ratio of 20:1 beads:detergent (wt wt^{-1}) by overnight (12-16 hours) incubation at 25°C with gentle agitation. Bio-Beads by making a single perforation to the top and bottom of the Eppendorf tube with a hot needle. The perforated tube was gently centrifuged (~500 x *g*) into a new tube with fresh Bio-Beads (20:1 wt wt^{-1}) and incubated for a final 2 hours at 25°C. After removing the 2^{nd} Bio-Bead batch, samples were ultracentrifuged at ~150,000 x *g* for 15 minutes at 4°C to remove insoluble material. Filtered supernatant (Millipore; 0.22 μm) was separated by SEC (Superose 6 Increase 10/300 GL; GE Healthcare) with SEC Buffer to remove empty nanodiscs from Cx46/50-nanodiscs. Peak Cx46/50-nanodiscs (confirmed by SDS-PAGE) were pooled and concentrated (Vivaspin 6; 50-kDa cut-off filter; Sartorius) to a final concentration ~2.5 mg mL^{-1} (confirmed by UV_{280} absorbance). Chromatography steps were performed by FPLC at 4°C.

CryoEM specimen preparation and data collection

25% CHS samples were prepared for cryoEM by applying 5 μl freshly purified Cx46/50-nanodiscs (~2.1 mg mL^{-1}) to a glow-discharged holey carbon grid (Quantifoil R 1.2/1.3, 400 mesh) for 8.0 seconds. The grid was blotted for 5.0 seconds (3.0 seconds dwell time) and plunge frozen in liquid ethane using a

Vitrobot Mark IV (Thermo Fisher Scientific) at 100% humidity and stored under liquid nitrogen.

Vitrified 25% CHS Cx46/50 nanodiscs were imaged on a Titan Krios (Thermo Fisher Scientific) operated at 300 kV. Dose-fractionated image stacks were recorded on a K3 Direct Electron Detector (Thermo Fisher Scientific) at 120,000x nominal magnification in super-resolution mode with a physical pixel size of 0.8015 Å $pixel^{-1}$ (0.40075 Å $pixel^{-1}$ super-resolution). The dose rate was 0.8 e^{-} $pixel^{-1}$ sec^{-1} with a total dose for each exposure of ~38 e^{-} $Å^{-2}$. A dataset of 7,250 movies was obtained with nominal defocus values ranging from 0.3-1.5 μm, and data collection parameters were controlled in an automated manner using serialEM[262].

80% CHS samples were prepared by application of 5 μl freshly purified Cx46/50-nanodiscs (~2.4 mg mL^{-1}) to a glow-discharged holey carbon grid (Quantifoil R 1.2/1.3, 400 mesh) for 8.0 seconds. The grid was blotted for 4.0 seconds (3.0 seconds dwell time), plunge frozen in liquid ethane (Vitrobot Mark IV; Thermo Fisher Scientific) at 100% humidity and stored under liquid nitrogen.

Vitrified 80% CHS Cx46/50 nanodiscs were imaged on a Titan Krios (Thermo Fisher Scientific) operated at 300 kV. Dose-fractionated image stacks were recorded on a K3 Direct Electron Detector (Thermo Fisher Scientific) at 130,000x nominal magnification (super-resolution mode) with a physical pixel size of 0.648 Å $pixel^{-1}$ (0.324 Å $pixel^{-1}$ super-resolution). The dose rate was 0.56 e^{-} $pixel^{-1}$ sec^{-1} with a total dose for each exposure of ~29.5 e^{-} $Å^{-2}$. A dataset of 3,245 movies was obtained with nominal defocus values ranging from 0.5-2.0 μm, and

data collection parameters were controlled in an automated manner using serialEM[262].

CryoEM image processing for Cx46/50 in 25 mol% CHL nanodiscs

The entire dataset of 7,426 movies was subjected to beam-induced motion correction with MotionCor2[263] and contrast transfer functions (CTFs) were estimated with Gctf[208]. Micrographs with CTF models worse than 5 Å resolution were discarded and the remaining 7,204 micrographs were used for subsequent processing steps. The blob-picker in cryoSPARC (Structura Biotechnology; v2.15.0)[264] was used to pick an initial set of 4,690,010 particles. Two rounds of 2D classification were used to generate a cleaned particle stack (177,094) that was used for *ab initio* reconstruction in cryoSPARC. Homogeneous refinement (D6 symmetry applied) yielded a map at 5.21 Å resolution. This map was lowpass-filtered to 20 Å and 20 uniquely spaced orientations were projected as templates to pick 8,355,567 particles. Four rounds of heterogeneous refinement (without symmetry) yielded a cleaned set of 588,774 particles that refined to 2.31 Å resolution after non-uniform refinement[265] in cryoSPARC (320-pixel box, 1.00 Å pix^{-1}). The particle stack was culled to 474,448 after a final round of heterogeneous refinement in cryoSPARC with D6 symmetry applied. After removal of duplicate particles (100 Å minimum distance), the remaining 470,213 particles were refined to 2.24 Å resolution after another round of non-uniform refinement. Postprocessing and local resolution estimation was performed in cryoSPARC and local resolution-filtered maps were generated from atomic model refinement.

CryoEM image processing for Cx46/50 in 80 mol% CHL nanodiscs

The entire dataset of 3,245 movies was subjected to beam-induced motion correction with MotionCor2[263] and contrast transfer functions (CTFs) were estimated with Gctf[208]. Micrographs with CTF models worse than 5 Å resolution were discarded and the remaining 3,063 micrographs were used for subsequent processing steps. The blob-picker in cryoSPARC (Structura Biotechnology; v2.15.0)[264] was used to pick an initial set of 1,726,707 particles. 2D classification was used to yield a refined set of 181,562 particles. An *ab initio* model was generated in cryoSPARC, and homogeneous refinement with D6 symmetry yielded a map at 4.98 Å resolution. CryoSPARC was used to lowpass-filter this map to 20 Å, and 50 uniquely spaced orientations were projected as templates to pick 3,312,377 particles. Two rounds of heterogeneous refinement in cryoSPARC (without symmetry) yielded a set of 325,495 particles. Non-uniform refinement[265] in cryoSPARC yielded a 3D reconstruction at 2.48 Å (256-pixel box, 1.215 Å pix^{-1}). Particle re-extraction (300-pixel box, 1.037 Å pix^{-1}) and duplicate removal (75 Å minimum distance) improved the resolution to 2.29 Å. The refined stack of 306,503 particles was converted from cryoSPARC to RELION format with UCSF PyEM (v.0.5)[266].

Bayesian polishing and CTF refinement (per-particle defocus, per-micrograph astigmatism, beam-tilt refinement, 3rd order aberration correction, 4th order aberration correction) with 3D refinement (D6 symmetry) in RELION-3.1[207,209] yielded a map at 2.53 Å resolution (320-pixel box, 0.972 Å pix^{-1}). An initial atomic model was fit into the unsharpened map from 3D auto-refine (see Atomic

modelling, refinement, and validation below) and a 15 Å-resolution map was simulated from the atomic model using the molmap tool in UCSF ChimeraX[212]. A mask was generated from the 15-Å molmap (0.1 initial threshold, 2-pixel extension, 2-pixel soft edge). The molmap-based mask was applied during 3D classification without alignment (D6 symmetry, 10 Å initial lowpass filter, *k*=6, *T*=4) in RELION. After 100 iterations, one of the six classes were empty. A "destabilized" NT-gate was identified in three of the six classes (106,303 particles altogether). A 5th class with 32,934 particles resembled the stabilized open-state NT-gate previously described for Cx46/50[27,243]. Finally, a sixth class showed features of both the "destabilized" NT-gate and the stabilized open-state NT-gate. A final round of Bayesian polishing and CTF refinement on the "destabilized" NT-gate particles yielded a 2.2 Å resolution map (D6 symmetry, 320-pixel box, 0.875 Å pix^{-1}). Postprocessing and local resolution estimation was performed in RELION and local resolution-filtered maps were generated for atomic model refinement.

Atomic modelling, refinement, and validation

Initial atomic models of Cx46 (7JKC) and Cx50 (7JJP) were fit as rigid bodies into the 2.2 Å "destabilized" NT-gate cryoEM map. After deletion of lipid acyl chains and solvent, all-atom models for Cx46 and Cx50 were subjected to several iterations of manual adjustment with COOT[213] followed by real-space refinement in PHENIX[214] with secondary structure and non-crystallographic symmetry (D6) restraints applied. Model quality was monitored at each iteration with MolProbity[215]. Coordinate and restraint files for DMPC (PDBe Ligand Code: MC3) and CHS

(PDBe Ligand Code: Y01) were generated with PHENIX eLBOW[217]. DMPC and CHS ligands were manually fit into the cryoEM density with COOT. Atoms in DMPC and CHS that could not be accommodated by the density were deleted. Several iterations of real-space refinement on the entire model were completed until refinement statistics converged.

Chapter 4: Calcium induced gating at the NT-domain of connexin-46/50 gap junctions

Authors: Jonathan A. Flores[1, †], Susan E. O'Neill[2, †], and Steve L. Reichow[1,2,†]

Affiliations:

[1] Department of Chemical Physiology and Biochemistry, Oregon Health and Science University, Portland OR 97239, U.S.A.

[2] Department of Chemistry, Portland State University, Portland OR 97201, U.S.A.

[†] Indicates equal contribution

Respective Contributions

S.E.N. and J.A.F. contributed equally to the work. S.E.N. conducted the protein purification and reconstitution of cryoEM specimens. S.E.N. collected the cryoEM datasets. S.E.N. and J.A.F. performed image analysis. J.A.F. contributed to atomic modeling. J.A.F., S.E.N., and S.L.R. contributed to the experimental design and structural interpretation. J.A.F. and S.L.R. contributed to manuscript preparation. S.L.R. provided overall guidance to the design and execution of the work.

This is an unpublished manuscript in preparation

Abstract

Gap junctions form cell-to-cell communication pathways that enable electrical and metabolic coupling throughout the body and are associated with a range of disease states. In cases of tissue injury (e.g., heart attack and stroke) gap junctional communication pathways can be decoupled by high intracellular calcium (Ca^{2+}) levels, as a mechanism for preventing damaged cells from impacting healthy tissues. Despite decades of intense interest, details defining this mechanism of gap junctional gating remain unclear and highly debated. Here, we describe the Ca^{2+} induced gating of native lens Cx46/50 gap junction channels revealed by single particle cryoEM. The structures resolve many novel features and capture several components of previously proposed models of Ca^{2+} induced gating of gap junction channels. These include resolving multiple Ca^{2+} binding sites localized within the pore, which result in a variety of occluded/gated states involving the n-terminal helix (NT) domain. In addition, there is evidence for subunit rearrangements that result in pore collapse, facilitating steric blockade of the permeation pathway by the NT domains, reminiscent of the 'iris model' of channel gating proposed nearly 40 years ago. Together, these results offer key insights to understanding how Ca^{2+} mishandling in the lens (and other tissues) result in gap junction uncoupling.

Introduction

Gap junctions form cell-to-cell communication channels that are ubiquitously expressed throughout the human body, where they play key roles in electrical and metabolic coupling, and long-range cellular communication[162,235]. Due to their central roles in diverse physiological processes, aberrant gap junctional communication is associated with a range of disease states (including blindness, deafness, arrhythmia, stroke, skin disease and cancers)[107,110,117,165,260]. In cases of tissue injury (e.g., heart attack and stroke), ischemic conditions result in release of Ca^{2+} into the cytoplasm that may contribute to the spread of cytotoxic signaling to surrounding cells and/or tissue. Thus, a key mechanism for regulating gap junctional coupling is Ca^{2+}-induced closure, as a means for decoupling damaged cells from healthy tissues. Despite this critical role, gaining detailed mechanistic understanding for this regulatory mechanism has proven elusive and controversial.

Gap junction intercellular channel formation is achieved through an assembly of twelve subunits, known as connexins[25,141,166]. Each connexin monomer consists of four transmembrane helices (TM1-4), two extracellular loops (EC1-2) that form the sites of docking interaction and an amphipathic n-terminal helix domain (NT), implicated in channel selectivity/gating. Within the plasma membrane, six connexins are organized into a hemichannel structure. Hemichannels from neighboring cells dock together to form complete cell-to-cell channels, which may cluster together to form large gap junctional plaques. These channels establish a remarkably large pore that provides passage to an array of chemical information, including ions, metabolites, hormones, and other small

signaling molecules up to ~1 kDa in size (*e.g.,* K^+, cyclic AMP, inositol triphosphate, and glucose). In this way, interconnected cells may exchange electrical and chemical information across entire tissues or organs.

Regulation of cell-to-cell coupling is physiologically controlled by a variety of mechanisms: pH[267], phosphorylation[88,268], lipids[98], membrane potential[269], transjunctional voltage (V_j)[270,271], and biologically active divalent cations, including Mg^{2+} [256,272] and Ca^{2+} [273,274]. The functional roles of Ca^{2+} gating in gap junction intercellular channels and hemichannels are distinct. While gap junctions exist primarily in an open-state under resting V_j conditions and are gated by high intracellular Ca^{2+} induced by extreme cell-stress, hemichannels are typically maintained in a closed state under resting membrane potentials and normal external concentrations of Ca^{2+} (~1.8 mM)[274]. However, it remains unclear if the mechanisms used to close these two types of channels in response to high Ca^{2+} conditions are fundamentally different.

Early low-resolution X-ray and cryoEM studies performed on liver gap junctions[133,134,275] suggested significant subunit rearrangements and conformational changes in the presence of Ca^{2+}. This led to the proposed 'iris model' of gap junctional gating in that prevailed for ~30 years, in which connexin subunits rearrange to constrict the pore—reminiscent of a camera iris. Such structural perturbations in response to Ca^{2+} were consistent with AFM studies conducted on Cx26 hemichannels[276]. However, this model was finally challenged in 2016, when X-ray structures of amphipol-stabilized human Cx26 were obtained by the Yeager laboratory in the presence and absence of 20 mM Ca^{2+} resolved at

3.3 Å and 3.8 Å, respectively[105]. The two structures were nearly identical, except for the presence of a single Ca^{2+} ion bound at each subunit interface, chelated by E42 and E47 (and G45 backbone carbonyl) at the pore-lining EC1 domains of the dodecameric channel. Based on these observations and MD simulation studies, the authors ruled out large-scale structural changes, proposing an electrostatic barrier mechanism responsible for regulating ion conduction[105]. However, an important caveat to this work was that the NT domains, which are thought to play a critical role in ion permeation and channel gating[25,141,245,254,277–280], were not resolved in either of these X-ray structures. Thus, it remained unclear if Ca^{2+}-induced structural changes to this cytoplasmic-facing gating domain occurred.

Recent single-particle cryoEM structures of detergent solubilized Cx31.3 hemichannels have been obtained in the presence and absence of 50 mM Ca^{2+}, resolved at 2.3 and 2.5 Å, respectively[106]. Here again, the overall structures appear nearly identical. In this study, the location of bound Ca^{2+} ions could not be confidently assigned; however, subtle conformational changes were described within an aqueous tunnel formed by the EC domains, including residue E47, E187 and D66. In contrast to the apo- and Ca^{2+}-bound Cx26 structures, the NT domains of Cx31.3 were resolved, and found to adopt a unique lifted conformation in both conditions that occluded the pore diameter to ~8 Å. However, it is noted that a detergent or lipid molecule embedded within the channel may have contributed to the lifted NT conformations—for which the physiological relevance is unclear. Indeed, it was shown by equilibrium-state MD simulation that ions still permeate the pore of these channels, although complete pore closure of hemichannels may

require transmembrane voltage potential. Furthermore, the aqueous tunnel in Cx31.3 implicated in Ca^{2+} recognition is completely blocked in the Cx26 and Cx46/50 structures, indicating that the Ca^{2+} binding mechanism described in this work may be unique to hemichannels and/or to Cx31.3, which shows significant primary sequence divergence from other connexins.

The proposed electrostatic barrier mechanism by the Yeager laboratory has been challenged by studies conducted on human Cx26 and Cx46 hemichannels by the Harris and Contreras laboratories[101,102]. MD studies by these groups predicted Ca^{2+} binding at the pore-lining EC1 domain involving D50, while mutation of D50 or E47 (as well as D51 and/or E48 in Cx46) augmented the Ca^{2+} hemichannel gating properties and significantly reduced Ca^{2+} binding affinity[101,102]. Furthermore, in contrast to the electrostatic mechanism proposed by the Yeager lab, these authors concluded that Ca^{2+} binding does not establish a significant permeation barrier at the site of D50/E47, based on results obtained by cysteine crosslinking accessibility and Cd^{2+} blockade studies[101]. Thus, the authors concluded that channel closure must occur through a different mechanism. Such conclusions are consistent with orthogonal studies on Ca^{2+} regulation of Cx46 hemichannels, which argue that Ca^{2+} binding is coupled to movement of the voltage sensing domain, leading to diminished water permeation[152].

Our work has focused on the native mammalian lens gap junctions, Cx46/50[27,243,245,280]. In the avascular lens, Cx46/50 plays a critical role in maintenance of lens homeostasis and transparency by contributing to a proteinaceous microcirculatory system[13]. Ca^{2+} mishandling is a key factor

associated with age-related cataract formation[18,64,65,68,69], and thus Ca^{2+}-induced closure of Cx46/50 gap junctions may serve an important role in preventing the formation and propagation of light-scattering opacities in the lens. At the same time, genetic mutations that affect the function of Cx46 or Cx50 have been shown to result in cataract formation in mouse models, through mechanisms involving Ca^{2+} accumulation and precipitation[64,65,68].

Here, we describe the structure of native Cx46/50 gap junction channels reconstituted in lipid nanodiscs under conditions of high Ca^{2+} (20 mM). Comparative analysis to our previously described apo-state structures obtained under nearly identical conditions (except for the presence of Ca^{2+}) using single particle cryoEM[243]. The Ca^{2+}-bound structures reveal many novel features that appear to capture components of each of the proposed models of Ca^{2+}-induced gating of gap junctions. These include resolving multiple Ca^{2+}-binding sites localized within the pore, which result in multiple occluded/gated states involving the NT domains that are clearly distinct from the stabilized open-state conformation obtained in the absence of Ca^{2+}. In addition, we find evidence for subunit rearrangements that result in pore collapse, facilitating steric blockade of the permeation pathway by the NT domains, reminiscent of the ‘iris model’ proposed over 40 years ago[133,134,275]. In totality, these structures can reconcile many of the observations made over the last four decades and offer key insights that build on

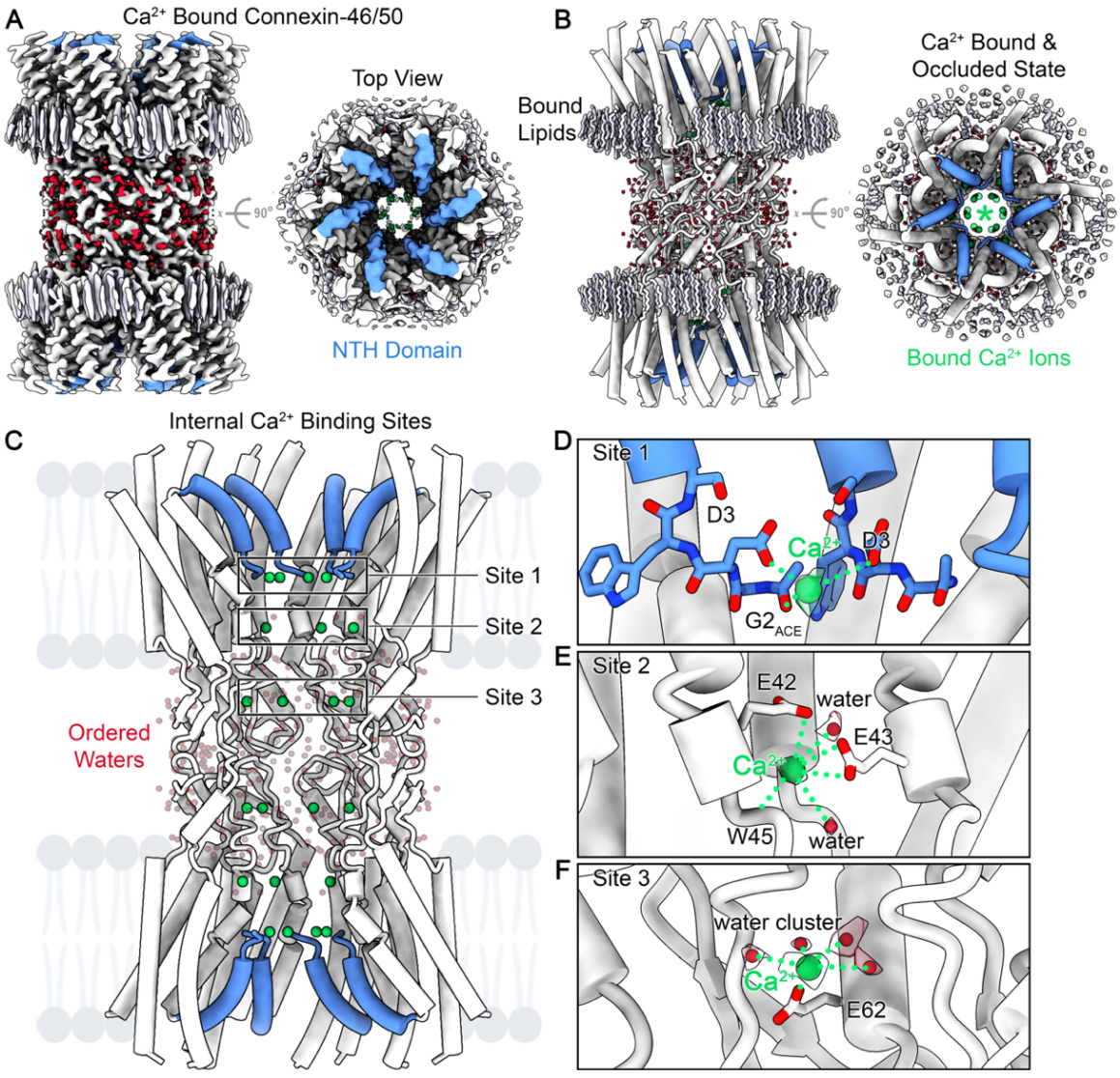

Figure 1 – Overview of Ca^{2+} bound and occluded state of connexin-46/50.

(A) CryoEM reconstruction of Ca^{2+}-bound Cx46/50 gap junctions in lipid nanodiscs. Protein – white; NT domain – blue; waters – red; lipids – light purple; Ca^{2+} ions – green. ***(B)*** Atomic model of Ca^{2+}-bound Cx46/50 in tube representation, colored as in panel A. Asterisk indicates location of bound Ca^{2+} within the pore. ***(C)*** Internal view of panel A, (lipid models omitted for clarity). Each of the twelve connexin subunits binds up to 3 calcium ions (green spheres) within the channel pore (indicated as Sites 1-3). ***(D)*** Zoom view of Ca^{2+}-bound at (putative) Site 1, which involves chelation by neighboring NT domains through negatively charged D3 residues and the carbonyl of acetylated G2. ***(E)*** Zoom view of Ca^{2+} bound at Site 2. The Ca^{2+} is chelated by E42 and the E43 from the parahelix of TM1 in the neighboring subunit. Two stabilized waters and the backbone carbonyl of W45 are also involved. ***(F)*** Zoom view of Ca^{2+} bound at Site 3. Ca^{2+} is chelated at Site 3 by E62 in the EC and a cluster of 4 stabilized water molecules.

the understanding of how Ca^{2+} mishandling in the lens (and other tissues) results in gap junction uncoupling.

Results and Discussion

The Ca^{2+}-bound occluded state of connexin-46/50 in lipid nanodiscs

Native (heteromeric/heterotypic) connexin-46/50 intercellular channels were purified from mammalian lens tissue (young sheep) as previously described[27,243]. Freshly purified channels were reconstituted into self-assembling lipid nanodiscs containing pure dimyristoyl phosphatidylcholine (DMPC) at room temperature (~25°C), stabilized by the membrane scaffold protein MSP1E1[169,243] (see Methods). Reconstituted Cx46/50 was subjected to gel-filtration chromatography under buffering conditions (pH 7.4) identical to those used previously[243]. Lipid-embedded channels were then exchanged into buffer containing the addition of 20 mM $CaCl_2$ by gel-filtration chromatography. The reconstitution yielded a monodisperse population of intercellular channels embedded into a pair of lipid nanodiscs, as assessed by negative stain EM.

Structure determination by high-resolution single particle cryoEM resulted in a high-quality consensus reconstruction, with an overall resolution of 2.1 Å (gold-standard FSC[210,281]) (Fig. 1A). The quality of the cryoEM map allowed for detailed stereochemical structural refinement of both Cx46 and Cx50 (Fig. 1B). In addition to resolved protein structure, there are bouquets of resolved lipid chains at each of the subunit interfaces localized at the extracellular leaflet, as well as 540 resolved water molecules, similar to the previously described apo-state resolved

at 1.9 Å[243] (Fig. 1A,B). As described previously[27,243], the heteromeric pattern(s) of Cx46/50 co-assembly could not be unambiguously resolved (see Methods). Nevertheless, atomic models of both Cx50 and Cx46 isoforms were equally well-fit into the D6-symmetrized cryoEM map, reflecting their close sequence and structural conservation (89% sequence similarity over the structured regions). Given the structural similarity of both isoforms, structural comparisons between the Ca^{2+}-bound and apo-states of Cx46/50 are provided here using Cx46 as the archetype (details regarding Cx50 are provided where appropriate).

Under high Ca^{2+} conditions, Cx46/50 resembles the overall structure and topology of previously described apo-states[27,243] (Fig. 1A). However, clear conformational changes at the NT domains give rise to an occluded pore entrance (detailed description in the following section). Furthermore, in contrast to the single Ca^{2+} binding site resolved for Cx26[105], as many as three Ca^{2+} binding sites are resolved for Cx46/50. All three sites are localized within the pore of the channel (Fig. 1C, Sites 1-3). Perhaps the most surprising site (Site 1) is identified at the proximal end of each of the NT domains (Fig. 1D). This site is also the least well-defined by the cryoEM density and is thus considered to be putatively assigned. The Ca^{2+} ion appears to be chelated by carboxylate sidechains from D3 contributed by two neighboring NT domains, and the carbonyl group of the acetylated G2 position. M1 is posttranslationally cleaved in Cx46 and Cx50, and the resulting n-terminal G2 is acetylated in mammals[49,50,243]. This configuration results in a ring of bound Ca^{2+} ions at the narrowed pore entrance, which appear

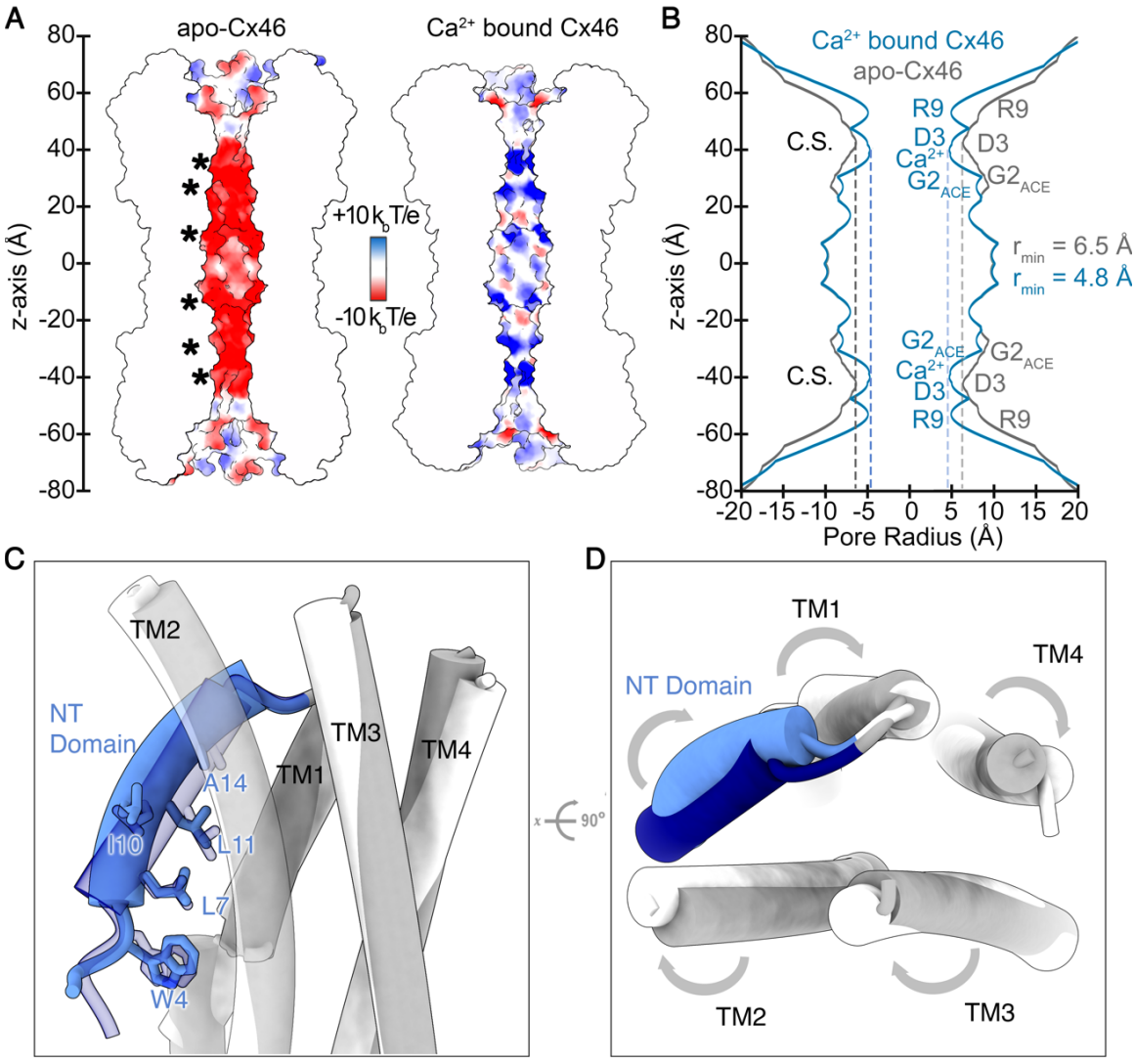

Figure 2 – Ca^{2+} induced changes in electrostatics and conformational state of the permeation pathway.

(A) Coulombic surface representation of connexin-46 in the apo-state (left) and Ca2+ bound state (right). Structures are shown in split-view to visualize the permeation pathway. Positive charge – blue; neutral – white; negative charge – red. Asterisk indicate location of Ca^{2+} binding sites. ***(B)*** Pore profile of apo-Cx46 (grey) versus Ca^{2+} bound Cx46 (blue), calculated with HOLE (Ref. 61). Constrictions of the pore radius are localized to the NT constriction site (C.S.). ***(C)*** Zoom view of conformational changes at the NT domain induced by Ca^{2+}. Hydrophobic anchoring residues are displayed in stick representation. ***(D)*** Diagram illustrating the coordinated rearrangement of the TM domains that accompany movement of the NT domain. In panels C and D, apo-Cx46 is displayed in grey and dark blue. Ca2+-bound Cx46 is displayed in white and light blue.

to stabilize the occluded-state conformation. Notably, D3 is highly conserved among connexin isoforms and plays a key role in voltage-sensing in Cx46 and Cx50[255,282,283], and in other connexins (including Cx26, which contains an equivalent D2 position)[254,284].

In contrast to the putative assignment of Ca^{2+} at Site 1, the other two Ca^{2+} binding sites (Sites 2 and 3) are clearly resolved as unique solvent densities in the cryoEM map, as compared to the apo-state. The Ca^{2+} ion bound at Site 2 is chelated by E42 and E43 of a neighboring subunit, located at the parahelix of TM1, as well as two stabilized waters and backbone carbonyl of W45 (Fig. 1E). Site 2 most closely relates to the site described in the Ca^{2+}-bound state of Cx26 described by X-ray crystallography[105]. In Cx26, Ca^{2+} is bound by residues E47 and E42 (equivalent to E43 in Cx46). The equivalent E48 in Cx46/50 does not directly contribute to Ca^{2+}; however, the proximity of E48 in Cx46/50 is consistent with the previously reported augmentation of Ca^{2+}-binding upon mutation[101]. In Cx50, residue 43 is a phenylalanine (F43), and the equivalent site in other connexins is somewhat variable. In principle, F43 could contribute to Ca^{2+} binding through a canonical cation-pi electron cloud interaction[285]. However, this site in Cx50 appears incapable of adopting a conformation that could satisfy this role and likely does not directly contribute to Ca^{2+} binding. In contrast, the 42 position (or equivalent) is very highly conserved among connexin isoforms as either glutamate or aspartate. A notable exception is in Cx26, which contains a lysine at this site, and may explain the minor differences between these Ca^{2+} binding sites among these structures[105].

Ca^{2+} binding at Site 3 is localized at the EC1 loop and is defined by the sidechain carbonyl of E62 and a cluster of four ordered water molecules (Fig. 1F). This site is unique from previously proposed binding sites in Cx46 and Cx26[101,102]. However, structurally it is near the D51 residue proposed to contribute to Ca^{2+} binding based on functional mutation studies in Cx46[101]. Genetic perturbation at D51 could reasonably affect the local structure and augment Ca^{2+} chelation by E62 and the surrounding water cluster, rationalizing the observed reduction in Ca^{2+} binding by Lopez, *et al*[101]. Notably, the glutamate at position 62 is only conserved in four (out of 20) human connexins (Cx43, Cx45, Cx46, Cx50). It is possible that in connexin hemichannels, D51 plays a more significant role in Cx46/50 and other connexins, as the aspartate in position 51 is conserved in all 20 human connexins.

Ca^{2+} binding induces electrostatic and structural changes within the permeation pathway of Cx46/50

To gain further insight into the mechanistic effects of Ca^{2+} binding, we carried out a detailed structural comparison of the permeation pathways in apo- and Ca^{2+}-bound states of Cx46/50 (Fig. 2). The coulombic potentials along the permeation pathways of Cx46 and Cx50 are largely electronegative, consistent with the appreciable cation-selectivity of these channels[27,280,286–289]. In Cx46, a band of positive charge at the pore entrance is conferred by the arginine at position 9 (R9; N9 in Cx50) in the NT domain. Indeed, this position is one of the key differences between Cx46 and Cx50 responsible for distinguishing channel conductance and permeant selectivity[27,278,280,288,290]. In contrast, when bound to Ca^{2+}, the coulombic

potential of the permeation pathway in Cx46/50 becomes almost completely electropositive (Fig. 2A). Such an environment would be unfavorable to permeation to Na^+ ions, the major permeant in the eye lens[13,291].

In the apo-state, the major constriction site (C.S.) in Cx46/50 is defined by the distal end of the NT domains (r_{min} = 6.5 Å) as determined by pore-profile analysis with HOLE[27,230,280] (Fig. 2B, grey trace, regions +/- 30-60 Å along the z-axis). Ca^{2+} binding at Site 1, combined with the induced conformational changes in the NT domains result in a more occluded C.S. (r_{min} = 4.8 Å) Fig. 2B, blue trace). The conformational changes within the NT domain result in a re-orientation with

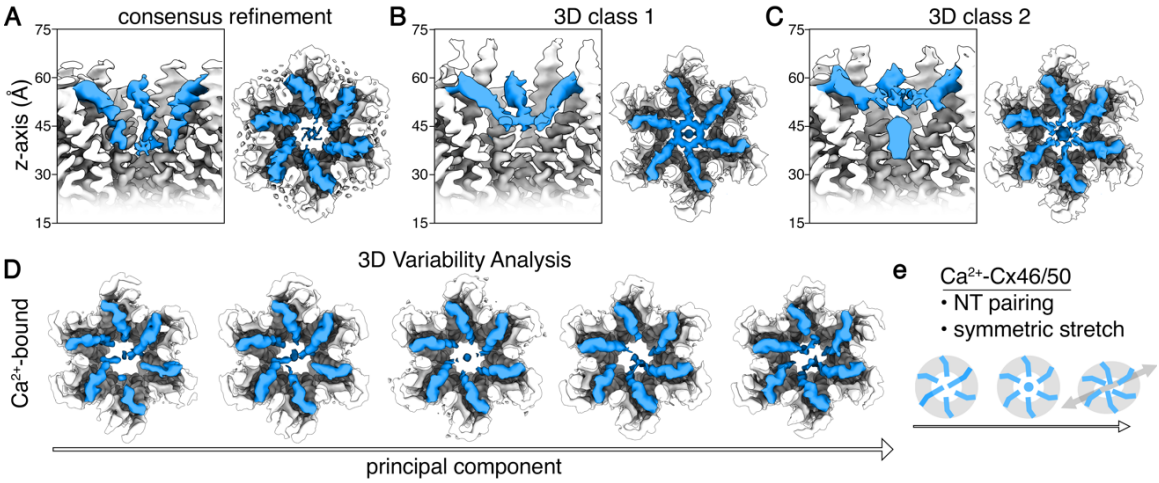

Figure 3 – Ca^{2+} binding results in multiple closed states and pore collapse of connexin-46/50 channels.

(A) Split view (left) and top view (right) showing the NT domain conformation of Cx46/50 obtained by consensus refinement of the cryoEM dataset with D6 symmetry. ***(B** and **C)*** Additional discrete states of the NT domain obtained by 3D classification (class 1, panel B) and (class 2, panel C) obtained with D6 symmetry. Both classes show unique NT orientations that obstruct the pore vestibule. ***(D)*** Asymmetric principal component analysis reveals 3D variability within the NT domain and symmetric stretching of the pore. Pore occlusion by the NT domains appears to involve paired interactions involving neighboring and opposing subunits. The stretching mode results in pore collapse, accompanied by close contact of NT domains from opposing subunits.

respect to the TM helices and remodeling of the conserved hydrophobic residues that anchor the amphipathic helix to the pore vestibule in the previously described stabilized-open state conformation[27,243] (Fig. 2C).

Rearrangements at the NT domain coincide with subtle reorganization of the TM helices (TM1-4) (Fig. 2D). TM1 (which is directly connected to the NT) moves away from the center of the channel toward TM4. This is further associated with a more dramatic movement of TM2 toward the pore, with more modest re-arrangements of TM3/4 to maintain TM packing interactions. Overall, these concerted movements can be described as an overall rotation of TM helices in a clockwise direction, when looking down from the cytoplasmic view of the channel (Fig. 2D). This rearrangement draws the distal region of the NT back, away from the center of the channel, while the forward movement of TM2 buttress this region of the NT and appears to further stabilizes the occluded conformation.

Ca^{2+} gating involves NT-domain closure and pore collapse

The conformational rearrangements at the NT domains observed in the presence of Ca^{2+} appear to occlude the pore pathway of Cx46/50, as compared to the apo-state (Fig. 2). However, the resulting pore diameter (~9.6 Å) would still be large enough to permit permeation of solvated ions, and thus ionic currents may not be completely inhibited as expected. Notably, the NT domains display significantly lower local resolution as compared to the TM and EC domains, consistent with conformational heterogeneity and/or local disorder (Fig. 3A). In an attempt to resolve this heterogeneity, 3D classification methods in RELION-3.1[207,209] were

applied, which resolved additional discrete conformational states that were distinguishable by features localized to the NT regions of the channel (Fig. 3B,C). While local resolution of the NT domains obtained in these classes were not suitable for atomic modeling, they display distinct differences from the consensus refinement and clear indications of complete pore closure. Notably, similar approaches using various applied symmetries or without applied symmetry did not result in a significant improvement in resolvable features for these states.

In one of these classes (class 1), the NT domains adopt a slightly more lifted conformation as compared to the consensus cryoEM map and appears to be

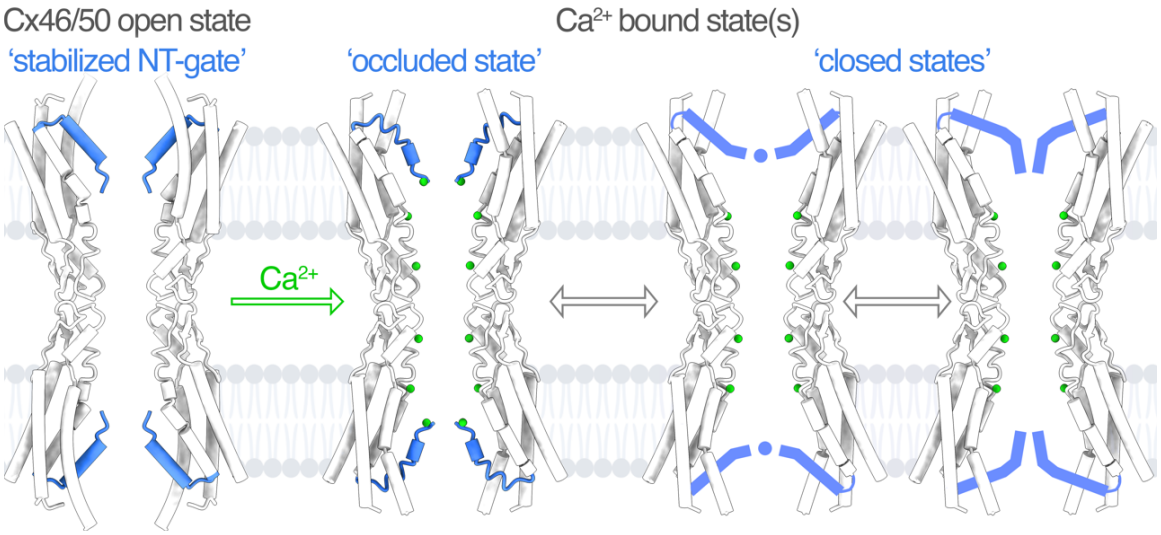

Figure 4 – Overview of Ca^{2+} induced gating in connexin-46/50 gap junction channels.
In the apo-state, Cx46/50 channels reside in an open state, characterized by the stabilized conformation of the NT domains (blue). Under high calcium conditions, Ca^{2+} ions (green) may bind at up to 3 sites located at each of the twelve subunits. These interactions induce conformational changes in the NT domains, resulting in a variety of occluded and/or closed state conformations expected to impede or completely block the permeation of ionic currents and other molecular substates. Close contact between NT domains may be supported by subunit rearrangements that collapse the pore architecture, enabling steric block of the permeation pathway.

completely detached from TM1/2 (Fig. 3B). The proximal ends of the NT domains form a continuous density of interaction and display a plug-like feature at the center of the channel pore. In another class (class 2), the distal region of the NT is even more lifted, to almost 90° with respect to the pore axis, while the proximal regions of the NT interact deeper into the pore and form a prominent central plug (Fig. 3C). In both classes, the conformational state(s) adopted by the NT would be expected to completely abrogate permeation of solvated ions.

The limited resolution within the NT domains displayed in the 3D classes representing closed-states of the channel (Fig. 3B,C) are consistent with the lack of interaction of these domains with the pore lumen and overall conformational heterogeneity induced by Ca^{2+} binding. To gain further insight into continuum dynamics of the NT, a symmetry-expanded particle stack was generated for 3D variability analysis in cryoSPARC[292].

This approach revealed a particularly notable principal component describing the continuous dynamics of the NT domains and displayed a break in overall D6 symmetry of the channels (Fig. 3D,E). At one end of the principal component, the NT domains adopt paired interactions involving two sets of neighboring subunits and a pair of opposing subunits that cross the pathway of the channel, effectively occluding the pore (Fig. 3D, left). Along the trajectory of this principal component, the NT domains transition through a symmetric arrangement that most closely resembles the consensus refinement obtained from RELION (compare Fig. 3D, center to Fig. 3A). At the end of this principal component, the two sets of paired NT domains come into close contact to occlude the pore, while

the other two NT domains become more retracted toward the channel lumen (Fig. 3D, right). Concomitant with these changes in NT domain conformations is an overall stretching of the channel architecture, facilitated by subunit rearrangements that deform the shape of the channel pore. In this way, the pore effectively collapses, enabling NT domain interactions between opposing subunits and occlusion of the permeation pathway (Fig. 3E). 3D variability analysis applied to the apo-state Cx46/50 cryoEM dataset did not reveal similar features of NT dynamics or modes of channel stretching, suggesting that the observed conformational dynamics are a direct consequence of Ca^{2+} binding, and likely play a fundamental role in the mechanism of channel inhibition.

Conclusions

This study provides first concrete evidence that the NT domain of gap junctions is directly involved in Ca^{2+} gating (Fig. 4). Remarkably, the structural features identified in Cx46/50 appear to capture key features of Ca^{2+} gating models previously proposed for other connexins, while also resolving many discrepancies that have stymied our understanding of this mechanism. The site 2 Ca^{2+} binding site observed in Cx46/50 is consistent with the Ca^{2+} site resolved in Cx26[105], as is the dramatic change in coulombic potential within the pore that occurs as a result. The NT of Cx26 appears to be inherently less stable as compared to Cx46/50 and is either unresolved or poorly resolved in X-ray and cryoEM structures of Cx26[25,105,141,277,293]. The inherent instability of the Cx26 NT has precluded a mechanistic understanding its role in channel gating. However, the ability of the

NT to form a gate in Cx26 is supported by early electron crystallographic studies[141,277] and a recent report that examined the structural mechanism of pH regulation[293]. Indeed, the role of the NT domain as the physical gate in response to Ca^{2+} is also consistent with the pore-accessibility studies on hemichannels of Cx26 and Cx46 by Lopez, *et al*[101]. Remarkably, deformation of the channel also appears to contribute to the Ca^{2+} gating mechanism in Cx46/50, resulting in pore collapse and facilitating close contact between opposing NT domains. This feature is profoundly reminiscent of the 'iris model' of channel gating originally proposed by Zampighi, Unwin, and Ennis over 40 years ago[133,134,275].

Gaining a clear mechanistic picture of the Ca^{2+} gating response in the gap junctions is an important step toward understanding how cells protect themselves from localized stress/trauma. Without a regulatory mechanism to uncouple cells in response to Ca^{2+}, cell death signals could propagate via gap junctions to healthy cells, resulting in catastrophic cell death across entire tissues (a.k.a. the "bystander effect" or the "kiss of death")[294,295]. In the eye lens, Ca^{2+} induced closure of Cx46/50 may provide an important protective mechanism to isolate healthy tissue from propagation of cataractogenesis. Likewise, this protective mechanism is expected to play an important role in isolating tissue damage under conditions of calcium overload associated with heart attack and stroke. The potential for pharmacological control over this mechanism may yield a promising therapeutic approach to treating these conditions, as well as other connexinopathies.

Methods

MSP expression and purification

A bacterial expression plasmid encoding MSP1E1 was obtained from Addgene[169]. MSP1E1 was expressed and purified as described[170,243]. Protein concentration was determined by UV absorbance at 280 nm. Flash-frozen aliquots were stored at –80°C for up to 18 months.

Cx46/50 purification and nanodisc reconstitution

Native Cx46/50 intercellular channels were isolated from ovine lens fiber cells[27,243]. Lamb eyes obtained from Wolverine Packers slaughterhouse (Detroit, MI) were dissected and fully intact lenses were stored at –80°C. Gap junctions were isolated from lens cores, which are enriched in the c-terminal truncation variant of Cx46/50 (a.k.a. MP38)[37,38,45,121]. Details of the purification procedure are provided below.

Lenses were thawed from -80°C and core tissue was dissected from cortex with a surgical blade. Stripped membranes were prepared as described[201–203]. Protein concentration was determined by BCA (Pierce) and membranes were stored at –80°C in Storage Buffer (10 mM Tris [pH 8.0], 2 mM EDTA, 2 mM EGTA) at ~2 mg mL^{-1} protein. Stripped membranes were solubilized with Storage Buffer with 20 mg mL^{-1} n-decyl-β-D-maltoside (DM; Anatrace) for 30 minutes at 37°C with gentle agitation. Insoluble material was cleared by ultracentrifugation at ~150,000 x *g* for 30 minutes at 4°C. Filtered supernatant (Millipore; 0.22 μm) was separated by ion-exchange chromatography (UnoQ, BioRad) with Buffer A (Storage Buffer with 3 mg mL^{-1} DM). Protein was eluted with a 25 CV gradient of Buffer B (Buffer A with 500 mM NaCl), ending with 50% Buffer B. Peak Cx46/50 fractions (confirmed by SDS-PAGE) were pooled and separated by size exclusion

chromatography (SEC; Superose 6 Increase 10/300 GL; GE Healthcare) with SEC buffer (20 mM HEPES [pH 7.4], 150 mM NaCl, 2 mM EDTA, 2 mM EGTA and 3 mg mL^{-1} DM). Peak fractions were pooled and concentrated to ~5 mg mL^{-1} (Vivaspin 6; 50-kDa MWCO; Sartorius). Protein concentration was measured by UV_{280} absorbance.

Freshly purified Cx46/50 was reconstituted into MSP1E1 nanodiscs with dimyristoyl phosphatidylcholine (DMPC; Avanti), following established procedures[170,204,243]. DMPC in chloroform was dried under N_2 gas and left under vacuum overnight to remove residual solvent. DMPC thin films were resuspended in 50 mg mL^{-1} DM and sonicated at 37°C for 2 hours. DMPC and freshly purified Cx46/50 were combined at a 0.6:90 molar ratio (33.3 μm Cx46/50, 4 mM DMPC). Cx46/50 with DMPC was gently pipetted to mix and incubated at 25°C with gentle agitation for 2 hours. Purified MSP1E1 was added for a final molar ratio of 0.6:1:90 (Cx46/50:MSP1E1:lipids), and the reconstitution mixture was incubated at 25°C for 30 minutes. DM was removed with Bio-Beads SM-2 resin (BioRad) at a ratio of 20:1 beads:detergent (wt wt^{-1}) by overnight (12-16 hours) incubation at 25°C with gentle agitation. Bio-Beads by making a single perforation to the top and bottom of the Eppendorf tube with a hot needle. The perforated tube was gently centrifuged (~500 x *g*) into a new tube with fresh Bio-Beads (20:1 wt wt^{-1}) and incubated for a final 2 hours at 25°C. After removing the 2nd Bio-Bead batch, samples were ultracentrifuged at ~150,000 x *g* for 15 minutes at 4°C to remove insoluble material. Filtered supernatant (Millipore; 0.22 μm) was separated by SEC

(Superose 6 Increase 10/300 GL; GE Healthcare) with SEC Buffer plus 20 mM Ca^{2+} to exchange the Cx46/50 nanodiscs into a high-Ca^{2+} environment and to remove empty nanodiscs. Peak Cx46/50-nanodiscs in 20 mM Ca^{2+} (confirmed by SDS-PAGE) were pooled and concentrated (Vivaspin 6; 50-kDa cut-off filter; Sartorius) to a final concentration ~2.5 mg mL^{-1} (confirmed by UV_{280} absorbance). All chromatography steps were performed by FPLC at 4°C.

CryoEM specimen preparation and data collection

Cx46/50-nanodiscs in 20 mM Ca^{2+} were prepared for cryoEM by applying 5 μl Cx46/50-nanodiscs (~2.1 mg mL^{-1}) to a glow-discharged holey carbon grid (Quantifoil R 2/1, 400 mesh) for 8.0 seconds. The grid was blotted for 5.0 seconds (3.0 seconds dwell time) and plunge frozen in liquid ethane (Vitrobot Mark IV; Thermo Fisher Scientific) at 100% humidity and stored under liquid nitrogen.

Vitrified Cx46/50 nanodiscs in 20 mM Ca^{2+} were imaged on a Titan Krios (Thermo Fisher Scientific) operated at 300 kV. Dose-fractionated image stacks were recorded on a K3 Direct Electron Detector (Thermo Fisher Scientific) at 120,000x nominal magnification in super-resolution mode with a physical pixel size of 0.830 Å $pixel^{-1}$ (0.415 Å $pixel^{-1}$ super-resolution). The nominal dose rate was 0.49 e^{-} $Å^{-2}$ sec^{-1} with a nominal exposure dose of ~37 e^{-} $Å^{-2}$. A dataset of 5,750 movies was obtained with nominal defocus values ranging from 0.5-1.5 μm. Data collection parameters were controlled in an automated manner with serialEM[262].

CryoEM image processing for Cx46/50-lipid nanodiscs in 20 mM Ca^{2+}

Beam-induced motion for the entire dataset was corrected with MotionCor2[263] and contrast transfer function (CTF) estimation was done with Gctf[208]. Micrographs with CTF models worse than 5 Å resolution were discarded and the remaining 5,478 micrographs were used for subsequent processing steps. The blob-picker in cryoSPARC (Structura Biotechnology; v2.15.0)[264] was used to pick an initial set of 5,101,050 particles. 2D classification was used to generate a cleaned particle stack (374,002) for *ab initio* reconstruction in cryoSPARC. Homogeneous refinement (D6 symmetry applied) of the top two *ab inito* models yielded a map at 3.24 Å (208-pixel box, 1.596 Å pix^{-1}). A 20 Å lowpass-filter was applied to the result from homogeneous refinement and 30 uniquely spaced projections were used for template picking in cryoSPARC to generate 8,263,040 template-based picks. Three rounds of heterogeneous refinement (without symmetry) and duplicate particle removal (75 Å minimum separation distance) yielded a refined set of 488,423 particles that refined to 2.38 Å resolution after non-uniform refinement[265] in cryoSPARC (256-pixel box, 1.167 Å pix^{-1}).

One round of heterogeneous refinement in cryoSPARC (D6 symmetry applied) and particle de-duplication (100 Å minimum separation distance) culled the particle set to 308,534. Local motion correction followed by another round of non-uniform refinement yielded a consensus reconstruction at 2.06 Å resolution (288-pixel box, 0.865 Å pix^{-1}) (Fig. 1A, 3A). This refined particle stack was used for 3D variability analysis in cryoSPARC[292] (Fig. 3D). At this stage, the particle stack was also converted from cryoSPARC to RELION format with UCSF PyEM (v.0.5)[266] for subsequent processing.

Bayesian polishing and CTF refinement (per-particle defocus, per-micrograph astigmatism, beam-tilt refinement, 3rd order aberration correction, 4th order aberration correction) followed by 3D auto-refine in RELION-3.1[207,209] yielded a 2.12 Å resolution map (224-pixel box, 0.949 Å pix^{-1}). An initial atomic model was fit into the unsharpened map from 3D auto-refine (see Atomic modelling, refinement, and validation below) and an 8 Å-resolution map was simulated from the atomic model using the molmap tool in UCSF ChimeraX[212]. A solvent mask derived from the molmap (0.4 initial threshold, 5-pixel extension, 5-pixel soft edge) was applied during 3D classification without alignment (D6 symmetry, 10 Å initial lowpass filter, k=10, T=16, limit resolution to 5 Å) in RELION. After 500 iterations, five of the ten classes (86,465 particles) resembled the NT conformation observed in the consensus refinement obtained from cryoSPARC (Fig. 1A, 3A). Three of the ten classes (29,633 particles) featured a significantly "lifted" NT domain. These particles were subjected to a final round of 3D classification without alignment (D6 symmetry, 6 Å initial lowpass filter, k=6, T=8, no resolution limit). After 300 iterations, one of the six classes featured (16,463 particles) featured a "lifted" NT domain (Fig. 3B; Class 1). Four classes (7,705 particles) featured a lifted NT domain distinct from "Class 1" (Fig. 3C; Class 2). "Class 1" particles were refined to 2.56 Å resolution in RELION (density shown in Fig. 3B). "Class 2" particles were refined to 2.95 Å resolution in RELION (density shown in Fig. 3C). Postprocessing and local resolution estimation was performed in RELION and local resolution-filtered maps were generated for atomic model refinement.

Atomic modelling, refinement, and validation

Initial atomic models of Cx46 (7JKC) and Cx50 (7JJP) were fit as rigid bodies into the 2.06 Å-resolution consensus refinement obtained in cryoSPARC (Fig. 1B, C, D, E, F). After deletion of lipid acyl chains and solvent, all-atom models for Cx46 and Cx50 were subjected to several iterations of manual adjustment with COOT[213] followed by real-space refinement in PHENIX[214] with secondary structure and non-crystallographic symmetry (D6) restraints applied. Model quality was monitored at each iteration with MolProbity[215]. Coordinate and restraint files for DMPC (PDBe Ligand Code: MC3) and were generated with PHENIX eLBOW[217]. DMPC ligands were manually fit into the cryoEM density with COOT. Atoms in DMPC that could not be accommodated by the density were deleted. Several iterations of real-space refinement on the entire model were completed until refinement statistics converged.

Chapter 5: The post-resolution revolution era of cryoEM applied to gap junction structural biology

Authors: Jonathan A. Flores[1] and Steve L. Reichow[1,2]

Affiliations:

[1] Department of Chemical Physiology and Biochemistry, Oregon Health and Science University, Portland OR 97239, U.S.A.

[2] Department of Chemistry, Portland State University, Portland OR 97201, U.S.A.

Respective Contributions

J.A.F and S.L.R. contributed to manuscript preparation.

S.L.R. provided overall guidance to the design and execution of manuscript preparation.

This is an unpublished manuscript in preparation

A 70-year journey for gap junction structure begins and ends at the electron microscope

A dialogue on the structure and function of junctional membranes began in the 1950s with electron microscope (EM) imaging of heavy metal-stained sections

cardiac and liver tissue. A common thread in these images were juxtaposed cell membranes separated by a protein-dense 3 nm gap[296–299]. Over two decades passed before Caspar, *et al* and Makowski, *et al* correlated EM images with x-ray diffraction (XRD) of the hexagonal arrays found in liver junctional membranes. The quasi-crystalline array composed of "connexons" (connexin hemichannels) were ~20 Å wide (membrane plane) and ~150 Å long junctions (membrane orthogonal), with a central pore ~16 Å across. The 1980s saw a slew of two-dimensional crystallography (2DX) efforts spearheaded largely by Unwin, Zampighi, Ennis, *et al*[133,134,275,300,301]. These efforts would yield maps in the ~20 Å resolution range of hepatocyte gap junctions, enabling visualization of "open" and "closed" states, proposed to be facilitated by a coordinated rearrangement connexin subunits.

Despite the propensity for gap junctions to coalesce into 2D crystals, disorder in the lattice stymied efforts to obtain high-resolution details. 15 years after the 2DX structures from Unwin, *et al*, Mark Yeager's group presented improved 2DX diffraction using recombinant Cx43 with a c-terminal truncation that improved crystal order[135,136,138]. The structures (resolved to ~6-7 Å in the membrane plane) showed a 24-transmembrane domain architecture in each membrane, demonstrating that gap junctions are dodecameric assemblies with six connexins in each hemichannel.

Another decade would pass until a return to XRD in 2009, applied to three-dimensional (3D) crystals of recombinant protein isolated in detergent, yielded a high-resolution breakthrough from Maeda, *et al*[25]. The crystal structure of human Cx26 resolved to 3.4 Å finally gave a detailed look at the intermolecular interactions

stabilizing the dodecameric channel architecture and provided a model for the n-terminal helix (NTH), which was suspected to be involved in channel gating.

Advancements in direct electron detection and beam-induced motion correction[155,302–305], automated data collection routines[262,306–309], and image processing algorithms[154,158,208,263,264,310–313] paved a road that led to the first gap junction structure by single-particle cryoEM[27]. The 3.5 Å resolution structure of native lens Cx46/50 from Myers, *et al* added gap junctions to the growing resolution revolution[156,157,314] guest list. Beyond illuminating mechanisms of perm-selectivity and a new open-state conformation, Myers, *et al* demonstrated that advances in cryoEM technology could now be harnessed to resolve gap junctions with enough detail to answer decades-old questions about their structure and function[315–317]. In a turn of events reminiscent of the ouroboros, our current understanding of gap junction structure has both commenced and arrived at the electron microscope.

The next cryoEM resolution revolution: breaking the 2 Å resolution barrier for optimal structure-based drug design

Chapter 2 of this thesis describes the cryoEM workflow—from tissues to atomic models—of native lens Cx46/50 in a double-lipid bilayer. Single-particle reconstructions of Cx46/50 surpassed the 2 Å resolution barrier—a highly sought-after benchmark for basic science and the pharmaceutical industry alike. This was an important achievement not least of all because for structure-based drug design (SBDD), it is generally considered that to design selective, high-affinity small

molecules for a druggable target, visualization of target-ligand interactions should be *at least* 2.5 Å to facilitate accurate stereochemical refinement and placement of critical solvent molecules[318,319]. Moreover, it has long been a cliché that high-resolution membrane protein structures are highly underrepresented in the Protein Data Bank: as of February 2022, ≤3 Å resolution membrane protein structures make up ~1.5 % of PDB entries; this figure drops to ~0.7 % ≤2.5 Å structures[320].

The observation that Cx46/50 can surpass the resolution benchmarks required for detailed mechanistic insights gives reason for optimism about the future of gap junction structural biology and membrane protein cryoEM. Indeed, as illustrated in chapters 3 & 4, Cx46/50 is an amenable, model system that can be used to address questions about how gap junction channels respond to regulatory signals, how disease-causing mutants give rise to aberrant channel function, and potentially leveraged for future SBDD efforts.

High-resolution *in situ* structures by cryo-electron tomography will be indispensable

While single-particle cryoEM has carved out a massive role for present gap junction structural investigations, one caveat still remains: proteins do not natively function as isolated, single particles. Rather, high-resolution *in situ* structures of gap junctions in the native cell membrane environment remain highly sought after.

For instance, because gap junctions natively assemble into plaques consisting of 1000s of individual channels, the native structure and function of gap junction channels within these plaque formations would answer countless

questions about how their structural behavior is affected by high-order assembly, and how models for cooperativity in channel gating might be evaluated with high-resolution imaging of plaque responses to regulatory signals in the cell. While *in situ* structural investigations by cryoET have yet to reveal detailed mechanistic insights into gap junction biology, based on the recent and rapid advances of that are occurring with this technique[321–323], cryoEM will surely continue to serve an important role for gap junction structural biology in the future.

References

1. Sue Menko, A. Lens epithelial cell differentiation. *Exp. Eye Res.* **75**, 485–490 (2002).
2. Bassnett, S. On the mechanism of organelle degradation in the vertebrate lens. *Exp. Eye Res.* **88**, 133–139 (2009).
3. Lynnerup, N., Kjeldsen, H., Heegaard, S., Jacobsen, C. & Heinemeier, J. Radiocarbon dating of the human eye lens crystallines reveal proteins without carbon turnover throughout life. *PloS One* **3**, e1529 (2008).
4. Rowan, S., Chang, M.-L., Reznikov, N. & Taylor, A. Disassembly of the lens fiber cell nucleus to create a clear lens: The p27 descent. *Exp. Eye Res.* **156**, 72–78 (2017).
5. Wride, M. A. Lens fibre cell differentiation and organelle loss: many paths lead to clarity. *Philos. Trans. R. Soc. Lond. B. Biol. Sci.* **366**, 1219–1233 (2011).
6. Truscott, R. J. W. Are ancient proteins responsible for the age-related decline in health and fitness? *Rejuvenation Res.* **13**, 83–89 (2010).
7. Schey, K. L., Wang, Z., Friedrich, M. G., Garland, D. L. & Truscott, R. J. W. Spatiotemporal changes in the human lens proteome: Critical insights into long-lived proteins. *Prog. Retin. Eye Res.* **76**, 100802 (2020).
8. Truscott, R. J. W. Age-related nuclear cataract-oxidation is the key. *Exp. Eye Res.* **80**, 709–725 (2005).

9. Michael, R. & Bron, A. J. The ageing lens and cataract: a model of normal and pathological ageing. *Philos. Trans. R. Soc. Lond. B. Biol. Sci.* **366**, 1278–1292 (2011).
10. Truscott, R. J. W. & Friedrich, M. G. The etiology of human age-related cataract. Proteins don't last forever. *Biochim. Biophys. Acta* **1860**, 192–198 (2016).
11. Khairallah, M. *et al.* Number of People Blind or Visually Impaired by Cataract Worldwide and in World Regions, 1990 to 2010. *Invest. Ophthalmol. Vis. Sci.* **56**, 6762–6769 (2015).
12. Trayhurn, P. & Van Heyningen, R. The role of respiration in the energy metabolism of the bovine lens. *Biochem. J.* **129**, 507–509 (1972).
13. Mathias, R. T., Kistler, J. & Donaldson, P. The lens circulation. *J. Membr. Biol.* **216**, 1–16 (2007).
14. Zhu, Y., Xu, S., Eisenberg, R. S. & Huang, H. A Bidomain Model for Lens Microcirculation. *Biophys. J.* **116**, 1171–1184 (2019).
15. Baldo, G. J. & Mathias, R. T. Spatial variations in membrane properties in the intact rat lens. *Biophys. J.* **63**, 518–529 (1992).
16. Delamere, N. A. & Dean, W. L. Distribution of lens sodium-potassium-adenosine triphosphatase. *Invest. Ophthalmol. Vis. Sci.* **34**, 2159–2163 (1993).
17. Mathias, R. T., Rae, J. L. & Baldo, G. J. Physiological properties of the normal lens. *Physiol. Rev.* **77**, 21–50 (1997).

18. Gao, J. *et al.* Connections between connexins, calcium, and cataracts in the lens. *J. Gen. Physiol.* **124**, 289–300 (2004).
19. Bagur, R. & Hajnóczky, G. Intracellular Ca2+ Sensing: Its Role in Calcium Homeostasis and Signaling. *Mol. Cell* **66**, 780–788 (2017).
20. Borchman, D., Paterson, C. A. & Delamere, N. A. Ca2+-ATPase activity in the human lens. *Curr. Eye Res.* **8**, 1049–1054 (1989).
21. Tamiya, S. & Delamere, N. A. The influence of sodium-calcium exchange inhibitors on rabbit lens ion balance and transparency. *Exp. Eye Res.* **83**, 1089–1095 (2006).
22. Mathias, R. T., White, T. W. & Gong, X. Lens gap junctions in growth, differentiation, and homeostasis. *Physiol. Rev.* **90**, 179–206 (2010).
23. Truscott, R. J. W. & Friedrich, M. G. Molecular Processes Implicated in Human Age-Related Nuclear Cataract. *Invest. Ophthalmol. Vis. Sci.* **60**, 5007–5021 (2019).
24. Söhl, G. & Willecke, K. Gap junctions and the connexin protein family. *Cardiovasc. Res.* **62**, 228–232 (2004).
25. Maeda, S. *et al.* Structure of the connexin 26 gap junction channel at 3.5 A resolution. *Nature* **458**, 597–602 (2009).
26. Grosely, R. & Sorgen, P. L. A history of gap junction structure: hexagonal arrays to atomic resolution. *Cell Commun. Adhes.* **20**, 11–20 (2013).
27. Myers, J. B. *et al.* Structure of native lens connexin 46/50 intercellular channels by cryo-EM. *Nature* **564**, 372–377 (2018).

28. Oshima, A. Structure and closure of connexin gap junction channels. *FEBS Lett.* **588**, 1230–1237 (2014).
29. Musil, L. S. & Goodenough, D. A. Multisubunit assembly of an integral plasma membrane channel protein, gap junction connexin43, occurs after exit from the ER. *Cell* **74**, 1065–1077 (1993).
30. Koval, M. Pathways and control of connexin oligomerization. *Trends Cell Biol.* **16**, 159–166 (2006).
31. Takeuchi, H. *et al.* Tumor necrosis factor-alpha induces neurotoxicity via glutamate release from hemichannels of activated microglia in an autocrine manner. *J. Biol. Chem.* **281**, 21362–21368 (2006).
32. Anselmi, F. *et al.* ATP release through connexin hemichannels and gap junction transfer of second messengers propagate Ca2+ signals across the inner ear. *Proc. Natl. Acad. Sci. U. S. A.* **105**, 18770–18775 (2008).
33. Ebihara, L., Korzyukov, Y., Kothari, S. & Tong, J.-J. Cx46 hemichannels contribute to the sodium leak conductance in lens fiber cells. *Am. J. Physiol. Cell Physiol.* **306**, C506-513 (2014).
34. Bai, D., Yue, B. & Aoyama, H. Crucial motifs and residues in the extracellular loops influence the formation and specificity of connexin docking. *Biochim. Biophys. Acta Biomembr.* **1860**, 9–21 (2018).
35. Revel, J. P. & Karnovsky, M. J. Hexagonal array of subunits in intercellular junctions of the mouse heart and liver. *J. Cell Biol.* **33**, C7–C12 (1967).

36. McNutt, N. S. & Weinstein, R. S. The ultrastructure of the nexus. A correlated thin-section and freeze-cleave study. *J. Cell Biol.* **47**, 666–688 (1970).

37. White, T. W., Bruzzone, R., Goodenough, D. A. & Paul, D. L. Mouse Cx50, a functional member of the connexin family of gap junction proteins, is the lens fiber protein MP70. *Mol. Biol. Cell* **3**, 711–720 (1992).

38. Paul, D. L., Ebihara, L., Takemoto, L. J., Swenson, K. I. & Goodenough, D. A. Connexin46, a novel lens gap junction protein, induces voltage-gated currents in nonjunctional plasma membrane of Xenopus oocytes. *J. Cell Biol.* **115**, 1077–1089 (1991).

39. Jiang, J. X. & Goodenough, D. A. Heteromeric connexons in lens gap junction channels. *Proc. Natl. Acad. Sci. U. S. A.* **93**, 1287–1291 (1996).

40. Koval, M., Molina, S. A. & Burt, J. M. Mix and match: investigating heteromeric and heterotypic gap junction channels in model systems and native tissues. *FEBS Lett.* **588**, 1193–1204 (2014).

41. Zhong, G. *et al.* Mono-Heteromeric Configurations of Gap Junction Channels Formed by Connexin43 and Connexin45 Reduce Unitary Conductance and Determine both Voltage Gating and Metabolic Flux Asymmetry. *Front. Physiol.* **8**, 346 (2017).

42. Richter, G. M. *et al.* Risk factors for cortical, nuclear, posterior subcapsular, and mixed lens opacities: the Los Angeles Latino Eye Study. *Ophthalmology* **119**, 547–554 (2012).

43. Hashemi, H. *et al.* Global and regional prevalence of age-related cataract: a comprehensive systematic review and meta-analysis. *Eye Lond. Engl.* **34**, 1357–1370 (2020).

44. Gruijters, W. T., Kistler, J., Bullivant, S. & Goodenough, D. A. Immunolocalization of MP70 in lens fiber 16-17-nm intercellular junctions. *J. Cell Biol.* **104**, 565–572 (1987).

45. Kistler, J., Schaller, J. & Sigrist, H. MP38 contains the membrane-embedded domain of the lens fiber gap junction protein MP70. *J. Biol. Chem.* **265**, 13357–13361 (1990).

46. Lin, J. S. *et al.* Processing of the gap junction protein connexin50 in the ocular lens is accomplished by calpain. *Eur. J. Cell Biol.* **73**, 141–149 (1997).

47. Yin, X., Gu, S. & Jiang, J. X. The development-associated cleavage of lens connexin 45.6 by caspase-3-like protease is regulated by casein kinase II-mediated phosphorylation. *J. Biol. Chem.* **276**, 34567–34572 (2001).

48. Slavi, N., Wang, Z., Harvey, L., Schey, K. L. & Srinivas, M. Identification and Functional Assessment of Age-Dependent Truncations to Cx46 and Cx50 in the Human Lens. *Invest. Ophthalmol. Vis. Sci.* **57**, 5714–5722 (2016).

49. Shearer, D., Ens, W., Standing, K. & Valdimarsson, G. Posttranslational modifications in lens fiber connexins identified by off-line-HPLC MALDI-quadrupole time-of-flight mass spectrometry. *Invest. Ophthalmol. Vis. Sci.* **49**, 1553–1562 (2008).

50. Wang, Z. & Schey, K. L. Phosphorylation and truncation sites of bovine lens connexin 46 and connexin 50. *Exp. Eye Res.* **89**, 898–904 (2009).
51. Wang, Z., Han, J., David, L. L. & Schey, K. L. Proteomics and phosphoproteomics analysis of human lens fiber cell membranes. *Invest. Ophthalmol. Vis. Sci.* **54**, 1135–1143 (2013).
52. Berthoud, V. M., Westphale, E. M., Grigoryeva, A. & Beyer, E. C. PKC isoenzymes in the chicken lens and TPA-induced effects on intercellular communication. *Invest. Ophthalmol. Vis. Sci.* **41**, 850–858 (2000).
53. Yin, X., Jedrzejewski, P. T. & Jiang, J. X. Casein kinase II phosphorylates lens connexin 45.6 and is involved in its degradation. *J. Biol. Chem.* **275**, 6850–6856 (2000).
54. Lin, D., Lobell, S., Jewell, A. & Takemoto, D. J. Differential phosphorylation of connexin46 and connexin50 by H2O2 activation of protein kinase Cgamma. *Mol. Vis.* **10**, 688–695 (2004).
55. Zampighi, G. A., Planells, A. M., Lin, D. & Takemoto, D. Regulation of lens cell-to-cell communication by activation of PKCgamma and disassembly of Cx50 channels. *Invest. Ophthalmol. Vis. Sci.* **46**, 3247–3255 (2005).
56. Yin, X., Liu, J. & Jiang, J. X. Lens fiber connexin turnover and caspase-3-mediated cleavage are regulated alternately by phosphorylation. *Cell Commun. Adhes.* **15**, 1–11 (2008).
57. Cantrell, L. S. & Schey, K. L. Proteomic characterization of the human lens and Cataractogenesis. *Expert Rev. Proteomics* **18**, 119–135 (2021).

58. Mathias, R. T., Riquelme, G. & Rae, J. L. Cell to cell communication and pH in the frog lens. *J. Gen. Physiol.* **98**, 1085–1103 (1991).

59. Eckert, R. pH gating of lens fibre connexins. *Pflugers Arch.* **443**, 843–851 (2002).

60. Rong, P. *et al.* Disruption of Gja8 (alpha8 connexin) in mice leads to microphthalmia associated with retardation of lens growth and lens fiber maturation. *Dev. Camb. Engl.* **129**, 167–174 (2002).

61. White, T. W., Goodenough, D. A. & Paul, D. L. Targeted ablation of connexin50 in mice results in microphthalmia and zonular pulverulent cataracts. *J. Cell Biol.* **143**, 815–825 (1998).

62. Baldo, G. J. *et al.* Gap junctional coupling in lenses from alpha(8) connexin knockout mice. *J. Gen. Physiol.* **118**, 447–456 (2001).

63. Gong, X., Baldo, G. J., Kumar, N. M., Gilula, N. B. & Mathias, R. T. Gap junctional coupling in lenses lacking alpha3 connexin. *Proc. Natl. Acad. Sci. U. S. A.* **95**, 15303–15308 (1998).

64. Gao, J., Minogue, P. J., Beyer, E. C., Mathias, R. T. & Berthoud, V. M. Disruption of the lens circulation causes calcium accumulation and precipitates in connexin mutant mice. *Am. J. Physiol. Cell Physiol.* **314**, C492–C503 (2018).

65. Berthoud, V. M. *et al.* The Connexin50D47A Mutant Causes Cataracts by Calcium Precipitation. *Invest. Ophthalmol. Vis. Sci.* **60**, 2336–2346 (2019).

66. Baruch, A. *et al.* Defining a link between gap junction communication, proteolysis, and cataract formation. *J. Biol. Chem.* **276**, 28999–29006 (2001).

67. Tang, Y. *et al.* Age-related cataracts in alpha3Cx46-knockout mice are dependent on a calpain 3 isoform. *Invest. Ophthalmol. Vis. Sci.* **48**, 2685–2694 (2007).

68. Berthoud, V. M. *et al.* Connexin Mutants Compromise the Lens Circulation and Cause Cataracts through Biomineralization. *Int. J. Mol. Sci.* **21**, E5822 (2020).

69. Li, Y., Parkinson, D. Y., Feng, J., Xia, C.-H. & Gong, X. Quantitative X-ray tomographic analysis reveals calcium precipitation in cataractogenesis. *Sci. Rep.* **11**, 17401 (2021).

70. Hughes, J. R. *et al.* No turnover in lens lipids for the entire human lifespan. *eLife* **4**, (2015).

71. Borchman, D. & Yappert, M. C. Lipids and the ocular lens. *J. Lipid Res.* **51**, 2473–2488 (2010).

72. Borchman, D., Stimmelmayr, R. & George, J. C. Whales, lifespan, phospholipids, and cataracts. *J. Lipid Res.* **58**, 2289–2298 (2017).

73. Li, L. K., So, L. & Spector, A. Membrane cholesterol and phospholipid in consecutive concentric sections of human lenses. *J. Lipid Res.* **26**, 600–609 (1985).

74. Li, L. K. & So, L. Age dependent lipid and protein changes in individual bovine lenses. *Curr. Eye Res.* **6**, 599–605 (1987).

75. Li, L. K., So, L. & Spector, A. Age-dependent changes in the distribution and concentration of human lens cholesterol and phospholipids. *Biochim. Biophys. Acta* **917**, 112–120 (1987).

76. Borchman, D., Delamere, N. A., McCauley, L. A. & Paterson, C. A. Studies on the distribution of cholesterol, phospholipid, and protein in the human and bovine lens. *Lens Eye Toxic. Res.* **6**, 703–724 (1989).

77. Subczynski, W. K., Raguz, M., Widomska, J., Mainali, L. & Konovalov, A. Functions of cholesterol and the cholesterol bilayer domain specific to the fiber-cell plasma membrane of the eye lens. *J. Membr. Biol.* **245**, 51–68 (2012).

78. Subczynski, W. K., Pasenkiewicz-Gierula, M., Widomska, J., Mainali, L. & Raguz, M. High Cholesterol/Low Cholesterol: Effects in Biological Membranes: A Review. *Cell Biochem. Biophys.* **75**, 369–385 (2017).

79. Preston Mason, R., Tulenko, T. N. & Jacob, R. F. Direct evidence for cholesterol crystalline domains in biological membranes: role in human pathobiology. *Biochim. Biophys. Acta* **1610**, 198–207 (2003).

80. Mainali, L., Raguz, M., O'Brien, W. J. & Subczynski, W. K. Changes in the Properties and Organization of Human Lens Lipid Membranes Occurring with Age. *Curr. Eye Res.* **42**, 721–731 (2017).

81. Widomska, J., Subczynski, W. K., Mainali, L. & Raguz, M. Cholesterol Bilayer Domains in the Eye Lens Health: A Review. *Cell Biochem. Biophys.* **75**, 387–398 (2017).

82. Borchman, D., Yappert, M. C. & Herrell, P. Structural characterization of human lens membrane lipid by infrared spectroscopy. *Invest. Ophthalmol. Vis. Sci.* **32**, 2404–2416 (1991).

83. Borchman, D., Lamba, O. P. & Yappert, M. C. Structural characterization of lipid membranes from clear and cataractous human lenses. *Exp. Eye Res.* **57**, 199–208 (1993).

84. Borchman, D., Cenedella, R. J. & Lamba, O. P. Role of cholesterol in the structural order of lens membrane lipids. *Exp. Eye Res.* **62**, 191–197 (1996).

85. Trexler, E. B., Bukauskas, F. F., Bennett, M. V., Bargiello, T. A. & Verselis, V. K. Rapid and direct effects of pH on connexins revealed by the connexin46 hemichannel preparation. *J. Gen. Physiol.* **113**, 721–742 (1999).

86. Pfahnl, A. & Dahl, G. Gating of cx46 gap junction hemichannels by calcium and voltage. *Pflugers Arch.* **437**, 345–353 (1999).

87. Peracchia, C. Chemical gating of gap junction channels; roles of calcium, pH and calmodulin. *Biochim. Biophys. Acta* **1662**, 61–80 (2004).

88. Lampe, P. D. & Lau, A. F. The effects of connexin phosphorylation on gap junctional communication. *Int. J. Biochem. Cell Biol.* **36**, 1171–1186 (2004).

89. Cascio, M. Connexins and their environment: effects of lipids composition on ion channels. *Biochim. Biophys. Acta* **1711**, 142–153 (2005).

90. Borchman, D. Lipid conformational order and the etiology of cataract and dry eye. *J. Lipid Res.* **62**, 100039 (2021).

91. Malewicz, B., Kumar, V. V., Johnson, R. G. & Baumann, W. J. Lipids in gap junction assembly and function. *Lipids* **25**, 419–427 (1990).

92. Meyer, R., Malewicz, B., Baumann, W. J. & Johnson, R. G. Increased gap junction assembly between cultured cells upon cholesterol supplementation. *J. Cell Sci.* **96 (Pt 2)**, 231–238 (1990).
93. Zwijsen, R. M., Oudenhoven, I. M. & de Haan, L. H. Effects of cholesterol and oxysterols on gap junctional communication between human smooth muscle cells. *Eur. J. Pharmacol.* **228**, 115–120 (1992).
94. Bastiaanse, E. M., Jongsma, H. J., van der Laarse, A. & Takens-Kwak, B. R. Heptanol-induced decrease in cardiac gap junctional conductance is mediated by a decrease in the fluidity of membranous cholesterol-rich domains. *J. Membr. Biol.* **136**, 135–145 (1993).
95. Biswas, S. K. & Lo, W.-K. Gap junctions contain different amounts of cholesterol which undergo unique sequestering processes during fiber cell differentiation in the embryonic chicken lens. *Mol. Vis.* **13**, 345–359 (2007).
96. Biswas, S. K., Jiang, J. X. & Lo, W.-K. Gap junction remodeling associated with cholesterol redistribution during fiber cell maturation in the adult chicken lens. *Mol. Vis.* **15**, 1492–1508 (2009).
97. Mainali, L., Pasenkiewicz-Gierula, M. & Subczynski, W. K. Formation of cholesterol Bilayer Domains Precedes Formation of Cholesterol Crystals in Membranes Made of the Major Phospholipids of Human Eye Lens Fiber Cell Plasma Membranes. *Curr. Eye Res.* **45**, 162–172 (2020).
98. Locke, D. & Harris, A. L. Connexin channels and phospholipids: association and modulation. *BMC Biol.* **7**, 52 (2009).

99. Hung, A. & Yarovsky, I. Gap junction hemichannel interactions with zwitterionic lipid, anionic lipid, and cholesterol: molecular simulation studies. *Biochemistry* **50**, 1492–1504 (2011).

100. Zhivotovsky, B. & Orrenius, S. Calcium and cell death mechanisms: a perspective from the cell death community. *Cell Calcium* **50**, 211–221 (2011).

101. Lopez, W. *et al.* Mechanism of gating by calcium in connexin hemichannels. *Proc. Natl. Acad. Sci. U. S. A.* **113**, E7986–E7995 (2016).

102. Lopez, W., Gonzalez, J., Liu, Y., Harris, A. L. & Contreras, J. E. Insights on the mechanisms of Ca(2+) regulation of connexin26 hemichannels revealed by human pathogenic mutations (D50N/Y). *J. Gen. Physiol.* **142**, 23–35 (2013).

103. Peracchia, C. Calmodulin-Mediated Regulation of Gap Junction Channels. *Int. J. Mol. Sci.* **21**, E485 (2020).

104. Peracchia, C. Calmodulin-Cork Model of Gap Junction Channel Gating-One Molecule, Two Mechanisms. *Int. J. Mol. Sci.* **21**, E4938 (2020).

105. Bennett, B. C. *et al.* An electrostatic mechanism for Ca(2+)-mediated regulation of gap junction channels. *Nat. Commun.* **7**, 8770 (2016).

106. Lee, H.-J. *et al.* Cryo-EM structure of human Cx31.3/GJC3 connexin hemichannel. *Sci. Adv.* **6**, eaba4996 (2020).

107. Delmar, M. & Makita, N. Cardiac connexins, mutations and arrhythmias. *Curr. Opin. Cardiol.* **27**, 236–241 (2012).

108. Abrams, C. K. & Scherer, S. S. Gap junctions in inherited human disorders of the central nervous system. *Biochim. Biophys. Acta* **1818**, 2030–2047 (2012).

109. Beyer, E. C., Ebihara, L. & Berthoud, V. M. Connexin mutants and cataracts. *Front. Pharmacol.* **4**, 43 (2013).

110. Delmar, M. *et al.* Connexins and Disease. *Cold Spring Harb. Perspect. Biol.* **10**, a029348 (2018).

111. Srinivas, M., Verselis, V. K. & White, T. W. Human diseases associated with connexin mutations. *Biochim. Biophys. Acta Biomembr.* **1860**, 192–201 (2018).

112. Klee, P. *et al.* Connexins protect mouse pancreatic β cells against apoptosis. *J. Clin. Invest.* **121**, 4870–4879 (2011).

113. Ozog, M. A., Siushansian, R. & Naus, C. C. G. Blocked gap junctional coupling increases glutamate-induced neurotoxicity in neuron-astrocyte co-cultures. *J. Neuropathol. Exp. Neurol.* **61**, 132–141 (2002).

114. Saltman, A. E. *et al.* Gap junction uncoupling protects the heart against ischemia. *J. Thorac. Cardiovasc. Surg.* **124**, 371–376 (2002).

115. Rhodes, J. D. & Sanderson, J. The mechanisms of calcium homeostasis and signalling in the lens. *Exp. Eye Res.* **88**, 226–234 (2009).

116. Shiels, A., Bennett, T. M. & Hejtmancik, J. F. Cat-Map: putting cataract on the map. *Mol. Vis.* **16**, 2007–2015 (2010).

117. García, I. E. *et al.* Connexinopathies: a structural and functional glimpse. *BMC Cell Biol.* **17 Suppl 1**, 17 (2016).

118. Dunia, I., Sen Ghosh, C., Benedetti, E. L., Zweers, A. & Bloemendal, H. Isolation and protein pattern of eye lens fiber junctions. *FEBS Lett.* **45**, 139–144 (1974).

119. Benedetti, E. L. *et al.* A portrait of plasma membrane specializations in eye lens epithelium and fibers. *Biochim. Biophys. Acta* **457**, 353–384 (1976).

120. Kistler, J., Kirkland, B. & Bullivant, S. Identification of a 70,000-D protein in lens membrane junctional domains. *J. Cell Biol.* **101**, 28–35 (1985).

121. Kistler, J. & Bullivant, S. Protein processing in lens intercellular junctions: cleavage of MP70 to MP38. *Invest. Ophthalmol. Vis. Sci.* **28**, 1687–1692 (1987).

122. Kistler, J., Christie, D. & Bullivant, S. Homologies between gap junction proteins in lens, heart and liver. *Nature* **331**, 721–723 (1988).

123. Kistler, J. *et al.* Molecular portrait of lens gap junction protein MP70. *J. Struct. Biol.* **103**, 204–211 (1990).

124. Goodenough, D. A. The crystalline lens. A system networked by gap junctional intercellular communication. *Semin. Cell Biol.* **3**, 49–58 (1992).

125. Lampe, P. D. *et al.* In vitro assembly of gap junctions. *J. Struct. Biol.* **107**, 281–290 (1991).

126. Sosinsky, G. E. Image analysis of gap junction structures. *Electron Microsc. Rev.* **5**, 59–76 (1992).

127. Kistler, J., Bond, J., Donaldson, P. & Engel, A. Two distinct levels of gap junction assembly in vitro. *J. Struct. Biol.* **110**, 28–38 (1993).

128. Kistler, J., Goldie, K., Donaldson, P. & Engel, A. Reconstitution of native-type noncrystalline lens fiber gap junctions from isolated hemichannels. *J. Cell Biol.* **126**, 1047–1058 (1994).

129. Raunser, S. & Walz, T. Electron crystallography as a technique to study the structure on membrane proteins in a lipidic environment. *Annu. Rev. Biophys.* **38**, 89–105 (2009).

130. Reichow, S. L. & Gonen, T. Lipid-protein interactions probed by electron crystallography. *Curr. Opin. Struct. Biol.* **19**, 560–565 (2009).

131. Caspar, D. L., Goodenough, D. A., Makowski, L. & Phillips, W. C. Gap junction structures. I. Correlated electron microscopy and x-ray diffraction. *J. Cell Biol.* **74**, 605–628 (1977).

132. Makowski, L., Caspar, D. L., Phillips, W. C. & Goodenough, D. A. Gap junction structures. II. Analysis of the x-ray diffraction data. *J. Cell Biol.* **74**, 629–645 (1977).

133. Unwin, P. N. & Zampighi, G. Structure of the junction between communicating cells. *Nature* **283**, 545–549 (1980).

134. Unwin, P. N. & Ennis, P. D. Two configurations of a channel-forming membrane protein. *Nature* **307**, 609–613 (1984).

135. Unger, V. M., Kumar, N. M., Gilula, N. B. & Yeager, M. Three-dimensional structure of a recombinant gap junction membrane channel. *Science* **283**, 1176–1180 (1999).

136. Fleishman, S. J., Unger, V. M., Yeager, M. & Ben-Tal, N. A Calpha model for the transmembrane alpha helices of gap junction intercellular channels. *Mol. Cell* **15**, 879–888 (2004).

137. Yeager, M. & Nicholson, B. J. Structure of gap junction intercellular channels. *Curr. Opin. Struct. Biol.* **6**, 183–192 (1996).

138. Unger, V. M., Kumar, N. M., Gilula, N. B. & Yeager, M. Projection structure of a gap junction membrane channel at 7 A resolution. *Nat. Struct. Biol.* **4**, 39–43 (1997).

139. Gonen, T., Sliz, P., Kistler, J., Cheng, Y. & Walz, T. Aquaporin-0 membrane junctions reveal the structure of a closed water pore. *Nature* **429**, 193–197 (2004).

140. Gonen, T. *et al.* Lipid-protein interactions in double-layered two-dimensional AQP0 crystals. *Nature* **438**, 633–638 (2005).

141. Oshima, A., Tani, K., Hiroaki, Y., Fujiyoshi, Y. & Sosinsky, G. E. Three-dimensional structure of a human connexin26 gap junction channel reveals a plug in the vestibule. *Proc. Natl. Acad. Sci. U. S. A.* **104**, 10034–10039 (2007).

142. Oshima, A., Tani, K., Hiroaki, Y., Fujiyoshi, Y. & Sosinsky, G. E. Projection structure of a N-terminal deletion mutant of connexin 26 channel with decreased central pore density. *Cell Commun. Adhes.* **15**, 85–93 (2008).

143. Loewenstein, W. R. Junctional intercellular communication: the cell-to-cell membrane channel. *Physiol. Rev.* **61**, 829–913 (1981).

144. Bevans, C. G., Kordel, M., Rhee, S. K. & Harris, A. L. Isoform composition of connexin channels determines selectivity among second messengers and uncharged molecules. *J. Biol. Chem.* **273**, 2808–2816 (1998).

145. Yeager, M. & Harris, A. L. Gap junction channel structure in the early 21st century: facts and fantasies. *Curr. Opin. Cell Biol.* **19**, 521–528 (2007).

146. Gassmann, O. *et al.* The M34A mutant of Connexin26 reveals active conductance states in pore-suspending membranes. *J. Struct. Biol.* **168**, 168–176 (2009).

147. Kwon, T., Harris, A. L., Rossi, A. & Bargiello, T. A. Molecular dynamics simulations of the Cx26 hemichannel: evaluation of structural models with Brownian dynamics. *J. Gen. Physiol.* **138**, 475–493 (2011).

148. Zonta, F., Polles, G., Zanotti, G. & Mammano, F. Permeation pathway of homomeric connexin 26 and connexin 30 channels investigated by molecular dynamics. *J. Biomol. Struct. Dyn.* **29**, 985–998 (2012).

149. Zonta, F., Polles, G., Sanasi, M. F., Bortolozzi, M. & Mammano, F. The 3.5 ångström X-ray structure of the human connexin26 gap junction channel is unlikely that of a fully open channel. *Cell Commun. Signal. CCS* **11**, 15 (2013).

150. Luo, Y., Rossi, A. R. & Harris, A. L. Computational Studies of Molecular Permeation through Connexin26 Channels. *Biophys. J.* **110**, 584–599 (2016).

151. Villanelo, F., Carrasco, J., Jensen-Flores, J., Garate, J. A. & Perez-Acle, T. Simulations on Simple Models of Connexin Hemichannels Indicate That

Ca2+ Blocking Is Not a Pure Electrostatic Effect. *Membranes* **11**, 372 (2021).

152. Pinto, B. I. *et al.* Calcium binding and voltage gating in Cx46 hemichannels. *Sci. Rep.* **7**, 15851 (2017).
153. Zhang, X. *et al.* Near-atomic resolution using electron cryomicroscopy and single-particle reconstruction. *Proc. Natl. Acad. Sci. U. S. A.* **105**, 1867–1872 (2008).
154. Scheres, S. H. W. RELION: implementation of a Bayesian approach to cryo-EM structure determination. *J. Struct. Biol.* **180**, 519–530 (2012).
155. Li, X. *et al.* Electron counting and beam-induced motion correction enable near-atomic-resolution single-particle cryo-EM. *Nat. Methods* **10**, 584–590 (2013).
156. Liao, M., Cao, E., Julius, D. & Cheng, Y. Structure of the TRPV1 ion channel determined by electron cryo-microscopy. *Nature* **504**, 107–112 (2013).
157. Cao, E., Liao, M., Cheng, Y. & Julius, D. TRPV1 structures in distinct conformations reveal activation mechanisms. *Nature* **504**, 113–118 (2013).
158. Scheres, S. H. Beam-induced motion correction for sub-megadalton cryo-EM particles. *eLife* **3**, e03665 (2014).
159. Zoonens, M. & Popot, J.-L. Amphipols for each season. *J. Membr. Biol.* **247**, 759–796 (2014).
160. Pintilie, G. *et al.* Measurement of atom resolvability in cryo-EM maps with Q-scores. *Nat. Methods* **17**, 328–334 (2020).

161. Beckers, M., Mann, D. & Sachse, C. Structural interpretation of cryo-EM image reconstructions. *Prog. Biophys. Mol. Biol.* **160**, 26–36 (2021).

162. Goodenough, D. A. & Paul, D. L. Gap junctions. *Cold Spring Harb. Perspect. Biol.* **1**, a002576 (2009).

163. Harris, A. L. Connexin channel permeability to cytoplasmic molecules. *Prog. Biophys. Mol. Biol.* **94**, 120–143 (2007).

164. Bonacquisti, E. E. & Nguyen, J. Connexin 43 (Cx43) in cancer: Implications for therapeutic approaches via gap junctions. *Cancer Lett.* **442**, 439–444 (2019).

165. Aasen, T., Mesnil, M., Naus, C. C., Lampe, P. D. & Laird, D. W. Gap junctions and cancer: communicating for 50 years. *Nat. Rev. Cancer* **16**, 775–788 (2016).

166. Sosinsky, G. E. & Nicholson, B. J. Structural organization of gap junction channels. *Biochim. Biophys. Acta* **1711**, 99–125 (2005).

167. Meyer, R., Malewicz, B., Baumann, W. J. & Johnson, R. G. Increased gap junction assembly between cultured cells upon cholesterol supplementation. *J. Cell Sci.* **96 (Pt 2)**, 231–238 (1990).

168. Puebla, C., Retamal, M. A., Acuña, R. & Sáez, J. C. Regulation of Connexin-Based Channels by Fatty Acids. *Front. Physiol.* **8**, 11 (2017).

169. Denisov, I. G., Grinkova, Y. V., Lazarides, A. A. & Sligar, S. G. Directed self-assembly of monodisperse phospholipid bilayer Nanodiscs with controlled size. *J. Am. Chem. Soc.* **126**, 3477–3487 (2004).

170. Ritchie, T. K. *et al.* Chapter 11 - Reconstitution of membrane proteins in phospholipid bilayer nanodiscs. *Methods Enzymol.* **464**, 211–231 (2009).
171. Gong, X. Q. & Nicholson, B. J. Size selectivity between gap junction channels composed of different connexins. *Cell Commun. Adhes.* **8**, 187–192 (2001).
172. Trexler, E. B., Bukauskas, F. F., Kronengold, J., Bargiello, T. A. & Verselis, V. K. The first extracellular loop domain is a major determinant of charge selectivity in connexin46 channels. *Biophys. J.* **79**, 3036–3051 (2000).
173. Kronengold, J., Trexler, E. B., Bukauskas, F. F., Bargiello, T. A. & Verselis, V. K. Pore-lining residues identified by single channel SCAM studies in Cx46 hemichannels. *Cell Commun. Adhes.* **10**, 193–199 (2003).
174. Verselis, V. K., Trelles, M. P., Rubinos, C., Bargiello, T. A. & Srinivas, M. Loop gating of connexin hemichannels involves movement of pore-lining residues in the first extracellular loop domain. *J. Biol. Chem.* **284**, 4484–4493 (2009).
175. Oh, S., Verselis, V. K. & Bargiello, T. A. Charges dispersed over the permeation pathway determine the charge selectivity and conductance of a Cx32 chimeric hemichannel. *J. Physiol.* **586**, 2445–2461 (2008).
176. Kwon, T. *et al.* Molecular dynamics simulations of the Cx26 hemichannel: insights into voltage-dependent loop-gating. *Biophys. J.* **102**, 1341–1351 (2012).

177. Bargiello, T. A., Tang, Q., Oh, S. & Kwon, T. Voltage-dependent conformational changes in connexin channels. *Biochim. Biophys. Acta* **1818**, 1807–1822 (2012).

178. Tong, X. *et al.* The First Extracellular Domain Plays an Important Role in Unitary Channel Conductance of Cx50 Gap Junction Channels. *PloS One* **10**, e0143876 (2015).

179. García, I. E. *et al.* The syndromic deafness mutation G12R impairs fast and slow gating in Cx26 hemichannels. *J. Gen. Physiol.* **150**, 697–711 (2018).

180. Rubinos, C., Sánchez, H. A., Verselis, V. K. & Srinivas, M. Mechanism of inhibition of connexin channels by the quinine derivative N-benzylquininium. *J. Gen. Physiol.* **139**, 69–82 (2012).

181. Berthoud, V. M. *et al.* Connexin50D47A decreases levels of fiber cell connexins and impairs lens fiber cell differentiation. *Invest. Ophthalmol. Vis. Sci.* **54**, 7614–7622 (2013).

182. Reis, L. M. *et al.* Whole exome sequencing in dominant cataract identifies a new causative factor, CRYBA2, and a variety of novel alleles in known genes. *Hum. Genet.* **132**, 761–770 (2013).

183. Banks, E. A. *et al.* Connexin mutation that causes dominant congenital cataracts inhibits gap junctions, but not hemichannels, in a dominant negative manner. *J. Cell Sci.* **122**, 378–388 (2009).

184. White, T. W., Bruzzone, R., Wolfram, S., Paul, D. L. & Goodenough, D. A. Selective interactions among the multiple connexin proteins expressed in

the vertebrate lens: the second extracellular domain is a determinant of compatibility between connexins. *J. Cell Biol.* **125**, 879–892 (1994).

185. White, T. W., Paul, D. L., Goodenough, D. A. & Bruzzone, R. Functional analysis of selective interactions among rodent connexins. *Mol. Biol. Cell* **6**, 459–470 (1995).

186. Nakagawa, S. *et al.* Asparagine 175 of connexin32 is a critical residue for docking and forming functional heterotypic gap junction channels with connexin26. *J. Biol. Chem.* **286**, 19672–19681 (2011).

187. Cottrell, G. T. & Burt, J. M. Functional consequences of heterogeneous gap junction channel formation and its influence in health and disease. *Biochim. Biophys. Acta* **1711**, 126–141 (2005).

188. Bai, D. & Wang, A. H. Extracellular domains play different roles in gap junction formation and docking compatibility. *Biochem. J.* **458**, 1–10 (2014).

189. Schadzek, P. *et al.* The cataract related mutation N188T in human connexin46 (hCx46) revealed a critical role for residue N188 in the docking process of gap junction channels. *Biochim. Biophys. Acta* **1858**, 57–66 (2016).

190. Silander, K. *et al.* Spectrum of mutations in Finnish patients with Charcot-Marie-Tooth disease and related neuropathies. *Hum. Mutat.* **12**, 59–68 (1998).

191. Primignani, P. *et al.* A novel dominant missense mutation--D179N--in the GJB2 gene (Connexin 26) associated with non-syndromic hearing loss. *Clin. Genet.* **63**, 516–521 (2003).

192. Deeley, J. M. *et al.* Human lens lipids differ markedly from those of commonly used experimental animals. *Biochim. Biophys. Acta* **1781**, 288–298 (2008).

193. Mabrey, S. & Sturtevant, J. M. Investigation of phase transitions of lipids and lipid mixtures by sensitivity differential scanning calorimetry. *Proc. Natl. Acad. Sci. U. S. A.* **73**, 3862–3866 (1976).

194. Shaw, A. W., McLean, M. A. & Sligar, S. G. Phospholipid phase transitions in homogeneous nanometer scale bilayer discs. *FEBS Lett.* **556**, 260–264 (2004).

195. Vermeer, L. S., de Groot, B. L., Réat, V., Milon, A. & Czaplicki, J. Acyl chain order parameter profiles in phospholipid bilayers: computation from molecular dynamics simulations and comparison with 2H NMR experiments. *Eur. Biophys. J. EBJ* **36**, 919–931 (2007).

196. Khakbaz, P. & Klauda, J. B. Investigation of phase transitions of saturated phosphocholine lipid bilayers via molecular dynamics simulations. *Biochim. Biophys. Acta Biomembr.* **1860**, 1489–1501 (2018).

197. Locke, D., Liu, J. & Harris, A. L. Lipid rafts prepared by different methods contain different connexin channels, but gap junctions are not lipid rafts. *Biochemistry* **44**, 13027–13042 (2005).

198. Schubert, A.-L., Schubert, W., Spray, D. C. & Lisanti, M. P. Connexin family members target to lipid raft domains and interact with caveolin-1. *Biochemistry* **41**, 5754–5764 (2002).

199. Hunte, C. Specific protein-lipid interactions in membrane proteins. *Biochem. Soc. Trans.* **33**, 938–942 (2005).

200. Spray, D. C., Rozental, R. & Srinivas, M. Prospects for rational development of pharmacological gap junction channel blockers. *Curr. Drug Targets* **3**, 455–464 (2002).

201. Reichow, S. L. *et al.* Allosteric mechanism of water-channel gating by Ca2+-calmodulin. *Nat. Struct. Mol. Biol.* **20**, 1085–1092 (2013).

202. Gold, M. G. *et al.* AKAP2 anchors PKA with aquaporin-0 to support ocular lens transparency. *EMBO Mol. Med.* **4**, 15–26 (2012).

203. Reichow, S. L. & Gonen, T. Noncanonical binding of calmodulin to aquaporin-0: implications for channel regulation. *Struct. Lond. Engl. 1993* **16**, 1389–1398 (2008).

204. Efremov, R. G., Gatsogiannis, C. & Raunser, S. Lipid Nanodiscs as a Tool for High-Resolution Structure Determination of Membrane Proteins by Single-Particle Cryo-EM. *Methods Enzymol.* **594**, 1–30 (2017).

205. Tang, G. *et al.* EMAN2: an extensible image processing suite for electron microscopy. *J. Struct. Biol.* **157**, 38–46 (2007).

206. Ludtke, S. J. Single-Particle Refinement and Variability Analysis in EMAN2.1. *Methods Enzymol.* **579**, 159–189 (2016).

207. Zivanov, J. *et al.* New tools for automated high-resolution cryo-EM structure determination in RELION-3. *eLife* **7**, e42166 (2018).

208. Zhang, K. Gctf: Real-time CTF determination and correction. *J. Struct. Biol.* **193**, 1–12 (2016).

209. Zivanov, J., Nakane, T. & Scheres, S. H. W. Estimation of high-order aberrations and anisotropic magnification from cryo-EM data sets in RELION-3.1. *IUCrJ* **7**, 253–267 (2020).

210. Scheres, S. H. W. & Chen, S. Prevention of overfitting in cryo-EM structure determination. *Nat. Methods* **9**, 853–854 (2012).

211. Scheres, S. H. W. Processing of Structurally Heterogeneous Cryo-EM Data in RELION. *Methods Enzymol.* **579**, 125–157 (2016).

212. Pettersen, E. F. *et al.* UCSF ChimeraX: Structure visualization for researchers, educators, and developers. *Protein Sci. Publ. Protein Soc.* **30**, 70–82 (2021).

213. Casañal, A., Lohkamp, B. & Emsley, P. Current developments in Coot for macromolecular model building of Electron Cryo-microscopy and Crystallographic Data. *Protein Sci. Publ. Protein Soc.* **29**, 1069–1078 (2020).

214. Afonine, P. V. *et al.* Real-space refinement in PHENIX for cryo-EM and crystallography. *Acta Crystallogr. Sect. Struct. Biol.* **74**, 531–544 (2018).

215. Williams, C. J. *et al.* MolProbity: More and better reference data for improved all-atom structure validation. *Protein Sci. Publ. Protein Soc.* **27**, 293–315 (2018).

216. Barad, B. A. *et al.* EMRinger: side chain-directed model and map validation for 3D cryo-electron microscopy. *Nat. Methods* **12**, 943–946 (2015).

217. Moriarty, N. W., Grosse-Kunstleve, R. W. & Adams, P. D. electronic Ligand Builder and Optimization Workbench (eLBOW): a tool for ligand coordinate

and restraint generation. *Acta Crystallogr. D Biol. Crystallogr.* **65**, 1074–1080 (2009).

218. Konig, N. & Zampighi, G. A. Purification of bovine lens cell-to-cell channels composed of connexin44 and connexin50. *J. Cell Sci.* **108 (Pt 9)**, 3091–3098 (1995).

219. Humphrey, W., Dalke, A. & Schulten, K. VMD: visual molecular dynamics. *J. Mol. Graph.* **14**, 33–38, 27–28 (1996).

220. Varland, S., Osberg, C. & Arnesen, T. N-terminal modifications of cellular proteins: The enzymes involved, their substrate specificities and biological effects. *Proteomics* **15**, 2385–2401 (2015).

221. Grubmüller, H., Heymann, B. & Tavan, P. Ligand binding: molecular mechanics calculation of the streptavidin-biotin rupture force. *Science* **271**, 997–999 (1996).

222. Wu, E. L. *et al.* CHARMM-GUI Membrane Builder toward realistic biological membrane simulations. *J. Comput. Chem.* **35**, 1997–2004 (2014).

223. Phillips, J. C. *et al.* Scalable molecular dynamics with NAMD. *J. Comput. Chem.* **26**, 1781–1802 (2005).

224. Huang, J. & MacKerell, A. D. CHARMM36 all-atom additive protein force field: validation based on comparison to NMR data. *J. Comput. Chem.* **34**, 2135–2145 (2013).

225. Buchoux, S. FATSLiM: a fast and robust software to analyze MD simulations of membranes. *Bioinforma. Oxf. Engl.* **33**, 133–134 (2017).

226. Piggot, T. J., Allison, J. R., Sessions, R. B. & Essex, J. W. On the Calculation of Acyl Chain Order Parameters from Lipid Simulations. *J. Chem. Theory Comput.* **13**, 5683–5696 (2017).

227. Pettersen, E. F. *et al.* UCSF Chimera--a visualization system for exploratory research and analysis. *J. Comput. Chem.* **25**, 1605–1612 (2004).

228. Community, B. O. *Blender–a 3D modelling and rendering package*. (Stichting Blender Foundation, 2018).

229. Donaldson, P. & Kistler, J. Reconstitution of channels from preparations enriched in lens gap junction protein MP70. *J. Membr. Biol.* **129**, (1992).

230. Smart, O. S., Neduvelil, J. G., Wang, X., Wallace, B. A. & Sansom, M. S. HOLE: a program for the analysis of the pore dimensions of ion channel structural models. *J. Mol. Graph.* **14**, 354–360, 376 (1996).

231. Deeley, J. M. *et al.* Sphingolipid distribution changes with age in the human lens. *J. Lipid Res.* **51**, 2753–2760 (2010).

232. Borchman, D. & Yappert, M. C. Age-related lipid oxidation in human lenses. *Invest. Ophthalmol. Vis. Sci.* **39**, 1053–1058 (1998).

233. Merchant, T. E., Lass, J. H., Meneses, P., Greiner, J. V. & Glonek, T. Human crystalline lens phospholipid analysis with age. *Invest. Ophthalmol. Vis. Sci.* **32**, 549–555 (1991).

234. Zigman, S., Paxhia, T., Marinetti, G. & Girsch, S. Lipids of human lens fiber cell membranes. *Curr. Eye Res.* **3**, 887–896 (1984).

235. Nielsen, M. S. *et al.* Gap junctions. *Compr. Physiol.* **2**, 1981–2035 (2012).

236. Dere, E. & Zlomuzica, A. The role of gap junctions in the brain in health and disease. *Neurosci. Biobehav. Rev.* **36**, 206–217 (2012).

237. Belousov, A. B., Fontes, J. D., Freitas-Andrade, M. & Naus, C. C. Gap junctions and hemichannels: communicating cell death in neurodevelopment and disease. *BMC Cell Biol.* **18**, 4 (2017).

238. van Veen, T. A. B., van Rijen, H. V. M. & Jongsma, H. J. Physiology of cardiovascular gap junctions. *Adv. Cardiol.* **42**, 18–40 (2006).

239. Jansen, J. A., van Veen, T. A. B., de Bakker, J. M. T. & van Rijen, H. V. M. Cardiac connexins and impulse propagation. *J. Mol. Cell. Cardiol.* **48**, 76–82 (2010).

240. Fleschner, C. R. & Cenedella, R. J. Lipid composition of lens plasma membrane fractions enriched in fiber junctions. *J. Lipid Res.* **32**, 45–53 (1991).

241. Gao, J. *et al.* The effects of age on lens transport. *Invest. Ophthalmol. Vis. Sci.* **54**, 7174–7187 (2013).

242. Giannone, A. A., Li, L., Sellitto, C. & White, T. W. Physiological Mechanisms Regulating Lens Transport. *Front. Physiol.* **12**, 818649 (2021).

243. Flores, J. A. *et al.* Connexin-46/50 in a dynamic lipid environment resolved by CryoEM at 1.9 Å. *Nat. Commun.* **11**, 4331 (2020).

244. Yue, B. *et al.* Connexin 46 and connexin 50 gap junction channel properties are shaped by structural and dynamic features of their N-terminal domains. *J. Physiol.* **599**, 3313–3335 (2021).

245. Tong, J.-J. *et al.* Molecular mechanisms underlying enhanced hemichannel function of a cataract-associated Cx50 mutant. *Biophys. J.* **120**, 5644–5656 (2021).

246. Broekhuyse, R. M., Kuhlmann, E. D., Bijvelt, J., Verkleij, A. J. & Ververgaert, P. H. Lens membranes III. Freeze fracture morphology and composition of bovine lens fibre membranes in relation to ageing. *Exp. Eye Res.* **26**, 147–156 (1978).

247. Henderson, D., Eibl, H. & Weber, K. Structure and biochemistry of mouse hepatic gap junctions. *J. Mol. Biol.* **132**, 193–218 (1979).

248. Zampighi, G., Simon, S. A., Robertson, J. D., McIntosh, T. J. & Costello, M. J. On the structural organization of isolated bovine lens fiber junctions. *J. Cell Biol.* **93**, 175–189 (1982).

249. Burendei, B. *et al.* Cryo-EM structures of undocked innexin-6 hemichannels in phospholipids. *Sci. Adv.* **6**, eaax3157 (2020).

250. Sanchez, H. A., Slavi, N., Srinivas, M. & Verselis, V. K. Syndromic deafness mutations at Asn 14 differentially alter the open stability of Cx26 hemichannels. *J. Gen. Physiol.* **148**, 25–42 (2016).

251. Oh, S., Rubin, J. B., Bennett, M. V., Verselis, V. K. & Bargiello, T. A. Molecular determinants of electrical rectification of single channel conductance in gap junctions formed by connexins 26 and 32. *J. Gen. Physiol.* **114**, 339–364 (1999).

252. Tong, J.-J. *et al.* Properties of two cataract-associated mutations located in the NH2 terminus of connexin 46. *Am. J. Physiol. Cell Physiol.* **304**, C823-832 (2013).

253. Nielsen, B. S. *et al.* Structural determinants underlying permeant discrimination of the Cx43 hemichannel. *J. Biol. Chem.* **294**, 16789–16803 (2019).

254. Verselis, V. K., Ginter, C. S. & Bargiello, T. A. Opposite voltage gating polarities of two closely related connexins. *Nature* **368**, 348–351 (1994).

255. Srinivas, M., Kronengold, J., Bukauskas, F. F., Bargiello, T. A. & Verselis, V. K. Correlative studies of gating in Cx46 and Cx50 hemichannels and gap junction channels. *Biophys. J.* **88**, 1725–1739 (2005).

256. Rimkute, L. *et al.* Modulation of Connexin-36 Gap Junction Channels by Intracellular pH and Magnesium Ions. *Front. Physiol.* **9**, 362 (2018).

257. Purnick, P. E., Oh, S., Abrams, C. K., Verselis, V. K. & Bargiello, T. A. Reversal of the gating polarity of gap junctions by negative charge substitutions in the N-terminus of connexin 32. *Biophys. J.* **79**, 2403–2415 (2000).

258. Bargiello, T. A. *et al.* Gating of Connexin Channels by transjunctional-voltage: Conformations and models of open and closed states. *Biochim. Biophys. Acta Biomembr.* **1860**, 22–39 (2018).

259. Manjarrez-Marmolejo, J. & Franco-Pérez, J. Gap Junction Blockers: An Overview of their Effects on Induced Seizures in Animal Models. *Curr. Neuropharmacol.* **14**, 759–771 (2016).

260. Laird, D. W. & Lampe, P. D. Therapeutic strategies targeting connexins. *Nat. Rev. Drug Discov.* **17**, 905–921 (2018).

261. Nalewajska, M., Marchelek-Myśliwiec, M., Opara-Bajerowicz, M., Dziedziejko, V. & Pawlik, A. Connexins-Therapeutic Targets in Cancers. *Int. J. Mol. Sci.* **21**, E9119 (2020).

262. Mastronarde, D. N. Automated electron microscope tomography using robust prediction of specimen movements. *J. Struct. Biol.* **152**, 36–51 (2005).

263. Zheng, S. Q. *et al.* MotionCor2: anisotropic correction of beam-induced motion for improved cryo-electron microscopy. *Nat. Methods* **14**, 331–332 (2017).

264. Punjani, A., Rubinstein, J. L., Fleet, D. J. & Brubaker, M. A. cryoSPARC: algorithms for rapid unsupervised cryo-EM structure determination. *Nat. Methods* **14**, 290–296 (2017).

265. Punjani, A., Zhang, H. & Fleet, D. J. Non-uniform refinement: adaptive regularization improves single-particle cryo-EM reconstruction. *Nat. Methods* **17**, 1214–1221 (2020).

266. Asarnow, D., Palovcak, E. & Cheng, Y. *asarnow/pyem: UCSF pyem v0.5*. (Zenodo, 2019). doi:10.5281/ZENODO.3576630.

267. Spray, D. C., Harris, A. L. & Bennett, M. V. Gap junctional conductance is a simple and sensitive function of intracellular pH. *Science* **211**, 712–715 (1981).

268. Moreno, A. P. Connexin phosphorylation as a regulatory event linked to channel gating. *Biochim. Biophys. Acta* **1711**, 164–171 (2005).

269. Revilla, A., Bennett, M. V. & Barrio, L. C. Molecular determinants of membrane potential dependence in vertebrate gap junction channels. *Proc. Natl. Acad. Sci. U. S. A.* **97**, 14760–14765 (2000).

270. Harris, A. L., Spray, D. C. & Bennett, M. V. Kinetic properties of a voltage-dependent junctional conductance. *J. Gen. Physiol.* **77**, 95–117 (1981).

271. Spray, D. C., Harris, A. L. & Bennett, M. V. Equilibrium properties of a voltage-dependent junctional conductance. *J. Gen. Physiol.* **77**, 77–93 (1981).

272. Palacios-Prado, N. *et al.* Molecular determinants of magnesium-dependent synaptic plasticity at electrical synapses formed by connexin36. *Nat. Commun.* **5**, 4667 (2014).

273. Rose, B. & Loewenstein, W. R. Permeability of cell junction depends on local cytoplasmic calcium activity. *Nature* **254**, 250–252 (1975).

274. Ebihara, L., Liu, X. & Pal, J. D. Effect of external magnesium and calcium on human connexin46 hemichannels. *Biophys. J.* **84**, 277–286 (2003).

275. Zampighi, G. & Unwin, P. N. Two forms of isolated gap junctions. *J. Mol. Biol.* **135**, 451–464 (1979).

276. Müller, D. J., Hand, G. M., Engel, A. & Sosinsky, G. E. Conformational changes in surface structures of isolated connexin 26 gap junctions. *EMBO J.* **21**, 3598–3607 (2002).

277. Oshima, A. *et al.* Asymmetric configurations and N-terminal rearrangements in connexin26 gap junction channels. *J. Mol. Biol.* **405**, 724–735 (2011).

278. Kronengold, J., Srinivas, M. & Verselis, V. K. The N-terminal half of the connexin protein contains the core elements of the pore and voltage gates. *J. Membr. Biol.* **245**, 453–463 (2012).

279. Ek-Vitorin, J. F. & Burt, J. M. Structural basis for the selective permeability of channels made of communicating junction proteins. *Biochim. Biophys. Acta* **1828**, 51–68 (2013).

280. Yue, B. *et al.* Connexin 46 and connexin 50 gap junction channel properties are shaped by structural and dynamic features of their N-terminal domains. *J. Physiol.* **599**, 3313–3335 (2021).

281. Henderson, R. *et al.* Outcome of the first electron microscopy validation task force meeting. *Struct. Lond. Engl. 1993* **20**, 205–214 (2012).

282. Peracchia, C. & Peracchia, L. L. Inversion of both gating polarity and CO2 sensitivity of voltage gating with D3N mutation of Cx50. *Am. J. Physiol. Cell Physiol.* **288**, C1381-1389 (2005).

283. Xin, L. & Bai, D. Functional roles of the amino terminal domain in determining biophysical properties of Cx50 gap junction channels. *Front. Physiol.* **4**, 373 (2013).

284. Xu, Q., Lin, X., Matiukas, A., Zhang, X. & Veenstra, R. D. Specificity of the connexin W3/4 locus for functional gap junction formation. *Channels Austin Tex* **10**, 453–465 (2016).

285. Infield, D. T. *et al.* Cation-π Interactions and their Functional Roles in Membrane Proteins. *J. Mol. Biol.* **433**, 167035 (2021).

286. Trexler, E. B., Bennett, M. V., Bargiello, T. A. & Verselis, V. K. Voltage gating and permeation in a gap junction hemichannel. *Proc. Natl. Acad. Sci. U. S. A.* **93**, 5836–5841 (1996).

287. Srinivas, M. *et al.* Voltage dependence of macroscopic and unitary currents of gap junction channels formed by mouse connexin50 expressed in rat neuroblastoma cells. *J. Physiol.* **517 (Pt 3)**, 673–689 (1999).

288. Tong, J.-J., Liu, X., Dong, L. & Ebihara, L. Exchange of gating properties between rat cx46 and chicken cx45.6. *Biophys. J.* **87**, 2397–2406 (2004).

289. Sakai, R., Elfgang, C., Vogel, R., Willecke, K. & Weingart, R. The electrical behaviour of rat connexin46 gap junction channels expressed in transfected HeLa cells. *Pflugers Arch.* **446**, 714–727 (2003).

290. Tong, J.-J. & Ebihara, L. Structural determinants for the differences in voltage gating of chicken Cx56 and Cx45.6 gap-junctional hemichannels. *Biophys. J.* **91**, 2142–2154 (2006).

291. Gao, J. *et al.* Lens intracellular hydrostatic pressure is generated by the circulation of sodium and modulated by gap junction coupling. *J. Gen. Physiol.* **137**, 507–520 (2011).

292. Punjani, A. & Fleet, D. J. 3D variability analysis: Resolving continuous flexibility and discrete heterogeneity from single particle cryo-EM. *J. Struct. Biol.* **213**, 107702 (2021).

293. Khan, A. K. *et al.* A Steric 'Ball-and-Chain' Mechanism for pH-Mediated Regulation of Gap Junction Channels. *Cell Rep.* **31**, 107482 (2020).

294. Vrionis, F. D. *et al.* The bystander effect exerted by tumor cells expressing the herpes simplex virus thymidine kinase (HSVtk) gene is dependent on connexin expression and cell communication via gap junctions. *Gene Ther.* **4**, 577–585 (1997).

295. Fick, J. *et al.* The extent of heterocellular communication mediated by gap junctions is predictive of bystander tumor cytotoxicity in vitro. *Proc. Natl. Acad. Sci. U. S. A.* **92**, 11071–11075 (1995).

296. Kisch, B. Electron microscopy as applied to cardiology. *J. Mt. Sinai Hosp. N. Y.* **19**, 606–611 (1952).

297. Sjostrand, F. S. & Andersson, E. Electron microscopy of the intercalated discs of cardiac muscle tissue. *Experientia* **10**, 369–370 (1954).

298. Kisch, B. Studies in comparative electron microscopy of the heart. II. Guinea pig and rat. *Exp. Med. Surg.* **13**, 404–428 (1955).

299. Sjostrand, F. S., Andersson-Cedergren, E. & Dewey, M. M. The ultrastructure of the intercalated discs of frog, mouse and guinea pig cardiac muscle. *J. Ultrastruct. Res.* **1**, 271–287 (1958).

300. Sikerwar, S. S. & Unwin, N. Three-dimensional structure of gap junctions in fragmented plasma membranes from rat liver. *Biophys. J.* **54**, 113–119 (1988).

301. Zampighi, G., Kreman, M., Ramón, F., Moreno, A. L. & Simon, S. A. Structural characteristics of gap junctions. I. Channel number in coupled and uncoupled conditions. *J. Cell Biol.* **106**, 1667–1678 (1988).
302. Milazzo, A.-C. *et al.* Initial evaluation of a direct detection device detector for single particle cryo-electron microscopy. *J. Struct. Biol.* **176**, 404–408 (2011).
303. Bammes, B. E., Rochat, R. H., Jakana, J., Chen, D.-H. & Chiu, W. Direct electron detection yields cryo-EM reconstructions at resolutions beyond 3/4 Nyquist frequency. *J. Struct. Biol.* **177**, 589–601 (2012).
304. Campbell, M. G. *et al.* Movies of ice-embedded particles enhance resolution in electron cryo-microscopy. *Struct. Lond. Engl. 1993* **20**, 1823–1828 (2012).
305. Shigematsu, H. & Sigworth, F. J. Noise models and cryo-EM drift correction with a direct-electron camera. *Ultramicroscopy* **131**, 61–69 (2013).
306. Cheng, A., Tan, Y. Z., Dandey, V. P., Potter, C. S. & Carragher, B. Strategies for Automated CryoEM Data Collection Using Direct Detectors. *Methods Enzymol.* **579**, 87–102 (2016).
307. Wu, S., Armache, J.-P. & Cheng, Y. Single-particle cryo-EM data acquisition by using direct electron detection camera. *Microsc. Oxf. Engl.* **65**, 35–41 (2016).
308. Tan, Y. Z., Cheng, A., Potter, C. S. & Carragher, B. Automated data collection in single particle electron microscopy. *Microsc. Oxf. Engl.* **65**, 43–56 (2016).

309. Baldwin, P. R. *et al.* Big data in cryoEM: automated collection, processing and accessibility of EM data. *Curr. Opin. Microbiol.* **43**, 1–8 (2018).

310. Sigworth, F. J., Doerschuk, P. C., Carazo, J.-M. & Scheres, S. H. W. An introduction to maximum-likelihood methods in cryo-EM. *Methods Enzymol.* **482**, 263–294 (2010).

311. Scheres, S. H. W. A Bayesian view on cryo-EM structure determination. *J. Mol. Biol.* **415**, 406–418 (2012).

312. Lyumkis, D., Brilot, A. F., Theobald, D. L. & Grigorieff, N. Likelihood-based classification of cryo-EM images using FREALIGN. *J. Struct. Biol.* **183**, 377–388 (2013).

313. Chen, S. *et al.* High-resolution noise substitution to measure overfitting and validate resolution in 3D structure determination by single particle electron cryomicroscopy. *Ultramicroscopy* **135**, 24–35 (2013).

314. Kühlbrandt, W. Biochemistry. The resolution revolution. *Science* **343**, 1443–1444 (2014).

315. Oshima, A. Potential of cryo-EM for high-resolution structural analysis of gap junction channels. *Curr. Opin. Struct. Biol.* **54**, 78–85 (2019).

316. Oshima, A. Structural insights into gap junction channels boosted by cryo-EM. *Curr. Opin. Struct. Biol.* **63**, 42–48 (2020).

317. Syrjanen, J., Michalski, K., Kawate, T. & Furukawa, H. On the molecular nature of large-pore channels. *J. Mol. Biol.* **433**, 166994 (2021).

318. Renaud, J.-P. *et al.* Cryo-EM in drug discovery: achievements, limitations and prospects. *Nat. Rev. Drug Discov.* **17**, 471–492 (2018).

319. Wigge, C., Stefanovic, A. & Radjainia, M. The rapidly evolving role of cryo-EM in drug design. *Drug Discov. Today Technol.* **38**, 91–102 (2020).

320. Berman, H. M. *et al.* The Protein Data Bank. *Nucleic Acids Res.* **28**, 235–242 (2000).

321. Tegunov, D., Xue, L., Dienemann, C., Cramer, P. & Mahamid, J. Multi-particle cryo-EM refinement with M visualizes ribosome-antibiotic complex at 3.5 Å in cells. *Nat. Methods* **18**, 186–193 (2021).

322. Ni, T. *et al.* High-resolution in situ structure determination by cryo-electron tomography and subtomogram averaging using emClarity. *Nat. Protoc.* **17**, 421–444 (2022).

323. Bäuerlein, F. J. B. & Baumeister, W. Towards Visual Proteomics at High Resolution. *J. Mol. Biol.* **433**, 167187 (2021).